

STRUCTURAL AND ELECTRONIC PROPERTIES OF HYDROGENATED
NANOCRYSTALLINE SILICON EMPLOYED IN THIN FILM PHOTOVOLTAICS

by

PETER GEORGE HUGGER

A DISSERTATION

Presented to the Department of Physics
and the Graduate School of the University of Oregon
in partial fulfillment of the requirements
for the degree of
Doctor of Philosophy

March 2011

DISSERTATION APPROVAL PAGE

Student: Peter George Hugger

Title: Structural and Electronic Properties of Hydrogenated Nanocrystalline Silicon
Employed in Thin Film Photovoltaics

This dissertation has been accepted and approved in partial fulfillment of the requirements for the Doctor of Philosophy degree in the Department of Physics by:

Dr. Miriam Deutsch	Chairperson
Dr. J. David Cohen	Advisor
Dr. Roger Haydock	Member
Dr. Heiner Linke	Member
Dr. Mark Lonergan	Outside Member

and

Richard Linton	Vice President for Research and Graduate Studies/Dean of the Graduate School
----------------	---

Original approval signatures are on file with the University of Oregon Graduate School.

Degree awarded March 2011

© 2011 Peter George Hugger

DISSERTATION ABSTRACT

Peter George Hugger

Doctor of Philosophy

Department of Physics

March 2011

Title: Structural and Electronic Properties of Hydrogenated Nanocrystalline Silicon
Employed in Thin Film Photovoltaics

Approved: _____
Dr. J. David Cohen

Hydrogenated nanocrystalline silicon (nc-Si:H) is a semiconducting material that is very useful as a thin film photovoltaic. A mixture of amorphous and crystalline silicon components, nc-Si:H shows good carrier mobilities, enhanced infrared response, and high resilience to light-induced degradation of its electronic properties, a thermally reversible degenerative phenomenon known as the Staebler-Wronski Effect (SWE). However, production of nc-Si:H is difficult in part because the structural and electronic properties of this material are not well understood. For example, its electronic properties have even been observed by some authors to improve upon prolonged light exposure, in direct opposition to the SWE observed in purely amorphous thin film silicon.

We used several junction capacitance based measurements together with characterization methods such as Raman spectroscopy and secondary ion mass spectroscopy to better understand the structure/function relationships present in nc-Si:H. Drive level capacitance profiling (DLCP) was used to determine densities, spatial

distributions, and energies of deep-gap defects. Transient photocapacitance (TPC) and transient photocurrent (TPI) were used to characterize optical transitions and the degree of minority carrier collection. Materials had crystallite volume fractions between 20% and 80% and were deposited using RF and modified VHF glow discharge (PECVD) processes at United Solar Ovonix, LLC. Measurements were made as a function of metastable state: annealed states were produced by exposing the material to temperatures above 370K for 0.5h and the lightsoaked state was produced by exposure to 200mW/cm² 610nm long-pass filtered light from an ELH halogen source for 100h.

We identified two deep defects in nc-Si:H. A primary defect appearing throughout the material at an electronic transition energy of roughly 0.7eV below the conduction band, and a second defect 0.4eV below the conduction band which was localized near the p/i junction interface. Results suggested that the deeper defect is related to the presence of oxygen and is located in grain boundary regions. The energy depth of this defect appears also to be somewhat dependent on metastable state. This phenomenon, and the universal decrease in minority carrier collection upon lightsoaking are accounted for in a model of electronic behavior we have developed over the course of this study.

CURRICULUM VITAE

NAME OF AUTHOR: Peter G. Hugger

GRADUATE AND UNDERGRADUATE SCHOOLS ATTENDED:

University of Oregon, Eugene OR
Virginia Military Institute, Lexington VA

DEGREES AWARDED:

Doctor of Philosophy, Physics, 2011, University of Oregon
Bachelor of Science, Physics, 2003, Virginia Military Institute

AREAS OF SPECIAL INTEREST:

Mixed phase and polymorph semiconductors

Silicon and silicon alloy semiconductors

Thin film photovoltaics

PROFESSIONAL EXPERIENCE:

Research and Teaching Assistant, Department of Physics, University of Oregon
Eugene, OR, 2003-2011

Summer Researcher, Space Telescope Science Institute, Baltimore, MD, 2002

GRANTS, AWARDS, AND HONORS:

National Science Foundation IGERT Fellow, University of Oregon, 2009-2010

PUBLICATIONS:

P.G. Hugger, J. Lee, G. Yue, X. Xu, B. Yan, J. Yang and S. Guha. "Material properties of a-SiGe:H solar cells as a function of growth rate." *Mater. Res. Soc. Symp. Proc.* **1245**, A07-03 (2010)

X. Xu, D. Beglau, S. Ehlert, Y. Li, T. Su, G. Yue, B. Yan, K. Lord, A. Banerjee, J. Yang, S. Guha, P. Hugger, and J. David Cohen. "High Efficiency Large Area a-Si:H and a-SiGe:H Multi-junction Solar Cells Using MVHF at High Deposition Rate" *Phys. Stat. Sol.* **7**, pp.1077-1080 (2010)

P.G. Hugger, J.D. Cohen, B. Yan, G. Yue, J. Yang and S. Guha. "Relationship of deep defects to oxygen and hydrogen content in nanocrystalline silicon photovoltaic materials." *Appl. Phys. Lett.* **97**, 252103 (2010).

P.G Hugger, J David Cohen, B. Yan, J. Yang and S. Guha "Insights and challenges toward understanding the electronic properties of hydrogenated nanocrystalline silicon." *Philo. Mag.* **89**, pp 2541-2555 (2009)

P.G. Hugger, J. Lee, J. David Cohen, G. Yue, X. Xu, B. Yan, J. Yang and S. Guha. "Junction Capacitance Study of a-SiGe:H Solar Cells Grown at Varying RF and VHF Deposition Rates." *Mater. Res. Soc. Symp. Proc.* **1153**, A07-12 (2009)

P.G. Hugger, J. D. Cohen, B. Yan, J. Yang and S. Guha. "Properties of light-induced degradation and the electronic properties of nanocrystalline silicon solar cells grown under functionally graded hydrogen dilutions." *J. of Non-Cryst. Sol.* **354**, 19-25 (2008)

P.G. Hugger, J.D. Cohen, B. Yan, G. Yue, X. Xu, J. Yang and S. Guha. "Electronic Properties of Nanocrystalline Silicon Deposited With Different Crystallite Fractions And Growth Rates." *Mater. Res. Soc. Symp. Proc.* **1066**, A06-06 (2008)

P.G. Hugger, S. Datta, P.T Erslev, G. Yue, G. Ganguly, B. Yan, J. Yang, S. Guha and J.D. Cohen. "Electronic Characterization and Light-Induced Degradation in nc-Si:H Solar Cells" *Mater. Res. Soc. Symp. Proc.* **910**, A02-01 (2006)

ACKNOWLEDGMENTS

I would like to acknowledge and express my deepest gratitude first to my parents and grandparents, for their unwavering love and support throughout my entire life. Surely if it were not for their kind upbringing I would never have had the opportunity to begin this study. I would also like to express my appreciation for my good friends Jason Miller, Ian Pilgrim and Westley Miller, who have helped me through many of life's ups and downs and have kept me happy and part of the community throughout my graduate work. Surely the importance of good friends can never be understated or ignored. Thank you all!

I am also thankful for my many colleagues within the materials science field. First of all, our wonderful collaborators at United Solar Ovonic, LLC: Subhendu Guha, Jeffrey Yang, Baojie Yan, Guozhen Yue, Xixiang Xu and others. Without your hard work and expertise with producing silicon-based photovoltaics of amazing quality, this work would never have made any progress. Thank you so much. Thank you, indeed, to the entire SAI research team and all its members from NREL, the Colorado School of Mines, Syracuse University and elsewhere. I also thank and acknowledge my office mate for years, Dr. Pete Erslev, who engaged me in many useful and interesting discussions that increased my knowledge of Physics and materials science, for his good friendship and for the excellent example he set as a good worker and experimentalist.

I am also thankful for the wonderful professionals here at the University of Oregon who helped me with my day-to-day problems, both great and small. Finishing my degree may have been impossible without the kind friendship and aid of Jeanne Basom, Jani Levy, Patty Smith, Patty Valenzuela, and Doreen Kester. I must give a very special and heartfelt

‘thank you’ to Bonnie Grimm, who acted as friend, confidante, and advisor to me my entire tenure here at the University of Oregon. Thank you, Bonnie!

Lastly, I must thank my advisor, David Cohen. His knowledge and experience, his patience and agreeableness, and his wise and balanced attitude toward living have helped me a great deal not only toward the completion of this dissertation, but in my journey through life as well. Thank you, Dave.

This dissertation I dedicate to all these individuals. I appreciate you all! This work is as much all of yours as it is mine.

Dedicated to my parents, Paul and Vickie Hugger

TABLE OF CONTENTS

Chapter	Page
I. INTRODUCTION	1
1.1. A Brief Perspective	1
1.2. The Ideal Crystal	3
1.3. Amorphous and Non-Ideal Crystals.....	6
Chemical Bonding, Coordination Defects, and the “8-N” Rule	7
Density of States	8
1.4. General Properties of Mixed Phase Materials	10
Definition of “Mixed Phase”	10
Types of Two-Phase Systems	11
Formation of the Grain Boundary Potential.....	14
Carrier Percolation	17
1.5. Summary and Purpose of This Work.....	18
II. EXPERIMENTAL TECHNIQUES	21
2.1. Formation of the <i>pn</i> Junction	21
2.2. General Formalism of the Depletion Capacitance	23
2.3. Depletion Capacitance and Gap State Profiling in Crystalline Semiconductors.....	25
2.4. Depletion Capacitance and Gap State Profiling in Disordered Semiconductors.....	27

Chapter	Page
2.5. Drive Level Capacitance Profiling.....	32
2.6. Optical Measurements	33
Transient Photocapacitance and Transient Photocurrent	35
Raman Spectroscopy	42
III. STRUCTURAL AND COMPOSITIONAL PROPERTIES OF NC-SI:H.....	47
3.1. Film Growth and Structure	47
3.2. Nanostructure.....	51
3.3. Compositional Variations	56
The Presence of Oxygen	61
IV. DEEP STATE DISTRIBUTIONS IN NC-SI:H.....	67
4.1. Crystallinity and Deep Defect Densities.....	67
4.2. Correlations with Oxygen and Hydrogen Content.....	71
4.3. Modeling Deep Defect Densities	74
Modeling the Temperature Dependence	80
Modeling the Metastable State Change.....	82
4.4. Host Phase of Deep Defects.....	85
4.5. Presence of the Near Interface Defect of Transition Energy 0.4eV	87

Chapter	Page
V. OPTICAL DETERMINATION OF ELECTRONIC PROPERTIES	92
5.1. Optically Measured Deep State Distributions.....	92
5.2. Light Trapping Effects.....	101
VI. INTERPRETATION AND DISCUSSION	106
6.1. Interpretation of the Optical Spectra.....	106
6.2. Interpretation of Drive Level Capacitance Profiling (DLCP) Results.....	108
VII. SUMMARY AND CONCLUSIONS.....	115
7.1. Ideas for Future Experiments.....	117
APPENDICES	119
A. DETAILS ON THE MODELING OF DLCP DATA.....	119
B. DEVICE PREPARATION AND APPLICATIONS	125
REFERENCES CITED.....	129

LIST OF FIGURES

Figure	Page
1.1. For crystalline solids, the Fermi level position in relation to boundary energies of the bands $E_n(\mathbf{k})$ determine whether the solid is conducting, insulating, or semiconducting.	4
1.2. When a material exhibits short and long-range atomic order (left), the theory of Bloch electrons provides the theoretical basis for the formation of the valence band, the band gap, and the conduction band.	5
1.3. (left) A schematic continuous random network (CRN) of atoms which desire 3-fold coordination. Interstitial and substitution related defects can be found in all kinds of non-ideal networks, but over- and under-coordinated atoms are a feature only of a CRN. (right) A schematic sub-bandgap density of states for an amorphous semiconductor. Structural and thermal disorder produces broader band tails than in the crystalline case and localized defects introduce electronic states into the material's bandgap.	6
1.4. The “cubic grain model” is a good way of modeling conduction in a well-mixed two-phase material in which the inclusionary cubic grains (“phase b” above) do not amalgamate.	13
1.5. Potential barriers can be produced in grain boundary (GB) regions by the presence of charged defects. If a large number of defects are present at a GB, then the Fermi level can become pinned to the defect distribution, thus inducing a potential barrier in to the conduction and valence bands (a), if the number of GB defects is small, the potential barrier is lower (b).	16
2.1. The depletion capacitance is formed when two materials of different bulk Fermi level energies (a) are brought into conductive contact. Charged regions form on each side of the junction until, at thermal equilibrium conditions, drive currents exactly cancel the diffusion currents (b).	21
2.2. A band diagram representation of the dynamic response of a junction to a voltage pulse. (a) the original reverse-biased condition; (b) the forward biased condition; and (c) an optically assisted return of the junction to the original reverse-biased condition.	36
2.3. Sample output Raman data from the Renishaw RM series confocal microscope. The excitation laser during this measurement was 785nm.	44

Figure	Page
3.1. The total crystalline volume fraction and crystallize size distribution for RF PECVD deposited silicon films as a function of RF power density and hydrogen dilution. The “A’s” refer to pure a-Si:H growth. (adapted from [41])	48
3.2. This TEM cross section image of highly crystalline (~70vol%) nc-Si:H shows columnar and cone-like nanocrystalline structures near the material surface. The growth direction was from the bottom of the image to the top. Similar dome-like surface protrusions were studied in [42] to quantify the relative growth rates of a-Si:H and the nanocrystallites. Differences in contrast denote the presence of differently oriented crystallite structures.	49
3.3. The cone-angle experiment presented in [42], which yielded a mean cone half angle of $\Theta=40^\circ$, was repeated on one highly crystalline sample (sample 16115) included in this study, yielding $\Theta=32.9^\circ$. Cone angles were found by extrapolating cone angles from best fits to spherical protrusions from the material surface.	50
3.4. A schematic adapted from [51] showing an idealized progression from polycrystalline silicon (a) to nearly pure amorphous silicon (c). The best nc-Si:H devices are always prepared in the “well-mixed” growth region near (b), where both phases exist in nearly equal volumes. These structural changes are most readily accomplished by varying the hydrogen-to-silane concentration ratio.	51
3.5. A schematic view of a typical sample array. Blue dots represent individual contacts. Contacts located centrally (C) are more crystalline than those located radially (R). Beyond a certain distance (indicated by the large circle) from the substrate center, samples were nearly fully amorphous.....	52
3.6. Sample Raman spectra with deconvolved component peaks from samples whose crystallinity was allowed to vary across the substrate (see Figure 3.4). Samples located centrally were more crystalline than those located radially. By using a strongly absorbed excitation wavelength (488nm) it was also seen that some samples showed an amorphous character near the p/i interface.	53
3.7. Typical SIMS spectrum of a nc-Si:H intrinsic layer. The increased counts near sputter time of 3500s indicates the presence of the substrate. A sputter time of 0s indicates the ‘top’ or light-incident side of the sample.	56
3.8. Hydrogen profiling effects are clearly seen using SIMS profiling. (top) a film grown using constant H dilution (bottom) a film grown as the H dilution was ramped down throughout the deposition.....	58

Figure	Page
3.9. Hydrogen dilution profiling effects on the open circuit voltage (V_{OC}). As expected, the average crystallinity yielded by Raman spectroscopy correlated well with V_{OC} , but those films with more amorphous content near the junction contact showed very high open circuit voltages.	59
3.10. Many nc-Si:H measured in this study showed significant concentrations of oxygen. A rough correlation of oxygen content to crystallinity was observed.	61
3.11. Zero loss EELS (left) and oxygen map EELS (right). Slightly higher concentrations of oxygen (right) seem to occur at the same location of the grain boundary type structures (left).	62
3.12. This high-resolution TEM image clearly indicates the presence of crystallites and grain boundaries in nc-Si:H. This particular sample, 14036, had a crystallite volume fraction of $X_c=0.61$. Growth direction in this image was from right to left. The region of disordered material on the left hand side of the image is most likely an effect of the ion-milling beam used for sample preparation. Note that in addition to clear regions of crystallite intersection, also visible are column-like crystal structures and overlaid crystal structures. The latter is an indicator that the sample thickness ($\sim 100\text{nm}$) was larger than the crystallite sizes ($\sim 20\text{nm}$).....	64
3.13. Oxygen per Hydrogen concentrations plotted against deconvolved Raman peak intensities. The linear increase ($R^2=0.3$) of $[O]/[H]$ with the 515cm^{-1} could suggest that oxygen accumulates in grain boundary regions.....	65
4.1. State A (open symbols) and State B (closed symbols) deep defect response, indicated by the temperature dependence of drive-level profiles, was seen to correlate with material crystallinity, indicated by the Raman spectra insets. Surprisingly, for the most amorphous samples it was often seen that DLCP densities would <i>decrease</i> upon lightsoaking.....	68
4.2. Some samples showed a metastable <i>decrease</i> in DLCP densities after lightsoaking, as shown here. This behavior, which seems at odds with the tenets of the Staebler-Wronski Effect, is discussed further in Chapter 6.....	69
4.3. An example of State B admittance data for the most crystalline material shown in Figure 4.1. The activation “step” in capacitance does not correspond to the temperature-dependent behavior of the DLCP density, indicating that some other process is causing this effect.	70

Figure	Page
4.4. Oxygen content, measured by [O]/[H] and [O]/[³⁰ Si] SIMS count ratios (above left), and DLCP densities (lower left) both correlated with device crystallinity. In particular, a very good correlation was seen between the [O]/[H] concentration and deep defect density (right). This could suggest that deep defects are the result of an H-mitigated oxygen-based center.	72
4.5. Spatial correlations between oxygen concentrations and E _C -0.7eV deep defect densities were also observed within individual films. The deep defect distributions were derived via modeling of DLCP data. The energy depth of such defects appear to become shallower upon lightsoaking.	74
4.6. A few samples prepared with thicker intrinsic layers showed curious State A (left) and State B (right) drive level profiles. The exact shapes of these profiles could be reproduced via modeling efforts.	75
4.7. The quantitative agreement between temperature (left) and frequency (right) domain data underscore the thermally-activated nature of these drive level profiles. Also shown are modeled fits to the data (dashed lines).....	77
4.8 A schematic describing the only density of states configuration found to adequately describe the State A drive level profiles of thick nc-Si:H samples. The dip was found to occur as the Fermi level crossed a relatively shallow (~ 0.4eV) defect located near the p-n junction (right) while at large values of reverse bias it did not (left)..	79
4.9. Spatial distributions of the sum of <i>all</i> deep states and shallow states (free carriers) were constrained to obey a sum rule across temperature changes for each metastable state that was modeled. The temperature dependence of the drive-level profiles was reproduced by changing the spatial extent of the region in which free carrier density was low.	80
4.10. A schematic representation of a randomized potential landscape, as described in Section 1.4. Grey areas represent regions where carrier conduction (percolation) is not possible. Our modeling results are consistent with a spatially dependent freezeout of conduction through conduction band states as the temperature is lowered, as shown in the progression in the figure.....	81
4.11. DLCP densities (left) were seen to first decrease, then later increase as a function of lightsoaking. These data were modeled (solid curves, right) by considering monotonic decreases in free carrier density and a monotonic density increase and simultaneous energy shift of deep defects from E _C -0.7eV to E _C -0.55eV.	83

Figure	Page
4.12. Bandgap schematics showing grain boundary material surrounded by crystallite material illustrate the process producing the lightsoak sequence from Figure 4.11. State A (left) carrier densities reduce and charged deep defect densities increase at early stages of lightsoaking (center). At later stages of lightsoaking free carrier densities are low and shallower, neutral defects are created.	84
4.13. For thick samples exhibiting the degradation response shown in Figure 4.11, light-induced degradation does not occur at incident photon energies of 1.5eV, but does occur for 2eV light. This strongly suggests that recombination events in the amorphous/grain boundary phase are the cause of metastability.....	86
4.14. Spatial distributions of shallow states (free carriers) and both deep defect states. The solid light blue line indicates the spatial distribution of the 0.4eV deep defects, and the orange triangles indicate the spatial distribution of the 0.7eV defects.	87
4.15. The original DLCP data from which the deep and shallow state distributions in Figure 4.13 (right) were derived (sample 15123-74; $X_c=0.69$). A specific near-interface distribution of deep states with transition energy 0.4eV was required to reproduce these DLCP results, despite the fact that no obvious “dip” betrayed the presence of this defect state. In retrospect, the broad spatial dependence of the DLCP signal out to 0.8mm from the junction interface indicates the presence of the 0.4eV state in this data.	88
4.16. These State B data both indicate the presence of a shallow, near-interface defect. (left) the lowest temperature profile indicates the spatial dependence of the 0.4eV defect while the 350K profile indicates the spatial dependence of the 0.7eV state. (right) This State B data is reminiscent of the annealed state data for sample 16115, but exhibits a much more subtle “dip” which we once again attribute to the 0.4eV near interface state. For this sample $X_c=0.59$	89
4.17. For a limited set of samples the presence of boron, in the form of the diatomic molecule BO, was investigated using secondary ion mass spectrometry. Densities of boron were very low in these samples, as seen in the figure, but spatial variation in the near-interface region is present in these samples. No correlation with the presence of 0.4eV defects has yet been determined.	90
5.1. A typical nc-Si:H TPC/TPI dataset with best fit curve for a sample that exhibited significant deep state response in DLCP measurements performed in the degraded state. The presence of a significant defect band near 0.75eV seems correlated with the defect response in DLCP. The pseudo-regular fluctuations in this data is the result of thin film interference.	93

- 5.2. Data in the annealed state for two nc-Si:H samples of different crystalline volume fractions. For both samples, the degree of minority carrier collection decreases with temperature. (left) The overall change in this collection fraction is quite large for the more crystalline material (sample 14036). (right) the more amorphous material (sample 14657) shows a lower magnitude change, but at higher measurement temperatures a decidedly amorphous-like residual TPC spectrum is revealed, showing a bandgap energy of $\sim 1.7\text{eV}$. [78] 94
- 5.3. Photocapacitance (TPC) and photocurrent (TPI) data are shown in both the annealed and lightsoaked states for samples of very different crystalline volume fraction. (left) the highly crystalline film (sample 16115) shows no evidence of an a-Si:H – like bandgap. In its lightsoaked state, the negative TPC signal below optical energies of 0.9eV indicates optical transitions into deep defect states above the Fermi level. Data were taken at 325K . (right) A more amorphous film (sample 13993) shows an a-Si:H – like band edge near 1.7eV . A negative feature appears near 1.2eV in the annealed state. Data were taken at 295K 97
- 5.4. Among the earliest results of this study was a correlation between minority carrier collection and cell performance in the annealed state. 98
- 5.5. The effects of light trapping were investigated in sample 14036 by using transient photocurrent (TPI) measurements. The effect of adding a textured back reflector was to broaden the effective TPI absorption curve. 102
- 5.6. The TPI method is well suited to imaging optical absorption over IR wavelengths. These data compare a TPI spectrum with a corresponding transmission/reflection spectrum, which becomes obscured at optical energies below $\sim 1.2\text{eV}$. [87] 104
- 6.1. We believe tunneling effects involving grain boundaries explain the optical transition energies for more crystalline (left) and more amorphous (right) materials. 107
- 6.2. Compared to the State A case (left) lightsoaking may produce more negatively charged defects which must be compensated by positive charge which can gather at the grain boundary edges (right), affecting both the band bending and the potential energy difference between the deep defects and the conduction band mobility edge. This effect can explain both the decreases of DLCP density upon lightsoaking and the decreases in minority carrier collection in the degraded state. 110

6.3. Under this model, the large DLCP signal in State B indicates band-to-band recombination (right) that occurs with an activation energy of half the crystallite bandgap, roughly 0.55eV. This could appear as a defect of energy 0.55eV in the DLCP measurement. In State A (left) holes occupying D- defects are too deep to emit to the valence band at the measurement frequency of 1100Hz.	112
A.1. State A fit parameters, Sample 16115. Note the deep defect energies of 0.7eV away from the interface and 0.4eV in a narrow region near the interface.	122
A.2. Intermediate State fit parameters, Sample 16115	123
A.3 State B fit parameters, Sample 16115. Note the energy shifts of the deep defects. The 0.7eV defect has become ~0.58eV and the near-interface defect has become 0.48eV. The deeper defect has an uncertainty of 0.05eV and the shallower defect has an uncertainty of 0.1eV.....	124
B.1. Sample structures were a very straightforward p-i-n configuration set atop a stainless steel specular back-reflector. Sometimes an Ag/ZnO textured back reflector was added to the device in order to facilitate light-trapping. Measurements on devices using such a back reflector are cited in the text. One result of this study was that such textured layers do indeed influence crystallite growth in these materials, which in turn influenced deep defect densities. Of course, light would be incident onto this device from the semi-transparent contact side.....	126

LIST OF TABLES

Table	Page
3.1. Raman crystalline fraction summary for two samples grown using the same recipe but deposited on different substrates, 16922 on textured Ag/ZnO and 16935 on specular stainless steel (SS). Samples 16966 and 16988 were deposited nearly three times thicker than the other two samples and were identical except for their final geometry, a typical n-i-p geometry in the case of 16966 and an a-Si:H sandwich geometry for 16988.....	54
3.2. Crystallinity and cell performance parameters for the devices featured in Figure 3.8. Crystalline fractions, $X_c \pm 0.05$, were estimated using Raman spectroscopy.....	60
5.1. Hole collection fractions, f_p , at 300K determined by the TPC and TPI signal ratios at a photon energies of 1.5 eV for a set of nc-Si:H sample devices of various amorphous volume fractions, X_a . State A and State B collection fractions are indicated by the superscripts. In all cases, the hole collection fractions, f_p , decrease after light soaking.	97

CHAPTER I

INTRODUCTION

1.1. A Brief Perspective

The modern age has developed quite a love affair with silicon. Although used in various glassy forms since the time of the ancient Mesopotamians, silicon's contemporary significance is clearly focused on its semiconducting properties. Indeed, the modern lifestyle owes a great deal to the abundance and usefulness of silicon as a semiconducting material. The ease with which semiconducting components are made has ushered in the age of inexpensive personal computing – with the attendant smartphones, digital media, supercomputers, gaming systems, digital cameras, flatscreen displays, etc. It is the easy mass production of crystalline silicon wafers, which are used to manufacture processors and memory modules that is the driving force behind this technology revolution. But this ready supply of crystalline silicon has, for the past 30 years, allowed the development of several other branches of semiconductor-based technology, not the least of which is the modern photovoltaic (PV) industry. Thus the abundance of inexpensive silicon wafers has revolutionized both the computing and PV industries and has allowed for the economic production of solar cells as well as microprocessors.

But since the first days of commercially available crystalline silicon solar cells in the 1960s the PV industry has matured. Market forces have driven PV developers toward making more efficient yet cheaper-to-produce solar modules. The end goal of this market

race is to develop PV technology that reaches “grid parity” – that magic figure with units of *production cost/produced watt* that will make the production of solar energy as cost effective as energy produced using carbon-based fuels¹. Speaking practically, decreasing *production cost/watt* for a solar module means making better quality (i.e. more highly efficient) modules using less raw material, taking less time to produce the module (higher deposition rates), and decreasing the necessary labor to install and maintain the modules. This has necessitated a shift in the PV industrial outlook from using thick and fragile crystalline silicon materials to *thin film* technologies, devices that are thin on the order of optical wavelengths but still operate as effective solar cell modules. It is at this technological transition where the story of amorphous silicon as a thin film photovoltaic begins and therefore also where the story of nanocrystalline silicon begins.

Nanocrystalline silicon (nc-Si:H) is the latest technological progression in silicon-based solar energy. Despite its good performance in this role, the electronic properties and structure/function relationships of nc-Si:H are very difficult to understand. The purpose of the current work will be to elucidate these relationships and to offer insight into how nc-Si:H behaves as a function of deposition conditions and post-deposition optical degradation.

The remainder of this Introduction will briefly outline the physical concepts and language required when discussing the properties of nc-Si:H. These concepts include the origin of the density of states in both crystalline and amorphous semiconductors,

¹ As this dissertation goes to press grid parity has been achieved in certain markets such as Hawaii, and is expected to be met in much of the USA by 2015. Grid parity is currently given an average value of US\$0.10/kWh in relatively sunny regions of OECD countries.

conductive properties of materials containing a mixture of crystalline and amorphous components, formation of the grain boundary potential, and carrier percolation.

1.2. The Ideal Crystal

The application of quantum physics to the description of solids is a great success of modern science. The theoretical body of solid state physics introduces the concepts of band structure and band gap – and therefore a description of why some materials conduct and others do not. An abbreviated approach [1] to this theory begins with a well ordered crystalline lattice, whose member atoms can be described using a set of vectors:

$$\mathbf{R} = n_1 \mathbf{a}_1 + n_2 \mathbf{a}_2 + n_3 \mathbf{a}_3 \quad (1.1)$$

The problem therefore is to consider the behavior of an electron in a potential $U(\mathbf{r})$ that is periodic in \mathbf{R} :

$$U(\mathbf{r} + \mathbf{R}) = U(\mathbf{r}) \quad (1.2)$$

Bloch's Theorem states that the Schrödinger equation with a periodic potential $U(\mathbf{r})$, $H\psi = [-\hbar^2 \nabla^2 / 2m + U(\mathbf{r})]\psi = E\psi$ is obeyed by a single independent electron of well-defined crystalline momentum \mathbf{k} :

$$\psi(\mathbf{r}) = u(\mathbf{r})e^{i\mathbf{k}\cdot\mathbf{r}} \quad (1.3)$$

This wavefunction, known as the “Bloch wavefunction” is chosen to have the form of a free electron wave function multiplied by a function $u(\mathbf{r})$ with the same periodicity as the crystalline lattice. In the free electron case, the ground state is constructed of electronic levels of energies $E(\mathbf{k}) = \hbar^2 k^2 / 2m$ below the Fermi level energy, E_F . For Bloch electrons this energy is written as a band of energies $E_n(\mathbf{k})$ where the quantum number n arises from

the many solutions to Schrödinger's equation that exist for any given value of \mathbf{k} . The energy bands $E_n(\mathbf{k})$ are periodic in the reciprocal lattice and are discrete for each n ; that is to say, they have an upper and lower bound.

Therefore the Fermi level energy position E_F , while unimportant in the free electron scenario, becomes crucially important in the crystalline solid. Since conduction can only occur in electronic bands that are partially filled with carriers, if E_F lies within an extensive energy band $E_n(\mathbf{k})$ the material will be a conductor, and conversely if E_F is situated such that under any condition there are *no* partially filled bands (such as within a large forbidden energy "gap", as shown in Figure 1.1) then the material will be an insulator.

Semiconducting solids represent an intermediate situation in which E_F lies in an energy gap between allowed Bloch electron energy bands that has a width of only a few eV or less. In this situation carriers can be thermally or optically excited across the energy gap and then participate in conduction. When this occurs, the energy band lying above the Fermi level is called the conduction band, E_C and the band lying below the Fermi level is called the valence band, E_V .

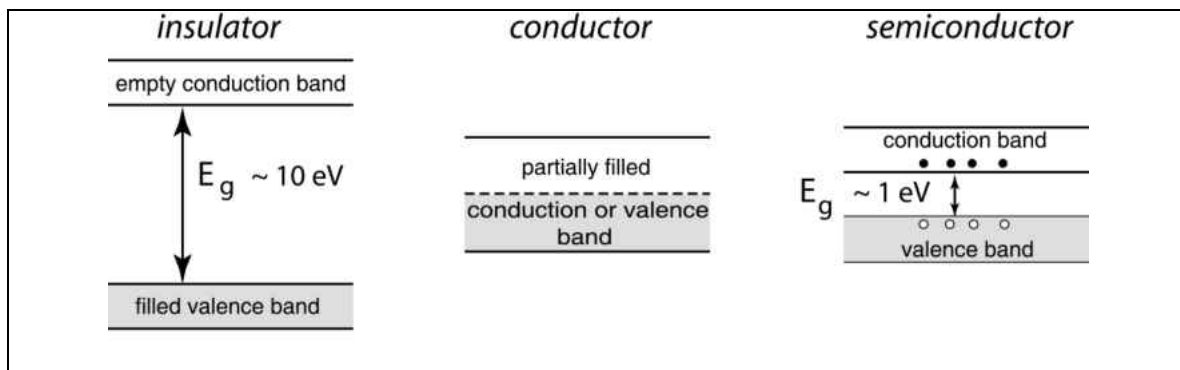


Figure 1.1. For crystalline solids, the Fermi level position in relation to boundary energies of the bands $E_n(\mathbf{k})$ determine whether the solid is conducting, insulating, or semiconducting.

Thus for crystalline solids we see that the existence of energy bands and forbidden energy regions (see Figure 1.2) between these bands arise from modifying free electron wavefunctions to functions sharing the periodicity of the crystalline lattice. From this it follows that the particular band structure in the neighborhood of the Fermi level, E_F , determines whether a material is an insulator, conductor, or semiconductor. The case of the *amorphous* solid adds substantial complication to these arguments. Indeed amorphous solids, by definition, do not possess the long-range order from which the Bloch electron/energy band theory is a direct consequence. Nonetheless amorphous conductors, insulators, and semiconductors do exist! A brief physical description of these materials and non-ideal crystals in general are provided in the next section.

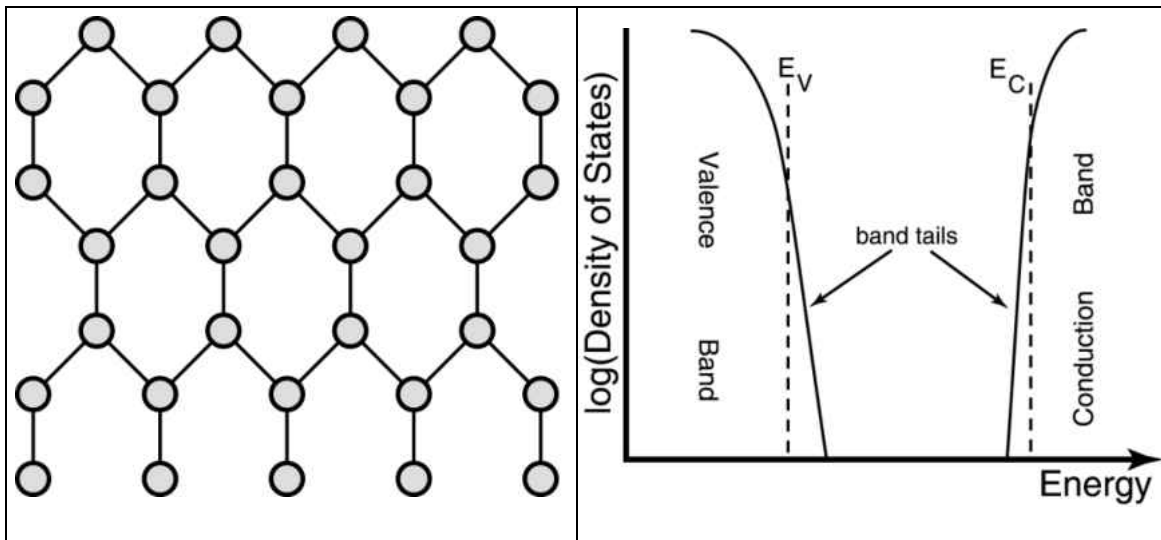


Figure 1.2. When a material exhibits short and long-range atomic order (left), the theory of Bloch electrons provides the theoretical basis for the formation of the valence band, the band gap, and the conduction band.

1.3. Amorphous and Non-Ideal Crystals

The basic three-dimensional properties of an amorphous solid is described well by the *continuous random network* (CRN) model, first introduced by Zachariasen in 1932. [2] In such a model, the regular crystalline network $\mathbf{R} = n_1 \mathbf{a}_1 + n_2 \mathbf{a}_2 + n_3 \mathbf{a}_3$ is replaced by a randomized network in which there exists no long range order and the primary structural feature of the system is the coordination of each individual member node, i.e. – how many bonds exist between the node and its neighbors. Figure 1.3(left) shows a CRN created by perturbing the crystalline network from Figure 1.2.

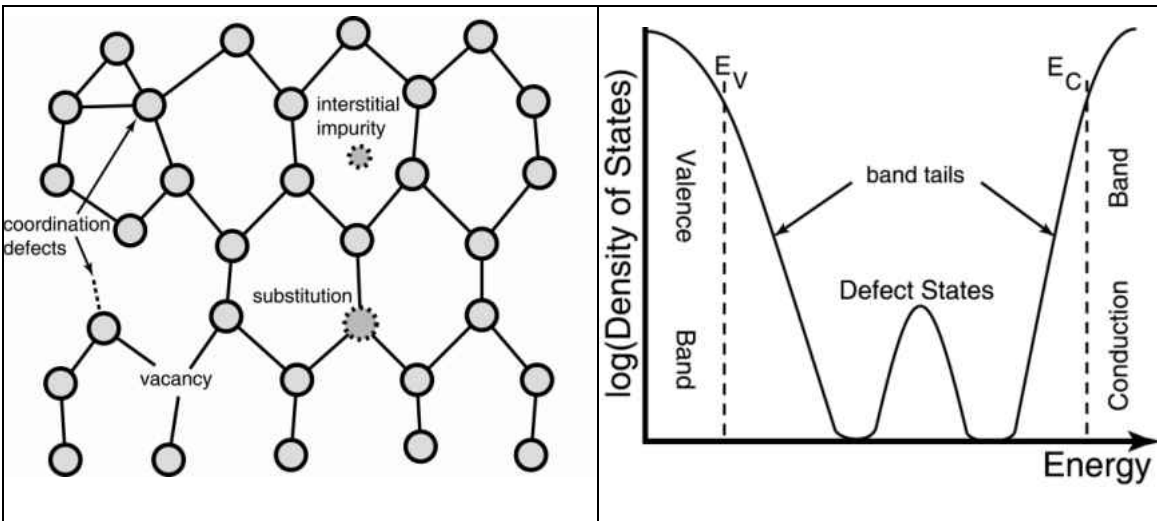


Figure 1.3. (left) A schematic continuous random network (CRN) of atoms which desire 3-fold coordination. Interstitial and substitution related defects can be found in all kinds of non-ideal networks, but over- and under-coordinated atoms are a feature only of a CRN. (right) A schematic sub-bandgap density of states for an amorphous semiconductor. Structural and thermal disorder produces broader band tails than in the crystalline case and localized defects introduce electronic states into the material's bandgap.

In addition to vacancy, substitution and interstitial defects, which may also be present in a crystalline network, the CRN shown in Figure 1.3 also contains coordination defects. These defects are a result of randomized atomic displacements and depending on the atoms involved, they may consist of both under- and over-coordinated nodes. Atomic coordination and its relation to defect states is discussed in the next section.

Chemical Bonding, Coordination Defects, and the “8-N” Rule

The CRN model of amorphous solids emphasizes the idea of atomic “coordination”. This refers to the chemical bonding environment of each individual atom in the amorphous network. Each atomic species has its own preferred bonding coordination, based on that species’ electronic valence. When atoms are brought together to form a solid, the valence electrons’ energy levels interact and split to form *bonding* and *anti-bonding* energy level states. To lowest mathematical approximation, these states result from creating molecular orbitals using linear combinations of atomic orbitals (LCAO) and represent in-phase and out-of-phase electronic arrangements, respectively. Physically, atoms form solids because the bonding orbitals are of energy lower than the isolated atomic orbitals.

In any solid, molecular orbitals will form in such a way as to minimize the bond energy. That is, electrons involved in covalent bonds will seek the lowest possible energy level available to them, first filling bonding states then only if necessary filling anti-bonding states. Since the number of electrons present in bonding states defines the desired number of covalent bonds for an atom, depending on the particular valences of the atoms involved in the bonding arrangement, any single atom may desire one, two, three, or four nearest neighbors.

This rule was formalized in the mid-20th century as the “8-N” rule. [3] This rule simply states that given a collection of elements, the optimum number of covalent bonds for each element, Z , is given by:

$$\begin{aligned} Z &= 8 - N; (N \geq 4) \\ Z &= N; (N < 4) \end{aligned} \tag{1.4}$$

for elemental arrangements of N valence electrons.

This discussion of bonding arrangements serves to illustrate the following important principle: *the continuous random network differs from the crystalline network in that it allows ambiguity in bonding coordination.* This means: (1) impurity atoms bond very differently in amorphous networks than in crystalline networks, allowing for dangling bond defects and over-coordination defects, and (2) structural changes can take place in amorphous materials as occupancy of bonding and anti-bonding states change and atoms re-coordinate to seek lower energy states.

Density of States

In the discussion of amorphous solids so far, there has been no mention of band structure. Indeed, the entire discussion of band structure of crystalline solids predicated on the notion of long-range atomic order such that electronic wave functions took a form that mirrored the spatial periodicity of the crystalline lattice. As it turns out, we don't need to throw all this theory out the door when talking about the electronic structure of amorphous solids. Instead, the bonding and anti-bonding orbitals that result from covalent bonding do a great job at explaining the presence of the valence and conduction bands. The short range interactions that define these molecular orbitals (not long range order effects) are the most

important factors [4] determining the general electronic structure of a material². For example, amorphous silicon is a semiconductor as well as crystalline silicon, and coal is just as much an insulator as diamond. This is why the definition of “amorphous solid” stresses no *long range* order, with short range order that is not too far a departure from their crystalline cousins.

The density of states for a typical amorphous material is shown in Figure 1.3 (right). The band tails are broader than in a crystalline material. This is because of the broader distribution of bond lengths and bond angles compared to a crystalline structure. The presence of coordination defects and atomic impurities and vacancies is seen in the middle of the forbidden energy gap. The Fermi level will also be situated somewhere between E_C and E_V . Indeed all aspects of the bandgap region are of importance to the overall electronic properties of the amorphous material as the exact distribution of states surrounding the Fermi level influence conduction, carrier trapping and recombination, and optical transitions in the material.

In summary, the important features of amorphous materials as compared to crystalline materials are: (1) the existence of coordination defects, (2) relative short range order, and (3) relative long range disorder. Results of these principles are that amorphous materials, in general, have band structures similar to their crystalline counterparts but with broader bandtails and (sometimes complex) distributions of defect states within the bandgap. All features of this bandgap region are important to the electronic properties of the amorphous material and complications in understanding the band gap density of states

² Local coordination interactions themselves cannot be used to completely explain the existence of a bandgap in disordered materials. Advanced calculation methods such as the method of pseudopotentials [5] have been helpful in solving this so-called “band gap paradox”. For a discussion of this subject see [6] p.456.

may arise from metastable coordination changes of atoms in the lattice as the number of electrons present in bonding and anti-bonding orbitals changes.

The topic of this thesis, however, is not crystalline or amorphous materials but rather the properties that result as crystalline and amorphous silicon materials are mixed. Therefore the goal of the next section is to introduce the general features of solid materials that are a mixture crystalline and amorphous components.

1.4. General Properties of Mixed Phase Materials

Materials that are a mixture of amorphous and crystalline components exhibit properties that can be modeled as a disordered combination of crystalline-like and amorphous-like electronic structure. These concepts are introduced in this section.

Definition of “Mixed Phase”

When speaking of inhomogeneously disordered semiconductors, the term “mixed phase” is often used. The “phase” spoken of here is not a thermodynamic phase (solid, gas, etc.) but rather is a synonym for “state of matter”. States of matter, as opposed to thermodynamic phase, are categorizations of matter based on their bulk properties. For example,

Crystalline Solid – a material in which inter-atomic attraction forces hold atoms in fixed positions relative to one another.

Glass or Amorphous Solid – a metastable solid state of matter with no long-range order among atomic constituents

Superfluid- a liquid state of matter characterized by zero viscosity and infinite fluidity; usually occurring at temperatures near absolute zero.

In this study, “mixed phase” refers to an inhomogeneous mixture of crystalline solids with amorphous solids. The act of mixing these two phases produces fluctuations in the band potential $U(\mathbf{r})$ which are caused not only by the presence of the two phases being mixed together, but also from secondary effects such as the presence of grain boundaries, voids, and regions of quasi-disorder.

Types of Two-Phase Systems

A comprehensive look at the types of two-phase systems is relevant to this thesis because nanocrystalline silicon can contain a wide variety of crystalline inclusions, ranging from the nominal $\sim 20\text{nm}$ crystallite inclusion to cone-like crystalline structures. These materials therefore exhibit a wide range of crystallinities and electronic behaviors. The basic features of which are outlined here.

Inclusions of Low Concentration

Perhaps the simplest two-phase scenario is the one in which one phase is of much higher concentration than the other. For example, if the volume fraction of the dominant phase, “phase a”, is given by X_a , then the fraction of “phase b” is $1-X_a$, then we shall require $X_b \ll 1$. In this case, the perturbations to $U(\mathbf{r})$ induced by each inclusion do not overlap and one may calculate an effective conductivity of the system using the potential distribution induced by an ellipsoidal inclusion [7] to yield:

$$\sigma = \sigma_a + X_b \frac{\chi(\sigma_b - \sigma_a)\sigma_a}{\sigma_b + \xi\sigma_a} \quad (1.5)$$

where ξ and χ are geometric factors on the order of 1 that reflect the shape of the

inclusions. [8] In this case, the effects of the inclusionary phase are minimal and the net conductivity effects are perturbational, as is reflected in Equation 1.5.

Matrix Systems

These systems are those in which neither phase dominates in concentration and the inclusionary phase does not cluster or form larger structures. It follows that for systems containing very large concentrations of inclusionary material, an ordered distribution of inclusions is required.

For illustrative purposes it is useful to consider the “cubic grain” model. [9,10] Since the cubic inclusions in this model don’t collide there is always a percolation pathway through the host material, so a main feature of this model is that the grain conductivity doesn’t matter very much. See Figure 1.4 for an illustration of a matrix system. For cubic grains of “phase b”, under the conditions $\sigma_a \ll \sigma_b$; $\lambda_1 \ll \lambda_2$:

$$\sigma \cong \frac{\sigma_a \sigma_b}{\sigma_a + \frac{\lambda_1}{\lambda_2} \sigma_b} \quad (1.6)$$

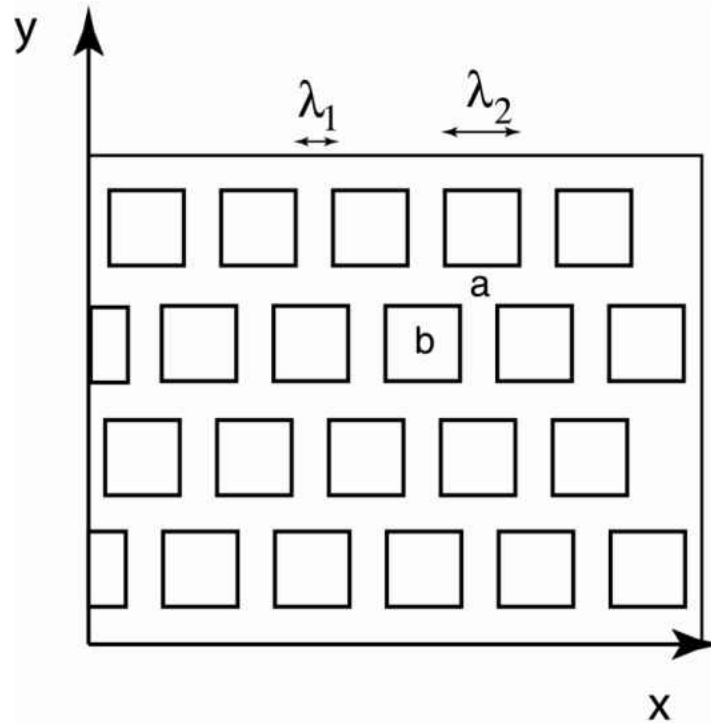


Figure 1.4. The “cubic grain model” is a good way of modeling conduction in a well-mixed two-phase material in which the inclusionary cubic grains (“phase b” above) do not amalgamate.

This result states for a material such as nc-Si:H, where the inclusions are of high conductivity, the conducting properties of the film will be primarily determined by the host material. It is worth noting, however, that σ is highly sensitive to changes in λ_1/λ_2 . This means that materials classified at ‘matrix systems’ can be highly sensitive to conditions that affect this spacing, such as film stress.

Well-Mixed Systems

Naturally, the most complex two-phase mixture is the one in which both phases exist in relatively equal concentrations and their spatial statistical distributions are similar. This kind of material is often called a “statistical mixture” and its properties are calculated

using the effective medium theory.

The effective medium theory cleverly assumes a hypothetical medium of conductivity σ in which two additional phases are present with conductivities σ_a and σ_b . If these additional phases exist as spherical inclusions then the fields inside the inclusions are expressible as

$$E_i \cong \frac{3\sigma}{2\sigma + \sigma_i} E; i = a, b \quad (1.7)$$

Where E is the field in the hypothetical medium, σ . Next we make the critical (and intuitive) assumption that the field *outside* the inclusions, E , is equal to the average of fields *inside* the inclusions, or $E = (1 - X_a)E_b + X_a E_a$. Making this substitution in Equation 1.7

we find an expression quadratic in σ which has the solution:

$$\sigma = \frac{1}{4} \left[\gamma + \sqrt{\gamma^2 + 8\sigma_a \sigma_b} \right]; \gamma = (2 - 3X_a)\sigma_b + (3X_a - 1)\sigma_a \quad (1.8)$$

However, this solution is approximate and notably fails when describing critical phenomena, such as insulator-to-conductor transitions.

Formation of the Grain Boundary Potential

In the previous sections conductivity in simple two-phase systems was discussed. In each of these models resulting conductivities were calculated for different geometries of crystalline inclusions in a host material by simply considering the bulk conductivities of each phase respectively. In actual materials, especially in polycrystals, it is common for regions of the inclusionary phase (which we consider here to be crystallites) to come into

contact with one another, forming “grain boundary” regions which can induce potential barriers in the material. These potential barriers can alter the conductivity of the two-phase mixture beyond what the two-phase models discussed above would predict.

For n-type crystallites with p-type interface states embedded in an amorphous matrix, one simple analysis [11] describes the resulting potential barrier, Δ , induced by N_i interface states (n_i of which are charged) between crystallites of effective doping N_D as:

$$\Delta = \frac{\pi e^2 n_i^2}{2\kappa N_D} \quad (1.9)$$

where κ is the dielectric constant of the crystallites. For large densities of interface states, N_i , the surface defect distribution will become pinned to the Fermi level (Figure 1.5 part a) and only some of the states will be charged (empty of electrons) and the result is a large interface potential.

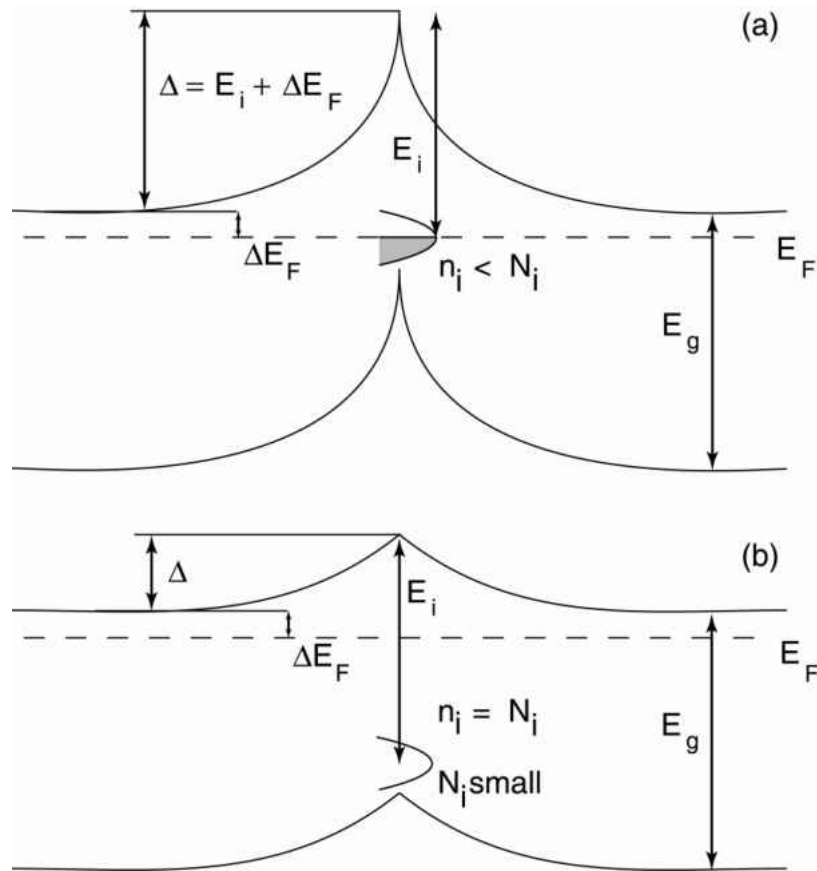


Figure 1.5. Potential barriers can be produced in grain boundary (GB) regions by the presence of charged defects. If a large number of defects are present at a GB, then the Fermi level can become pinned to the defect distribution, thus inducing a potential barrier in to the conduction and valence bands (a), if the number of GB defects is small, the potential barrier is lower (b).

For small densities of interface states very few of the states will be occupied, the states will not be pinned to the Fermi level and the band bending will be slight. This result described by Equation 1.9 is approximate, of course, and is only truly applicable to a material consisting of large crystallite grains of size d greater than the

Debye screening length, $d \gg \sqrt{\frac{\epsilon kT}{nq^2}}$. Equation 1.9 also ignores effects such as the

intersection of more than two crystallites, potential fluctuations from small angle lattice intersections, etc. *In the case that the crystallite inclusions are small*, as is the case with nc-Si:H, then the crystallite inclusions will become fully depleted and carriers will occupy the GB defect states. In this case the GB potential barrier heights will fluctuate with a mean amplitude:

$$\Delta \sim \frac{e^2 N_D^2 d^2}{\kappa} \quad (1.10)$$

Carrier Percolation

In any semiconductor with a randomly varying potential $U(\mathbf{r})$ of sufficient amplitude, one may speak of carrier *percolation*³ through the material. Formulation of the percolation theory is as follows: for a potential “landscape” $U(\mathbf{r})$, choose a threshold potential, V and allow the conduction of carriers only in regions where $U(\mathbf{r}) < V$. There will be a critical value of this threshold for which if V were smaller carrier conduction across the entire potential landscape would be impossible. This critical value of V is called the percolation level and its specific value is a property of $U(\mathbf{r})$. A classic 2-D descriptive example of percolation is to imagine a completely white chessboard on which one randomly begins to color individual squares black. In this case the percolation threshold will be the density of black squares at which an ant walking across the chessboard need

³ There are different kinds of percolation problems which are differentiated chiefly in that the underlying structures through which conduction is taking place changes; for example “site (vertex) percolation” or “bond (edge) percolation”. Here, we refer to percolation through a continuum system, or “continuous percolation”.

touch no white squares in order to reach the other side. For 2-dimensional random symmetric potentials the critical space portion defined by $U(\mathbf{r}) < V$ required for percolation is $X_c=0.5$. One may compare this number to the critical filling fraction for black squares on a chessboard, which is $X_c\sim 0.6$.

Percolation in 3-dimensional systems is more complex and determining X_c can be quite tricky as it depends on the local nature of $U(\mathbf{r})$. For example, a $U(\mathbf{r})$ constructed from spatially randomized Gaussian potentials [12] can have X_c as small as ~ 0.15 . One may compare this to 3-D site percolation (the 3-D analog of the chessboard) which has a critical volume density of $X_c\sim 0.31$. [13] Likewise a 3-D system of close packed spheres yields $X_c=0.289$.

The percolation problem in real materials becomes even more complex when bipolar conductivity is considered. For an intrinsic or compensated semiconductor the percolation levels of electrons in the conduction band and holes in the valence band (V_c^n and V_c^p respectively) can be situated in the potential landscape in such a way that electron and hole contributions to the conductivity may be similar. [8] Therefore a material may appear highly intrinsic, but in reality the equitable bipolar conduction may be a result of a sufficiently inhomogeneous $U(\mathbf{r})$.

1.5. Summary and Purpose of This Work

Nanocrystalline silicon (nc-Si:H) is the latest technological progression in photovoltaics that began with the mass production of crystalline silicon devices then led to thin film silicon technology, an area currently dominated by amorphous silicon materials. A mixture of crystalline and amorphous silicon, in one respect nc-Si:H is the form of

microcrystalline silicon with the smallest crystallite sizes (typically about 20nm). The electronic properties resulting from this physical structure is complex and exhibits properties of both ordered and disordered silicon semiconductors as well as properties related to two-phase semiconductor mixtures. These latter properties include conductivity dependencies on the distribution and volume density of nanocrystallites, conductivity dependencies on the presence of grain-boundary related potential fluctuations caused by defects, bipolar conductivity issues related to the different potential landscapes of the valence and conduction bands, and sensitivity of optical absorption to the phase mixture. These complications exist in addition to any issues associated with the study of deep gap defects in a-Si:H, a topic which has been debated now for several decades.

The struggle to understand nc-Si:H is perhaps warranted, however. Over the past decade this material has been evaluated for use in multijunction solar cell devices as the low optical gap component (in some cases utilized alongside a-Si:H and a-SiGe:H as the intermediate gap components [14-17]). Indeed, the record stabilized efficiency for multijunction a-Si:H based solar cells is currently held by a triple junction cell utilizing nc-Si:H. [18]

Nanocrystalline silicon shows enhanced conversion efficiency at IR wavelengths, enhanced carrier mobilities, and resilience to light-induced degradation of its electronic properties. These qualities underscore the potential importance of this material for the future development of a-Si:H-based PV technologies and motivate the physical understanding of nc-Si:H.

The purpose of this thesis is to elucidate some structure/function relationships of nc-Si:H using a collection of experimental methods that have previously been very

successful in describing the electronic and structural properties of a-Si:H, a-SiGe alloys, CIGS, and other materials. Some of these measurement methods are standard, such as Raman spectroscopy and secondary ion mass spectroscopy (SIMS) but others are more specialized. Particularly, this thesis will focus on the use of junction capacitance-based measurements to determine deep gap densities of states, optical absorption, and carrier transport properties of nc-Si:H. These measurement methods will be discussed, the results of their application will be shown, and finally, a microscopic model will be presented to describe the stable and metastable properties of nc-Si:H.

CHAPTER II

EXPERIMENTAL TECHNIQUES

2.1. Formation of the *pn* Junction

At their most basic, photovoltaics are simply rectifying junctions: diodes. They are either *pn* junctions, Schottky barriers or heterojunctions. All of these devices form rectifying potentials at their metallurgical interface via a process that is most easily explained in the case of the *pn* junction. Figure 2.1 shows the two halves of the *pn* junction.

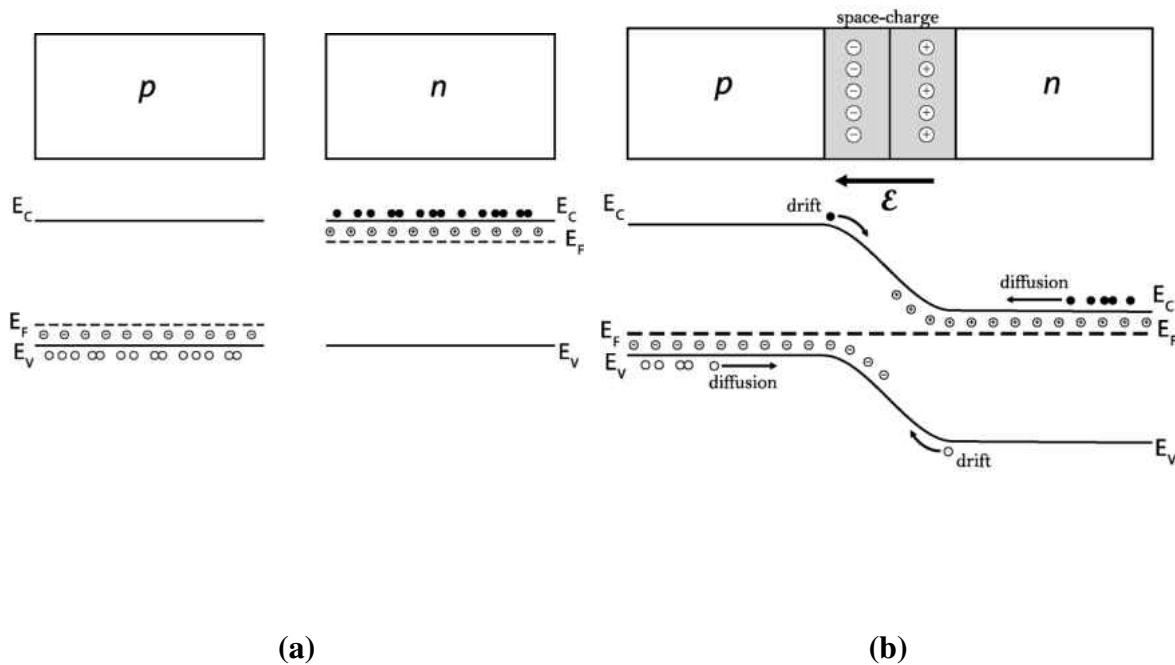


Figure 2.1. The depletion capacitance is formed when two materials of different bulk Fermi level energies (a) are brought into conductive contact. Charged regions form on each side of the junction until, at thermal equilibrium conditions, drift currents exactly cancel the diffusion currents (b).

The p side, doped with acceptors and the n side doped with donors. When these two halves are brought into conductive contact the free charge immediately begins to redistribute itself over the entire device by a diffusive process. As this happens, the electric fields of the donors (for the case of the n type material) and acceptors (for the p type material) are left uncompensated by the free charge and an electric field begins to form at the interface. This process continues until the drift current induced by the newly formed *space charge region* (or *depletion region*) exactly cancels the *diffusion current*. After this equilibrium is reached, what will have formed will be a rectifying junction, a structure that favors the flow of current in one direction only. For the figure shown, the flow of electrons is impeded from flowing from right to left.

Once formed, one can model the electronic behavior of this structure. It is standard to treat such a junction as a parallel resistor and capacitor in series with a series resistance. In this model the series resistance represents conduction through the bulk material, measurement cables, etc. The parallel resistance represents leakage through a non-ideal metallurgical interface, and C represents the capacitance attributed to the depletion region, which is a dipole layer of width W such that in the absence of AC signals $C = \frac{\epsilon A}{W}$.

It is important to recognize here that C actually consists of two capacitors in series: $\frac{1}{C} = \frac{1}{C_p} + \frac{1}{C_n}$. Where the subscript denotes the side of the junction where each capacitance exists. C_p and C_n will behave differently under application of bias and changes of temperature, but this is a complication in the analysis which is routinely ignored by claiming the junction to be “single sided”. That is, one side is so heavily doped that its

width is very small and so does not contribute significantly to C. However it is always prudent to remember that this “extra” capacitance exists as well as capacitances due to other layers in the device, which are also routinely ignored.

2.2. General Formalism of the Depletion Capacitance

Junction capacitance measurements were developed to characterize the properties of crystalline semiconductors. [19,20] However, such techniques are also useful when applied to the study of amorphous and mixed phase materials, even though energetic states in the bandgap of such materials are dispersed in energy. These measurements probe the rectifying barrier formed when materials have dissimilar Fermi levels are brought into contact (see previous sections). When a depletion region is formed in such a way, an externally applied bias δV_{ext} will alter the depletion region width. In the case of an applied reverse bias, the depletion region width will increase, extending the edge of the depletion region further into the bulk of the material and changing the space charge by an amount δQ . The capacitance represented by this response is then given by $C = \delta Q / \delta V_{ext}$. In this equation δQ represents a *net* charge density response upon application of δV_{ext} . The relationship between applied voltage and net charge change is given by Poisson’s equation:

$$\frac{d^2\psi}{dx^2} = \frac{\rho(x)}{\epsilon} \quad (2.1)$$

where ψ is the potential as measured from the conduction-band edge in the neutral bulk material, ϵ is the dielectric constant for the semiconductor, and the junction interface position is represented by $x=0$. This equation is easily integrated between $x=0$ and the bulk region ($x=b$) where ψ and $d\psi/dx$ are zero by applying the identity:

$$\frac{d}{dx} \left(x \frac{d\psi}{dx} \right) = \frac{d\psi}{dx} + x \frac{d^2\psi}{dx^2} \quad (2.2)$$

so that

$$x \frac{d\psi}{dx} \Big|_0^b = \psi(b) - \psi(0) + \int_0^b x \frac{d^2\psi}{dx^2} = -\psi(0) + \int_0^b \frac{x\rho(x)}{\epsilon} = 0 \quad (2.3)$$

Since the bulk region of the sample is electrically neutral we can extend the integration to infinity, thus yielding an expression for the interface potential:

$$\psi(0) = \int_0^\infty \frac{x\rho(x)}{\epsilon} \quad (2.4)$$

If one now shifts this interface potential with respect to the bulk potential by applying an external voltage bias: $\psi(0) \rightarrow \psi(0) + \delta V_{ext}$ then there will be a corresponding shift in charge density, $\delta\rho(x)$, throughout the depletion region. Assuming no significant changes of $\rho(x)$ on the Debye length scale in the sample (i.e. the sample is spatially uniform) and defining an active cross-sectional area A , the total charge shift due to δV_{ext} is given by

$\delta Q = A \int_0^\infty \delta\rho(x) dx$, so capacitance can be rewritten:

$$C = \frac{\delta Q}{\delta V_{ext}} = \frac{\epsilon A}{\langle x \rangle} \quad (2.5)$$

where $\langle x \rangle$ is the normalized electric dipole moment of the charge response to δV_{ext} given

by

$$\langle x \rangle = \frac{\int_0^\infty x \delta\rho(x)}{\int_0^\infty \delta\rho(x) dx} \quad (2.6)$$

It is important to remember that Equation 2.6 is valid for any junction capacitance measurement. In fact, $\langle x \rangle$ is *always* the quantity measured when one speaks of measuring a depletion width via capacitance techniques⁴. It is worth stating explicitly two results that come from the appearance of $\langle x \rangle$ in the expression for capacitance. First, C is the result of weighted spatial averages of charge response. Thus if charge response to a voltage perturbation is highly non-local, then C is the result of the average response. Secondly, constant dipole layers will not affect the value of $\langle x \rangle$ since any such layer will be defined as $\delta\rho(x)=0$. Therefore, immobile charge in the material bulk and elsewhere nearby the capacitance junction system are of no consequence.

2.3. Depletion Capacitance and Gap State Profiling in Crystalline Semiconductors

The general formalism outlined above can be solved exactly for several specific cases. Two of these cases are the depletion approximation case (“abrupt junction” [21]) and the continuous density of states scenario. The depletion approximation method is described as follows.

For crystalline semiconductors, it is often the case that the approximation can be made that the charge density, $\rho(x)$ contained in depletion region is constant throughout and quickly changes to zero at the depletion region/bulk interface. This, consequently, is the result of *gap states of discrete energy*. [21] In this scenario, Poisson’s equation is easily integrated to yield an expression for the electric field:

$$E(x)=(x-W)Nq/\epsilon \quad (2.7)$$

⁴ Instances in which $\langle x \rangle$ can be taken to represent the actual depletion region width W are special cases. One must always keep in mind that charge may respond to an externally applied voltage from many different regions of the sample.

where N is the constant number density of charge and $Nq=\rho$ is the charge density. Under the depletion approximation $\langle x \rangle$ has simply become the depletion region width, W . The band potential is given by integrating this result a second time:

$$\psi(x) = (x-x^2/2W)E(0) \quad (2.8)$$

Given the boundary condition $\Psi(0)=0$, the total voltage drop across the junction is expressed by the value of the band bending function at the depletion region edge. The total voltage drop must also be given by the built-in potential of the junction plus any externally applied voltage bias, or $\Psi(W)=V_{bi}-V_{app}$, where $V_{app}<0$ corresponds to reverse biasing the junction. Using this identity, the depletion width is given by:

$$W = \sqrt{2\varepsilon(V_{bi} - V_{app})/qN} \quad (2.9)$$

Given a well-defined device area A , the total charge in the depletion region is then given by

$$Q = AqNW \quad (2.10)$$

and the junction capacitance is

$$C = \frac{\delta\rho}{\delta\Psi} = \frac{\varepsilon A}{\langle x \rangle} = \frac{\varepsilon A}{W} \quad (2.11)$$

This is the well-known expression for a parallel plate capacitor of area A and plate separation W . This result is easily understood by recognizing that the depletion approximation has pre-supposed that all charge change with applied voltage ($\delta\rho/\delta\Psi$) occurs at the depletion region edge. Therefore, we have effectively defined the result to be so. However, for many crystalline semiconductors this approximation is quite valid. Indeed, this simplicity gives rise to a clever way of determining rather arbitrary spatial distributions

of donor states. Since any δQ as the result of an applied voltage δV occurs only in a localized region at the depletion edge the donor density profile is found by observing the rate of capacitance change with an applied bias:

$$N(W) = \frac{2}{q\varepsilon} \left(\frac{1}{\frac{dC^{-2}}{dV}} \right) \quad (2.12)$$

Therefore a plot of $1/C^2$ vs V yields a slope proportional to $N(W)$. This handy result is called the *profiler's equation* and is valid only under the depletion approximation, therefore requires simple distributions of gap defects in which gap states are single valued in energy and are not energetically disperse. This is opposed to actual gap state distributions in disordered semiconductors where typically both of these assumptions fail.

2.4. Depletion Capacitance and Gap State Profiling in Disordered Semiconductors

In a disordered semiconductor, the depletion approximation is not very useful. This is because gap states in disordered materials generally 1) exist as energetic distributions or bands rather than discrete “defect levels” and 2) co-exist spatially but are multivalued in energy. Therefore, as the measurement of capacitance is made: $C = \delta Q / \delta V$ *some* charge responds from near the depletion edge at $x=W$, and *some* charge responds from deeper within the depletion region. In this case a more involved treatment of charge response must be considered [22,23] where the DC charge density is of the form:

$$\rho(x) = \int_{-\infty}^{\infty} [f(E', E_f^0, T) - f(E', E_f^0 - \psi(x), T)] g(E', x) dE' \quad (2.13)$$

where E_f^0 is the Fermi level with respect to E_C in the bulk material and $\psi(x)$ is zero in the

bulk material.

In general, the occupation of a gap state in a semiconductor is described by the carrier trapping and emission rates for that state. For a gap state at energy depth $E=E_C-E_d$ the thermal emission frequency of electrons from that state into the conduction band is

$$v_n = \frac{1}{\tau} = v_o e^{-(E_C-E_d)/kT} \quad (2.14)$$

Where k is the Boltzmann constant, T is the temperature, and v_o is the thermal emission prefactor for electrons. Also known as the ‘attempt frequency’ or the ‘attempt to escape frequency’, v_o is a parameter that appears in energetic transitions of carriers that involve thermal energy contributions. [24] The attempt frequency has many physical interpretations that relate to a broad array of concepts such as entropy (see discussions on the Meyer-Neldel Rule [25,26]), carrier capture cross-sections (via detailed balance arguments, shown below), quantum mechanical matrix elements for energetic transitions, and phonon dispersions. Experimentally, the attempt frequency has been found to have a value roughly equal to the phonon frequency; typically $\sim 10^{13} \text{ s}^{-1}$ in amorphous silicon-like materials.

Under thermal equilibrium conditions, the thermal emission rate will be identically equal to the carrier capture rate for the gap state in question. The capture rate for a gap state is proportional to the density of unoccupied gap states as well as the free carrier density, with a proportionality constant that reflects the thermal velocity of free carriers and the gap state capture cross section. [21]

$$R_{cap} = v_{th} \sigma_n N_d (1 - f) \quad (2.15)$$

Setting the capture rate equal to the emission rate $R_{em}=v_n N_d f$ yields an expression

for the attempt frequency:

$$v_o = v_{th} \sigma_n N_C(T) = v_{oo} T^2 \quad (2.16)$$

Equation 2.14 implies that for a forced frequency response, i.e. – an AC measurement of capacitance at angular frequency ω , there exists a *thermal emission energy* E_e for which gap states of energy depth $E_C-E_d > E_e$ can not respond to the measurement frequency. Using Equation 2.14 and including the explicit T dependence of the attempt frequency from Equation 2.16, we obtain:

$$E_e = -kT \ln\left(\frac{\omega}{2\pi v_{oo} T^2}\right) \quad (2.17)$$

To a good approximation, the Fermi function can be considered a step function. In this case, the charge density affecting the junction capacitance at a measurement frequency and temperature ω , and T is:

$$\rho_s = \int_{E_C-E_e}^{E_f} g(E, x) dE \quad (2.18)$$

With some concept of how the extended density of states affect the space charge density, we may now consider the capacitance response of a disordered semiconductor. We will follow the derivation of Heath, *et. al.* [27]

Firstly, the interface potential obtained from solving Poisson's equation (Equation 2.1) takes a different form in disordered semiconductors. [23,27] For a voltage perturbation δV , applied for a time of order $1/\omega$, charge in occupied gap states cannot respond out to a

position $x = x_e$; which is defined as the location at which $E_C - E_F = E_e(\omega, T)$. At distances greater than x_e gap states lying in the energy range between E_F and E_e will respond to the voltage. Therefore, the interface potential can be written with two terms:

$$\psi_o(0) = \int_0^{x_\varepsilon} \frac{x\rho_o(x)}{\varepsilon} dx + \int_{x_\varepsilon}^{\infty} \frac{x\rho_o(x)}{\varepsilon} dx \quad (2.19)$$

where subscripts denote parameters *prior* to applying the voltage. After δV is applied, it must be true that $\psi(0) = \psi_o(0) + \delta V$ and the location at which $E_C - E_F = E_e(\omega, T)$ changes to $x_e = x_{e0} + \delta x$, which we shall write as $x_e + \delta x$ for convenience.

As the voltage is applied, for $x < x_e$ the charge density will remain $\rho_o(x)$. Between x_e and δx , $\rho(x)$ will be limited by charge emission from the gap state to the conduction band; this charge density we label as ρ_ε . Therefore:

$$\psi(0) = \psi_o(0) + \delta\psi = \int_0^{x_\varepsilon} \frac{x\rho_o(x)}{\varepsilon} dx + \int_{x_\varepsilon}^{x_\varepsilon + \delta x} \frac{x\rho_\varepsilon}{\varepsilon} dx + \int_{x_\varepsilon + \delta x}^{\infty} \frac{x\rho(x)}{\varepsilon} dx \quad (2.20)$$

If we now assume that the defect properties of the semiconductor vary slowly on the scale of δx , then the final integral in Equation 2.20 is merely the charge density prior to applying δV , but shifted by an amount δx . Therefore,

$$\psi(0) = \int_0^{x_\varepsilon} \frac{x\rho_o(x)}{\varepsilon} dx + \left[\frac{x^2\rho_\varepsilon}{2\varepsilon} \right]_{x_\varepsilon}^{x_\varepsilon + \delta x} + \int_{x_\varepsilon + \delta x}^{\infty} \frac{x\rho_o(x - \delta x)}{\varepsilon} dx \quad (2.21)$$

Under these assumptions, the total change of charge with the application of δV

should simply be

$$\delta Q = A\rho_\epsilon \delta x \quad (2.22)$$

Therefore to fully solve the capacitance response $C=\delta Q/\delta V$, our only challenge is to express δx in terms of the charge density and δV . Using Equations 2.19 and 2.21 we can cancel out an integral term and write

$$\delta V = \psi(0) - \psi_o(0) = \left[\frac{x^2 \rho_\epsilon}{2\epsilon} \right]_{x_\epsilon}^{x_\epsilon + \delta x} + \int_{x_\epsilon + \delta x}^{\infty} \frac{x \rho_o(x - \delta x)}{\epsilon} dx - \int_{x_\epsilon}^{\infty} \frac{x \rho_o(x)}{\epsilon} dx \quad (2.23)$$

We may shift the center integral using $y=x-\delta x$ to find

$$\delta V = \psi(0) - \psi_o(0) = \left[\frac{x^2 \rho_\epsilon}{2\epsilon} \right]_{x_\epsilon}^{x_\epsilon + \delta x} + \int_{x_\epsilon}^{\infty} \frac{(y + \delta x) \rho_o(y)}{\epsilon} dy - \int_{x_\epsilon}^{\infty} \frac{x \rho_o(x)}{\epsilon} dx \quad (2.24)$$

which allows a further cancellation of terms. After once again relabeling variables we reach

$$\delta V = \psi(0) - \psi_o(0) = \left[\frac{x^2 \rho_\epsilon}{2\epsilon} \right]_{x_\epsilon}^{x_\epsilon + \delta x} + \int_{x_\epsilon}^{\infty} \delta x \frac{\partial^2 \psi}{\partial x^2} dx \quad (2.25)$$

or

$$\delta V = \frac{\rho_\epsilon}{2\epsilon} [(x_\epsilon + \delta x)^2 - x_\epsilon^2] + \delta x F(x_\epsilon) \quad (2.26)$$

where $F(x_\epsilon)$ is simply the electric field at x_ϵ . Now, solving this equation for δx using the quadratic formula:

$$\delta x = \left(\frac{\varepsilon F}{\rho_e} + x_e \right) \left[1 - \sqrt{1 + \frac{2\rho_e \delta V \varepsilon}{(F\varepsilon + \rho_e x_e)^2}} \right] \quad (2.27)$$

and expanding the square root term $\sqrt{1-x} \approx 1 - \frac{x}{2} - \frac{x^2}{4} + \mathcal{O}(x^4)$ in powers of δV gives

$$\delta x \approx \frac{\varepsilon}{(\varepsilon F(x_e) + \rho_e x_e)} \delta V - \frac{\rho_e \varepsilon^2}{2(\varepsilon F(x_e) + \rho_e x_e)^3} \delta V^2 + \dots \quad (2.28)$$

So the capacitance response is expressible as

$$C = \frac{\delta Q}{\delta V} \approx \frac{A\rho_e \varepsilon}{(\varepsilon F(x_e) + \rho_e x_e)} - \frac{A\rho_e^2 \varepsilon^2}{2(\varepsilon F(x_e) + \rho_e x_e)^3} \delta V + \dots \quad (2.29)$$

2.5. Drive Level Capacitance Profiling

The Drive Level Capacitance Profiling (DLCP) method was developed [23,28] to provide a measurement of ρ_e , as described in the preceding section. That is, DLCP provides a measurement of densities of state in the gap down to an experimentally controllable energy depth E_e from the mobility band edge and at a spatial coordinate $\langle x \rangle$, the value of which is controlled by applying a DC bias voltage. Fundamentally, the DLCP measurement relies on a measurement of the junction capacitance as a function of a small AC voltage amplitude. Such a capacitance response can be described by $C=C_0+C_1\delta V+C_2 \delta V+\dots$

Comparing this form with Equation 2.29 above we see that

$$N_{DL} \stackrel{\text{def}}{=} -\frac{C_0^3}{2qA^2C_1} = \frac{\rho_e}{q} = n + \int_{E_c - E_g(T, \omega)}^{E_f} g(E, x) dE \quad (2.30)$$

where n is the majority free carrier density and the integral, which is dependent on $E_e(T, \omega)$,

represents the density of charge responding from occupied gap states. Therefore, measuring C for several values of AC voltages δV and empirically describing this response with a linear or quadratic function, a density of responding charge is found which is the sum of the free carrier density and responding deep states. This density we call the “drive level defect density” and it is commonly denoted by “ N_{DL} ”.

Note that it is important when applying these AC voltages to insure that the value of x_e does not vary appreciably from its value when $\delta V=0$. This means that a DC voltage offset is required such that $V_{total} \equiv V_{DC} + \delta V_{rms} = constant$. Once N_{DL} is found using this method, the distance from the junction at which N_{DL} responds is given by $\langle x \rangle$ (Equation 2.6), but to first order is approximated by $x_e = \epsilon A / C_0$. A spatial profile of N_{DL} values is generated by repeating the capacitance AC response analysis at several DC voltage biases, maintaining the condition $V_{total} = constant$ for each V_{DC} .

2.6. Optical Measurements

Optical measurements of semiconductors rely on the absorption, transmission, and reflection of light, usually between the wavelengths of $\sim 300\text{nm}$ and $2.5\mu\text{m}$, from the semiconductor surface or bulk. The most straightforward of these measurements is an transmission/reflection measurement. These measurements consist of measuring the transmitted (T) and reflected (R) components of a constant wave beam passed through a thin film of material of thickness d . This is a useful way of measuring the absorption coefficient $\alpha(\lambda)$ and thus the optical bandgap of a material, since the absorption coefficient is related to these parameters by

$$T = (1 - R)e^{-\alpha d} \quad (2.31)$$

But the transmission measurement is severely limited in its ability to provide useful information at optical energies below the semiconductor bandgap. This is because experimentally it is very difficult to measure the coefficients T and R to the accuracy required to detect the presence of mid-gap defect states that often have densities a factor 10^4 lower than the extended states comprising the conduction and valence bands. Therefore, several methods were developed in the last few decades to allow experimenters to optically probe mid-gap defects with the required sensitivity.

Two of the most common *sub-bandgap absorption measurements* used currently are Photothermal Deflection Spectroscopy (PDS) [29] and the Constant Photocurrent Method (CPM). [30] These measurements, like the Transient Photocapacitance (TPC) and Transient Photocurrent (TPI) methods used in this study, effectively measure generated carrier populations instead of transmitted or reflected light. This is the nature of their sensitivity advantage over transmittance type measurements.

The PDS technique measures the light-generated carrier population by monitoring heat energy produced by carrier recombination. One drawback to this technique is that the probe beam used to measure this heat gives information about densities of states in the bulk of the material as well as near the material surface. [29] Since densities of states at the material surface can be quite large, the sensitivity of PDS to densities of bulk states can be masked by large densities of surface states.

Alternately, the CPM technique monitors what light intensity $I(\lambda)$ is needed to produce a constant photocurrent over a range of wavelengths, thereby keeping a constant

light-induced carrier population over all optical excitation energies. [30] Straightforward and robust, the CPM method provides excellent sub-bandgap spectra but requires a particular coplanar measurement geometry that is typically not satisfied by traditional solar cell p-i-n configurations. Therefore CPM requires specially prepared samples.

Additionally, CPM is by its nature ambipolar and cannot distinguish majority and minority carrier processes. Some benefits of the measurement methods used in this study, Transient Photocapacitance and Transient Photocurrent, is that 1) they can be applied to *bona fide* solar cell structures and 2) they can resolve majority/minority carrier processes. These measurements are described in the next section.

Transient Photocapacitance and Transient Photocurrent

Just like the Drive Level (DLCP) method is based on measurement of the junction capacitance to determine mid-gap densities of states, the Transient Photocapacitance (TPC) and Transient Photocurrent (TPI) methods also measure a δQ in the space charge region. The most common approach when conceptually introducing these measurements is to relate them to the well-known Drive Level Transient Spectroscopy (DLTS) method [31] pioneered by Lang in 1974. The basic idea is that when an optical or voltage pulse is applied to a reverse-biased junction a non-equilibrium condition is achieved; after the pulse is removed an exponentially transient return to equilibrium is seen, shown in Figure 2.2. The transient effect can be measured in two ways: by monitoring the junction capacitance (TPC) or by monitoring the total current (TPI). In either case thermal processes will be the cause of the return to equilibrium, but this equilibration can be enhanced optically, as is shown in Figure 2.2 part (c). It is the effect of the optical pulse on the

redistribution of carriers during equilibration that is the spectroscopic principle behind TPC and TPI. Both experiments are performed as follows.

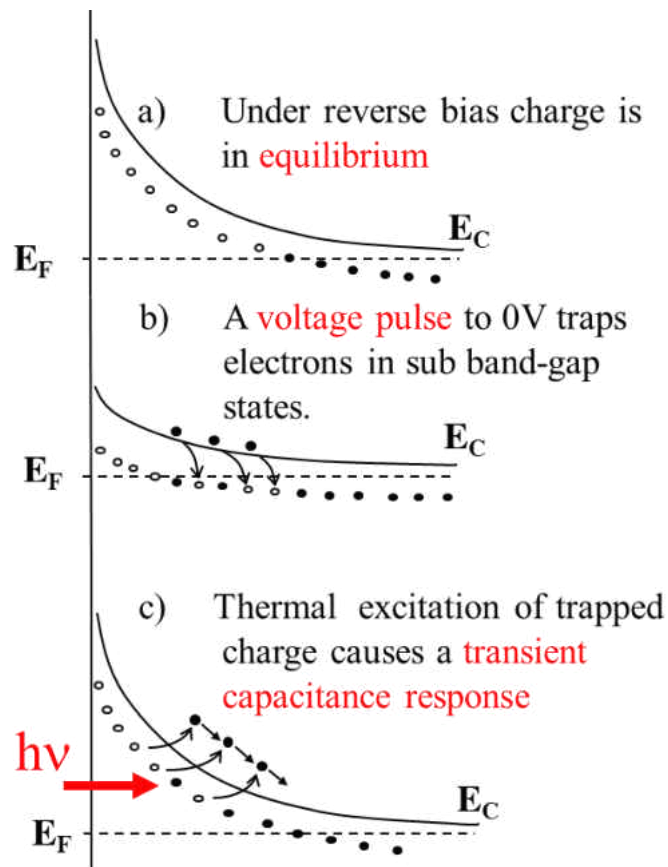


Figure 2.2. A band diagram representation of the dynamic response of a junction to a voltage pulse. (a) the original reverse-biased condition; (b) the forward biased condition; and (c) an optically assisted return of the junction to the original reverse-biased condition.

At temperature T and without illumination, the junction capacitance is monitored as a DC reverse-biased junction is momentarily ($\sim 2s$) pulsed into a slightly forward biased condition. The resulting capacitance transient response $D(t, T, \omega)$ is monitored via a

correlator function $A(t, \tau)$ ⁵:

$$S(\tau, T, \omega) = \int_{t_1}^{t_2} A(t, \tau) D(t, T, \omega) dt \quad (2.32)$$

This signal is called S_{dark} . The process is then repeated under monochromatic illumination to produce S_{light} . It is important while measuring S_{light} that the incident light flux be low enough that $S_{\text{light}} \propto \Phi(\lambda)$. This is known as the “linear response” regime. If the flux used is too high, then $S_{\text{light}} \propto \Phi(\lambda)^\gamma$ where $\gamma < 1$. Once a linear light response signal has been obtained, the Photocapacitance signal is then defined as the difference in the light and dark signals normalized to the monochromatic light flux, $\Phi(\lambda)$:

$$P_{\text{TPC}} = \frac{S_{\text{light}} - S_{\text{dark}}}{\Phi(\lambda)} \quad (2.33)$$

Since the thermal contribution to S is the same in the *light* and *dark* cases, P_{TPC} measures only the optical effect on the equilibration process. The spectra obtained in this way are very similar to what would be obtained if a true sub-bandgap absorption spectrum had been performed, but exhibit a few important differences.

In general, the optical absorption at E_{opt} is represented by

$$A = \int |(i|ex|f)|^2 g_{\text{unocc}}(E) g_{\text{occ}}(E - E_{\text{opt}}) dE \quad (2.34)$$

⁵ The correlator function $A(t, \tau)$ is an important experimental parameter that determines the maximum energy depth at which thermally emitted carriers may contribute to S , generally $E_\tau = -kT \ln\left(\frac{\tau}{\tau_0}\right)$. The parameter τ is called the ‘time window’ which for a simple ‘boxcar’ type correlator is simply of the form $\tau = t_2 - t_1$. The time window may have a more complex form depending on the functional form of $A(t, \tau)$. This functional also asserts certain signal to noise consequences [32].

Where $\langle i|ex|f \rangle$ is the optical matrix element between the occupied (*occ*) and unoccupied (*unocc*) states separated by energy difference E_{opt} . For semiconductors containing mid-gap defect states, there are two kinds of sub-bandgap absorption; these include transitions from the valence band into a gap state:

$$A_1 = \int_{E_f}^{E_V + E_{opt}} |\langle i|ex|f \rangle|^2 g_{unocc}(E) g_V(E - E_{opt}) dE \quad (2.35)$$

and from an occupied gap state into the conduction band:

$$A_2 = \int_{E_C - E_{opt}}^{E_f} |\langle i|ex|f \rangle|^2 g_{unocc}(E) g_C(E + E_{opt}) dE \quad (2.36)$$

Simplifying by letting $\langle i|ex|f \rangle$ and $g_V(E)$ (or $g_C(E)$) equal constants⁶:

$$A_1 \approx c' \int_{E_f}^{E_V + E_{opt}} g_{unocc}(E) dE \quad (2.37)$$

which implies

$$\frac{dA_i}{dE_{opt}} \propto g(E_V + E_{opt}) \quad (2.38)$$

Equation 2.38 asserts the general absorption-like *shape* of TPC and TPI spectra, but these measurement methods also provide carrier transport information of the host material. But

⁶ These assumptions are not particular to the analysis of TPC and TPI, but rather to a great many sub-bandgap optical spectroscopy methods. The assertion that the $g(E)$ are constant is reasonable based on the sheer magnitude difference between these states and mid-gap states (usually at least 10^4). The optical matrix element is assumed constant because no one can be bothered to actually measure it every time they take a spectrum. But, it turns out that this assumption is pretty good too. For more information see [33].

before the effects of carrier transport are discussed, it is important to consider the different spatial sensitivities of TPC and TPI to charge emissions from the gap. [34]

From Equation 2.4 we write the interface potential as

$$\psi_0(0) = \int_0^W x \frac{qN_d}{\epsilon} dx \quad (2.39)$$

where the total charge contained in the depletion region is given by qN_d . If we now allow

Δn electrons to escape the depletion region at position x , if $\Delta n \ll qN_d$, the interface potential becomes

$$\psi(0) = \int_0^{W+\delta W} x \frac{qN_d}{\epsilon} dx - \int_x^{x+\delta x} x \frac{\Delta n}{\epsilon} dx \quad (2.40)$$

This is easily evaluated to yield

$$\delta\psi(0) = \psi(0) - \psi_0(0) = \frac{q}{\epsilon} (W\delta W N_d - x\delta x \Delta n) \quad (2.41)$$

Since during the TPC and TPI measurements the potential across the junction is held constant throughout the measurement time window, $\delta\psi(0) = 0$. Therefore we may write:

$$\frac{\delta C}{C} = -\frac{\delta W}{W} = -\frac{x\delta x \Delta n}{N_d W^2} \quad (2.42)$$

This result asserts that the capacitance response scales linearly with x , the position at which Δn responds. Therefore TPC is most sensitive to majority carrier processes near the depletion region edge. Minority carrier processes produce the same result albeit with a shift of δW in the opposite direction with an emission of Δp from the depletion region:

$$\frac{\delta C}{C} = \frac{x\delta x\Delta p}{N_d W^2} \quad (2.43)$$

Next we consider the spatial sensitivity of the current response to charge emission from the depletion region. Once again, the charge emission will induce a change in W with some of the emitted carriers becoming absorbed into bulk conduction states in order to facilitate the change in W ⁷:

$$\delta Q = Aq(\Delta n\delta x - N_d\delta W) \quad (2.44)$$

Using Equation 2.42 this becomes

$$\delta Q = Aq\Delta n\delta x\left(1 - \frac{x}{W}\right) \quad (2.45)$$

Equation 2.45 asserts the opposite sensitivity to majority carrier charge emission from the depletion region than in the capacitance case: a linear *decrease* at increasing distances from the junction interface. However this opposite sensitivity is only true for majority carrier emission from the depletion region, which produces $\delta W < 0$ thereby requires charge absorption into the bulk. For minority carriers:

$$\delta Q = Aq\Delta p\delta x\left(\frac{x}{W}\right) \quad (2.46)$$

which yields the same spatial sensitivity to charge emission as in the capacitance case.

We have seen that TPC is most sensitive to charge emission processes far away from the junction interface; on the other hand, TPI is sensitive to majority carrier processes

⁷ For example, if W becomes smaller as majority carrier charge is emitted from the depletion region, the neutral bulk region will grow by δW . In order to maintain charge neutrality, some of the emitted charge will necessarily occupy bulk conduction states.

near the junction but most sensitive to minority carrier processes far from the junction. These spatial sensitivity issues aside, TPC and TPI measurements also have opposing sensitivities to minority carrier collection. This phenomenon, and a useful way to exploit it, is discussed in the next section.

Determination of the Minority Carrier Collection Fraction

For n-type materials, changes in capacitance can be written in terms of charge type emitted from the depletion region: $\delta C = \Delta n - \Delta p$; likewise total charge: $\delta Q = \Delta n + \Delta p$. This simple observation allows us to write TPC and TPI signal levels in terms of the *number* of carriers collected over the course of the measurement time window:

$$P_{TPC} = K_{cap}(n - p); P_{TPI} = K_{cur}(n + p); \quad (2.47)$$

Where the scale factor K depends on carrier mobilities, the optical matrix element, the spatial sensitivities of the respective measurement methods, the biases applied during the measurement, and many other factors. [35] However, if the TPC and TPI measurement are taken under identical experimental conditions, we add only the additional assumption that any effect of the individual spatial sensitivities of these measurements can be ignored to conclude [35,36]: $K_{cap} \approx K_{cur}$. Under these assumptions it is straightforward to show that

the fraction of all carriers collected which are holes can be expressed as

$$f_p = f_n \frac{1 - R}{1 + R} \quad (2.48)$$

Where R is the ratio of the TPC signal to the TPI signal, $R = P_{TPC}/P_{TPI}$ and $f_p = p/(n+p)$;

$f_n = n/(n+p)$. We generally assume that due to the high mobility of electrons and the long timescale of the TPI and TPC measurements that $f_n \sim 1$. If these assumptions hold, then it is possible to estimate f_p by taking ratios, R, of TPC and TPI spectra at a given excitation wavelength.

Raman Spectroscopy

Raman Spectroscopy is a well-known method for probing the molecular contents of a material by analyzing the inelastic scattering of photons off of the material. This inelastic scattering is known as the *Raman Effect* and is the result of quantum mechanical coupling between photons and phonons. In essence, Raman Spectroscopy gives the experimentalist information about the phonon dispersion spectrum of a material, therefore information regarding the material's contents. To briefly motivate the physical basis of the Raman measurement [37], one needs only to consider the atomic polarizability, α (i.e. how easily the atomic charge distribution can shift to absorb a photon) as a function of an atomic strain parameter, u .

$$\alpha = \alpha_1 u + \alpha_2 u^2 + \dots \quad (2.49)$$

Now let the strain parameter oscillate at frequency ω_s so that

$$u = u(t) = u_o \cos(\omega_s t) \quad (2.50)$$

The induced dipole moment in the atomic charge distribution, $p = \alpha E$, in the presence of a photon of frequency ω described by $E(t) = E_o \cos(\omega t)$ is then given by:

$$p = u(t) = \alpha_1 u_o E_o \cos(\omega t) \cos(\omega_s t) + \dots \quad (2.51)$$

Using the trigonometric identity $\cos(a)\cos(b)=1/2[\cos(a-b)+\cos(a+b)]$:

$$p = u(t) = \frac{1}{2} \alpha_1 u_o E_o \{ \cos[(\omega + \omega_s)t] + \cos[(\omega - \omega_s)t] \} + \dots \quad (2.52)$$

Therefore, the allowed inducible dipole moments (to first order) in such a scenario occur at two frequencies: $\omega + \omega_s$ and $\omega - \omega_s$. Since the ω_s represent vibration modes in the lattice this result indicates phonon-mediated optical absorption and likewise, emission. The inelastically scattered photons of *higher* final energy (those at frequency $\omega + \omega_s$) are called “anti-Stokes” scattered photons, and those of lower energy are said to be “Stokes” scattered.

Since the ω is known, the particular dispersion of the ω_s is used to gain knowledge of the host material’s structure. In this study, we have used this information to measure the crystalline volume fraction of nc-Si:H films.

Raman Measurements and Data Analysis

The Raman measurements used in this study were performed using a Renishaw RM series confocal microscope using both 488nm and 785nm excitation lasers. In addition, the control and analysis software for the RM series instrument is a very powerful tool for organizing data and for performing the gaussian deconvolutions that are required to determine crystalline volume fractions; this deconvolution process is discussed below.

Raman scattering measurements are performed very easily and quickly using the RM series equipment. Figure 2.3 shows a typical set of output data. There are, however, several important guidelines that are necessary to follow in order to obtain the best quality

data. The largest concern when working with materials containing amorphous content is not to melt the sample using the excitation laser. In most cases, a small amount of laser-induced melting will force the material to crystallize.

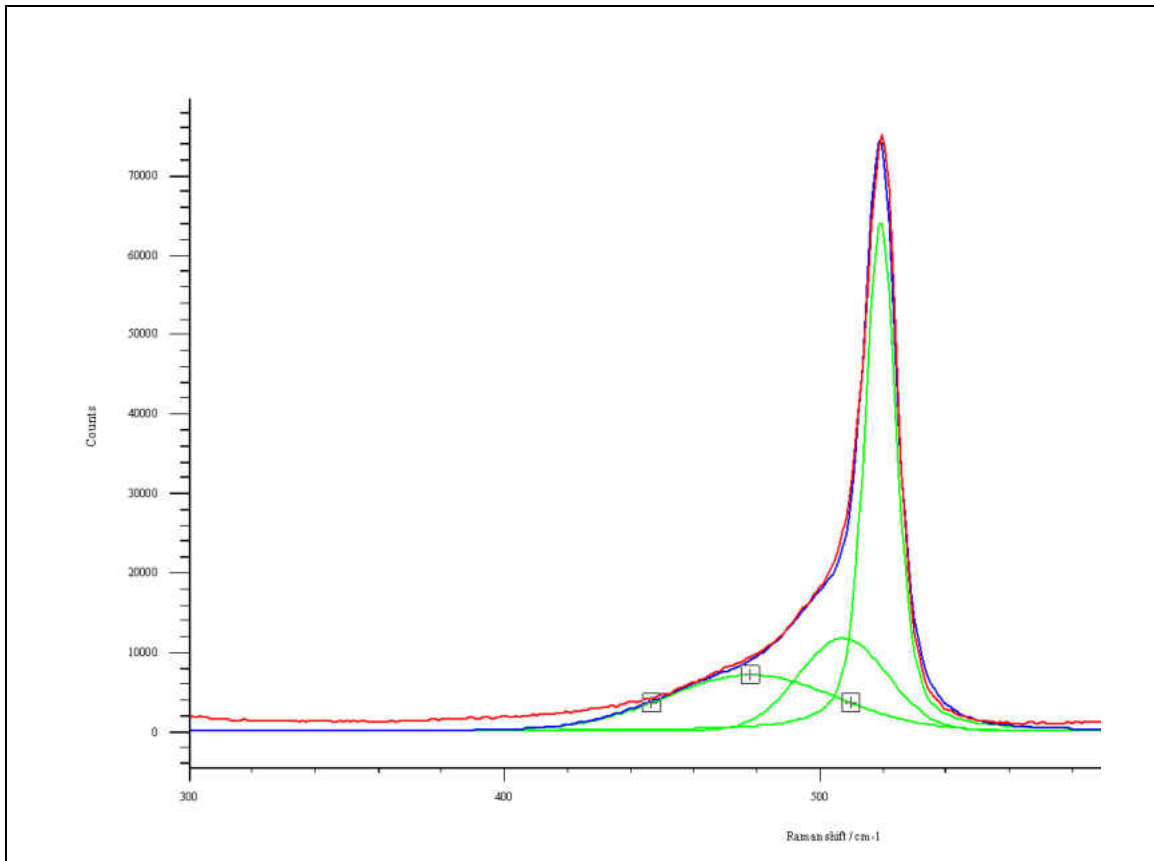


Figure 2.3. Sample output Raman data from the Renishaw RM series confocal microscope. The excitation laser during this measurement was 785nm.

For the measurements performed in this study, the 785nm excitation laser was attenuated to 0.05% and the 488nm laser was kept below 5% to prevent inadvertent crystallization of the nc-Si:H material. [38] Secondly, excitation laser wavelength should be carefully chosen so that one is sure that he is probing material properties in the region of material he wishes. For example, in this study the 488nm laser only has a penetration depth

of roughly 0.2 μm , meaning that data from this laser only provides information about the test material in this 0.2 μm region. Lastly, the RM series equipment allows one to very easily adjust the spot size of the excitation laser. Spot size is important since it defines the test area, therefore it is desirable to have a spot size large enough to provide a good spatial average of material properties. This is especially important when dealing with materials that may contain structures that are elongated along the growth direction, but may be well-spaced in spatial dimensions perpendicular to the growth direction, or in situation where crystallite structures amalgamate into clusters. In such cases, which is entirely possible for nc-Si:H, a too-small excitation laser spot size could easily produce skewed measurement results based solely on its randomized orientation on the material surface.

Figure 2.3 shows data taken using the Renishaw RM series instrument. The data is presented in the native format for the Renishaw system's analysis software. The red curve is the raw data, the green peaks are deconvolved component peaks and the blue curve is the sum of the component peaks. The analysis software makes it very easy to perform this deconvolution process and the results are obviously favorable.

The particular Raman analysis to determine crystallinity in this study followed the procedure of Bustarret *et. al.* and Han *et. al.* [39,40] although alternative analysis methods have recently been suggested. In the method used by Bustarret and Han, however, one simply calculates the crystalline volume fraction using the integrated peak areas of the deconvolved component peaks, like so:

$$X_c = \frac{I_{520} + I_{515}}{I_{520} + I_{510} + \gamma(L)I_{480}} \quad (2.53)$$

Here, I_x is the integrated peak area for the peak centered roughly at a Raman shift of x nm.

The $y(L)$ is a factor with magnitude on the order of 1 that corrects for the different absorptive properties of the crystalline and amorphous components when the crystalline inclusions are of nominal dimension L . [39] The factor is calculated by considering derivatives of the real and imaginary parts of the dielectric function. We calculated this factor to have a value of 0.95 for nc-Si:H, but we quickly decided to simply set $y(L)=1$ for the sake of consistency. With $y(L)=1$, note that the Renishaw analysis software very conveniently outputs the relevant numbers needed for the calculation of the crystalline volume fraction.

CHAPTER III

STRUCTURAL AND COMPOSITIONAL PROPERTIES OF NC-SI:H

3.1. Film Growth and Structure

Plasma-enhanced chemical vapor deposition (PECVD) is one method for depositing optically thin films, such as solar cells. The method works by ionizing a set of precursor gases between two parallel plate electrodes which carry a radio frequency (RF) or “very high” frequency (VHF) ionizing voltage. The gas is then allowed to condense on a substrate and thus the film is deposited.

In the case of nc-Si:H, and for the materials investigated in this study, the precursor gases are a mixture of silane (SiH_4) or disilane (Si_2H_6) and diatomic hydrogen; the growth method is a “modified” VHF technique, the details of which are property of United Solar Ovonic, LLC. The fractional hydrogen content of this gas is known as the hydrogen dilution ratio. The hydrogen dilution of the gas greatly affects the structural and electronic properties of the resulting film, as is summarized in Figure 3.1.

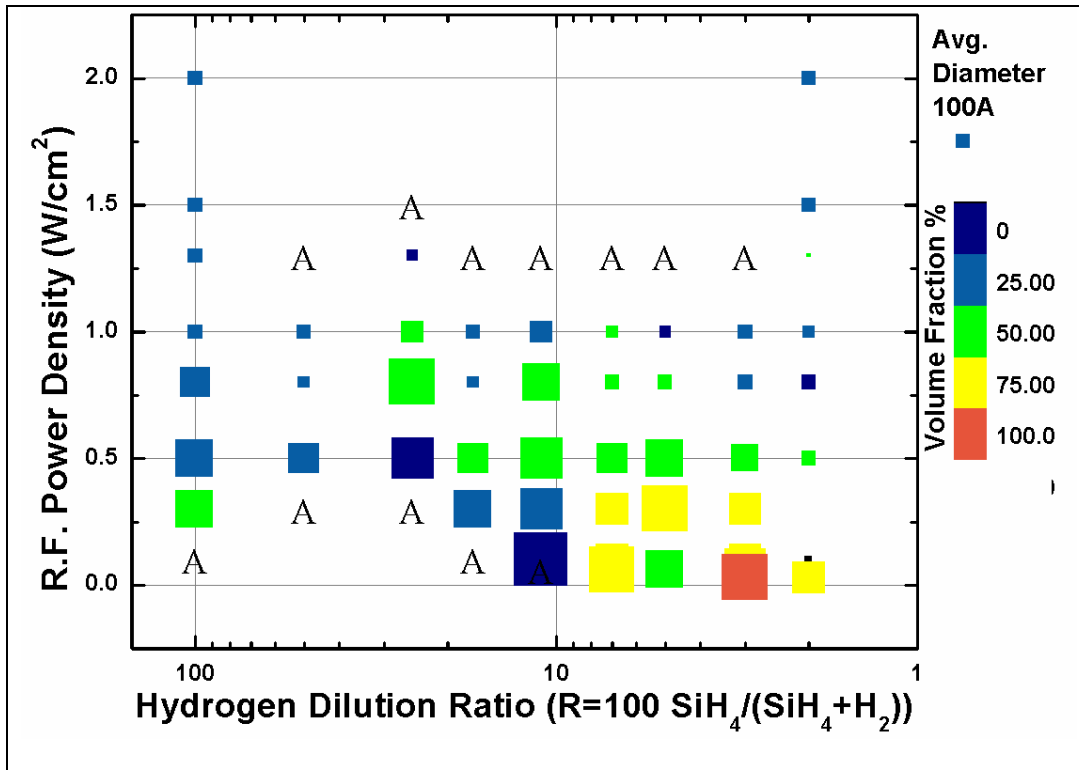


Figure 3.1. The total crystalline volume fraction and crystallite size distribution for RF PECVD deposited silicon films as a function of RF power density and hydrogen dilution. The “A’s” refer to pure a-Si:H growth. (adapted from [41])

In general, the film deposition process does not result in a homogenous material.

Instead, small local nucleations and subsequent growth patterns can cause large-scale inhomogeneities such as columnar or cone-shaped growth of crystallites, voids, grain-boundary collisions, and surface roughness. Some of these structures are visible in Figure 3.2. Careful control of the hydrogen dilution ratio and special care to produce a well-ionized and homogenous plasma can help to mitigate the effects of such structures and indeed, to control their growth. This is mainly because the hydrogen dilution ratio is one of the primary factors affecting film crystallinity.

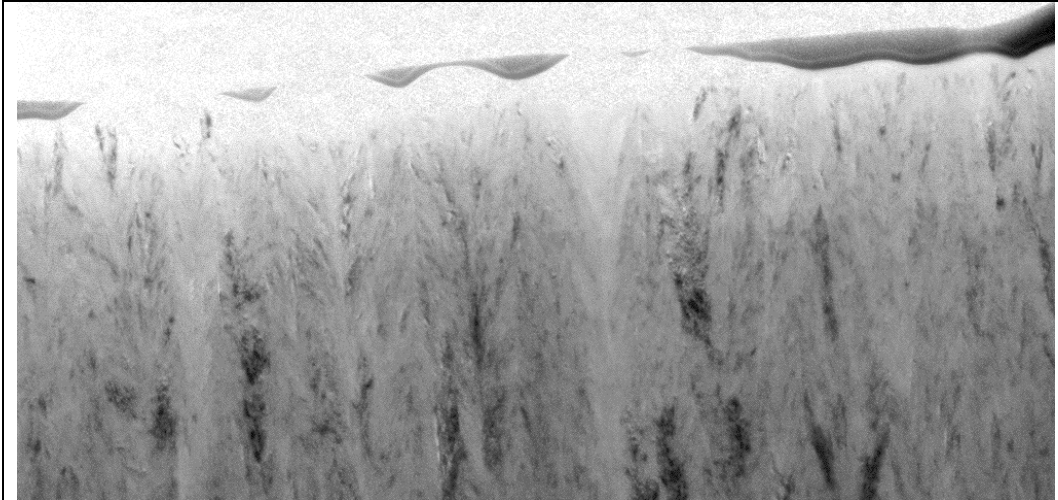


Figure 3.2. This TEM cross section image of highly crystalline (~70vol%) nc-Si:H shows columnar and cone-like nanocrystalline structures near the material surface. The growth direction was from the bottom of the image to the top. Similar dome-like surface protrusions were studied in [42] to quantify the relative growth rates of a-Si:H and the nanocrystallites. Differences in contrast denote the presence of differently oriented crystallite structures.

There have been many studies on the effect of hydrogen dilution in silicon films (for example [43-46]) but one particularly enlightening study was on the formation of crystalline cones in two-phase silicon materials. [42] In this study, crystalline cone structures were measured in materials with a given hydrogen dilution. The characteristic cone angles were then related to the relative growth rates for a-Si:H and c-Si in the film. The study supports two-phase silicon growth models such as that of Tsai [47], which suggests that hydrogen present in the precursor silane mixture preferentially “etches” the a-Si:H phase. This means that careful tweaking of the hydrogen dilution throughout the deposition process is a powerful way to control the formation of crystallites; increasing the dilution to promote crystallite growth, and ramping the dilution ratio down to choke off the

formation of crystallite cones or columns and therefore maintain a relatively homogenous a-Si:H/nc-Si:H film mixture. A characterization of growth cones for the material shown in Figure 3.2 is given below in Figure 3.3.

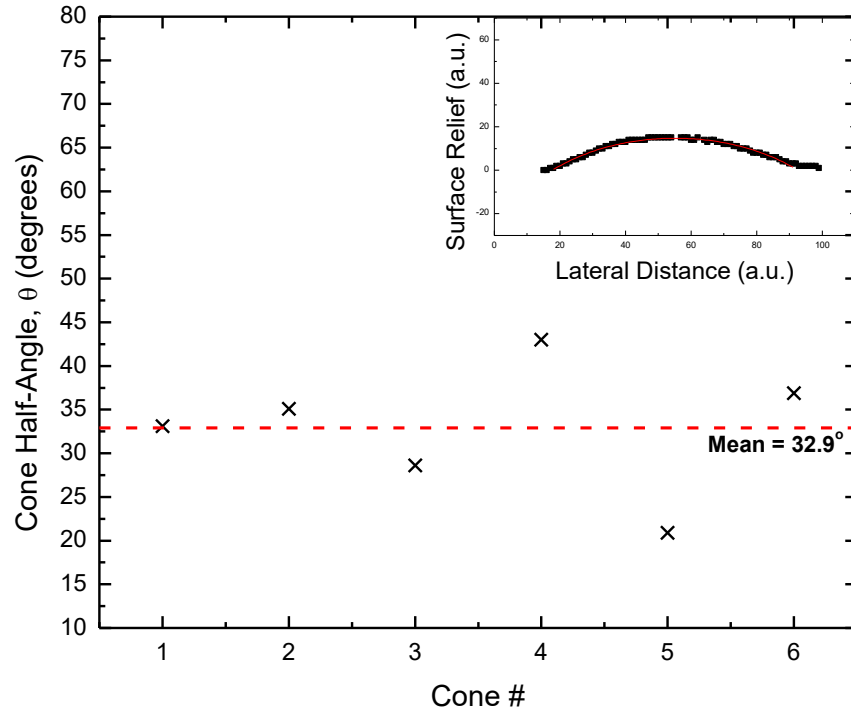


Figure 3.3. The cone-angle experiment presented in [42], which yielded a mean cone half angle of $\Theta=40^\circ$, was repeated on one highly crystalline sample (sample 16115) included in this study, yielding $\Theta=32.9^\circ$. Cone angles were found by extrapolating cone angles from best fits to spherical protrusions from the material surface.

Naturally, the deposition of quality nc-Si:H films goes beyond only controlling the hydrogen dilution ratio. Factors such as substrate temperature, the ionizing voltage amplitude and frequency, the precursor gas pressure, growth rates, etc. are also important, not to mention the presence of impurities (which is discussed below). The hydrogen dilution is however the most concrete influence on nanostructure, and nanostructure is an

important consideration when characterizing the performance of these materials. Such structure is the topic of the next section.

3.2. Nanostructure

Depending on the deposition parameters used one may achieve a mixed phase silicon material that is polycrystalline, having negligible amorphous content and consisting of many randomly oriented component crystals, or fully amorphous. As was discussed in the previous section, sweeping through this wide range of crystallinity is most readily achieved by altering the hydrogen dilution in the growth plasma. Figure 3.4 shows schematically the types of structures and the distribution of crystallites that might be produced as one deposits two-phase silicon at various hydrogen dilution ratios.

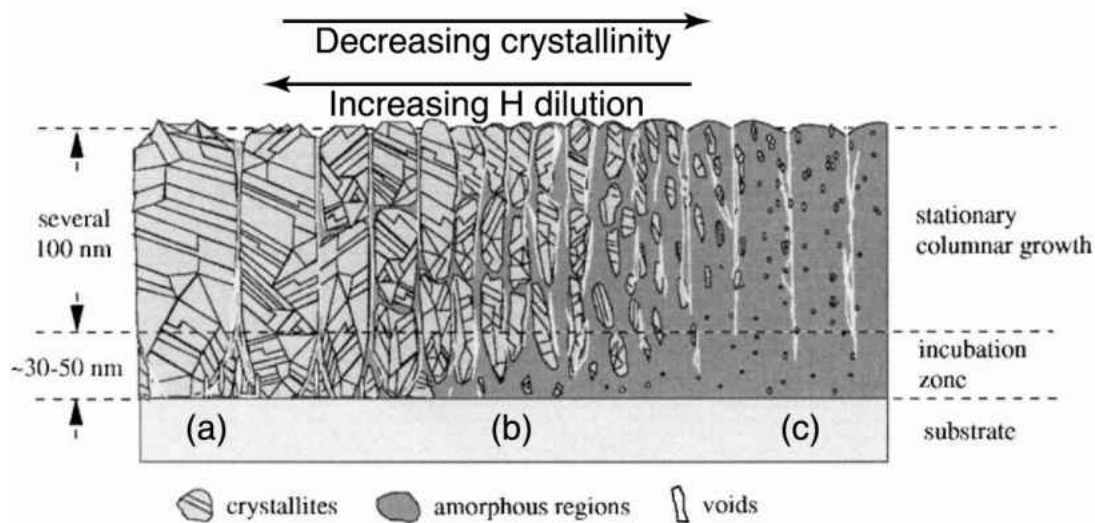


Figure 3.4. A schematic adapted from [51] showing an idealized progression from polycrystalline silicon (a) to nearly pure amorphous silicon (c). The best nc-Si:H devices are always prepared in the “well-mixed” growth region near (b), where both phases exist in nearly equal volumes. These structural changes are most readily accomplished by varying the hydrogen-to-silane concentration ratio.

It is important for one to know at what point along the growth continuum shown in Figure 3.4 he is growing mixed-phase silicon since the best contemporary materials tend to be prepared in the “well-mixed” regime. [48-50]

In order to study the effects of crystallinity on solar cell electronic properties and to study the effects of the substrate on resulting crystallite growth, we studied a series of samples each grown with a particular preparation “recipe” but for which crystallinity was allowed to vary across the face of the substrate, as shown in Figure 3.5.

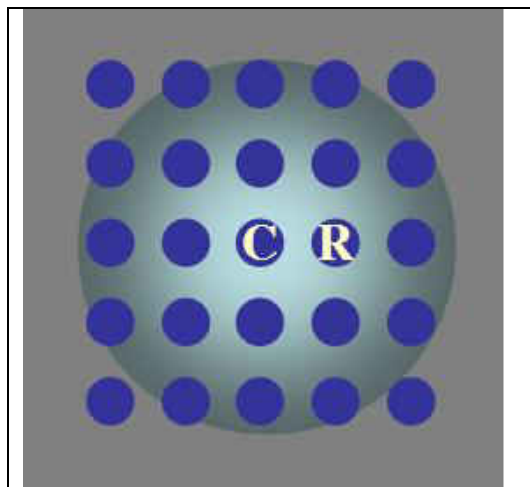


Figure 3.5. A schematic view of a typical sample array. Blue dots represent individual contacts. Contacts located centrally (C) are more crystalline than those located radially (R). Beyond a certain distance (indicated by the large circle) from the substrate center, samples were nearly fully amorphous.

For such samples, variation in crystallite content was a result of the inhomogeneous application of power density throughout the growth plasma. This allowed us to measure effects of crystallinity changes without also contending with simultaneously varying precursor gas compositions. Raman spectra for two of these materials are given in Figure 3.6.

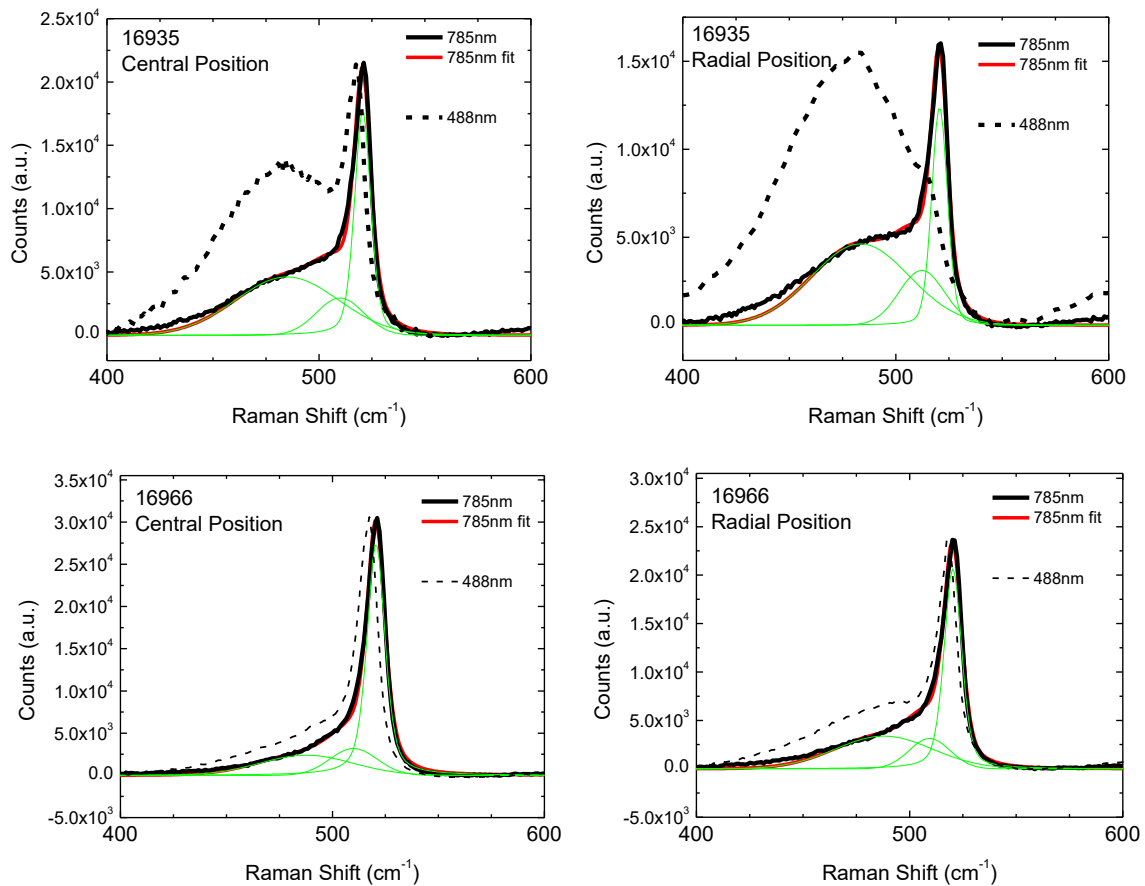


Figure 3.6. Sample Raman spectra with deconvolved component peaks from samples whose crystallinity was allowed to vary across the substrate (see Figure 3.4). Samples located centrally were more crystalline than those located radially. By using a strongly absorbed excitation wavelength (488nm) it was also seen that some samples showed an amorphous character near the p/i interface.

The spectra from Figure 3.6 show Raman results for two excitation wavelengths: 785nm, for which the raw data, best fit, and deconvolved best-fit peaks are given (see Section 2.6 on Raman Spectroscopy); and 488nm, for which the raw data is given. These excitation wavelengths were chosen so that the longer wavelength laser would penetrate the entirety of the films' intrinsic layers ($\sim 1\mu\text{m}$) while the shorter wavelength laser would be absorbed within the top $\sim 0.1\mu\text{m}$ of the intrinsic layer. These measurements indicate the extent to which structural properties of a single-deposition film can vary. These Raman spectra were performed on a common central (C) and radial (R) location for each member of the sample set (see Table 3.1).

Sample	Position	Crystalline Fraction, X_c	
		785nm	488nm
16922 Ag/ZnO	Central	0.63	0.39
	Radial	0.59	0.34
16935 SS	C	0.5	0.22
	R	0.44	0.04
16966 3 μ nip	C	0.91	0.65
	R	0.63	0.49
16988 3 μ sand.	C	0.75	0.06
	R	0.69	0.06

Table 3.1. Raman crystalline fraction summary for two samples grown using the same recipe but deposited on different substrates, 16922 on textured Ag/ZnO and 16935 on specular stainless steel (SS). Samples 16966 and 16988 were deposited nearly three times thicker than the other two samples and were identical except for their final geometry, a typical n-i-p geometry in the case of 16966 and an a-Si:H sandwich geometry for 16988.

The more radial samples were consistently more amorphous, but the extent of the change was strongly affected by the deposition parameters and the nature of the substrate.

Dependency of film structure on the substrate can be understood as follows. N and subsequent growth of crystallites means that films tend to become more crystalline throughout the growth process (see Section 3.1). For a film deposited on a rough substrate such as Ag/ZnO this means that crystallite growth cones are oriented in such a way that during growth the cones collide, resulting in a film of higher crystallinity and with a greater density of grain boundaries. [52,53] The data shown in Table 3.1 is consistent with this interpretation since the sample deposited on a textured substrate (16922) shows a greater density of crystallites than the material deposited on a specular substrate (16935) near the top surface.

Materials that were grown 3 μ m thick (samples 16966 and 16988), three times thicker than the other sample pair, were also seen to have higher average crystallinities than the thinner samples. Again, this is a result of crystallite seeding and growth during deposition. Note, however, that the a-Si:H/nc-Si:H/a-Si:H sandwich structure of sample 16988 has resulted in a small crystallite fraction for 488 nm laser illumination. This is a property of the a-Si:H buffer layer and not a property of the intrinsic layer.

These results are typical of the nc-Si:H films examined during this study and are provided to give a sense of the range of structural behaviors evident in nc-Si:H. During the deposition of high quality nc-Si:H material, however, the evolution of film properties throughout growth needs to be constrained as much as possible. As was mentioned in the section on growth kinetics, manipulation of the H dilution is one of the best ways to accomplish this -- for example, slowly ramping down the H dilution throughout the film

deposition. The effect of this ramping will be to control film crystallinity, but will also change the atomic composition of the film. The compositional effects of hydrogen dilution, and the presence of oxygen in these materials are the subjects of the next section.

3.3. Compositional Variations

One of the best ways to determine the composition of a film as a function of film depth is the well-known secondary ion mass spectroscopy (SIMS) method. Sample SIMS data is shown in Figure 3.7.

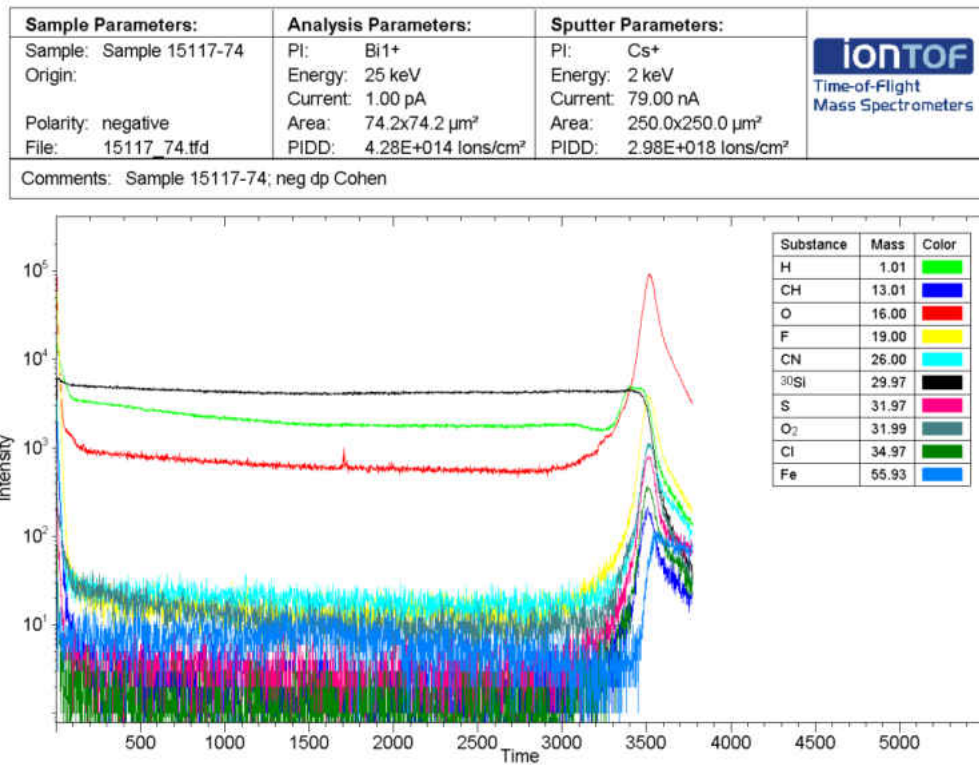


Figure 3.7. Typical SIMS spectrum of a nc-Si:H intrinsic layer. The increased counts near sputter time of 3500s indicates the presence of the substrate. A sputter time of 0s indicates the ‘top’ or light-incident side of the sample.

The SIMS technique destructively etches the film with an ion beam and examines the masses of the ejected material to determine the composition of the film as a function of the total etch time – i.e. depth. The sample spectrum in Figure 3.7 shows counts of molecular species vs. etch time. In this particular film, the most readily counted molecular species are ^{30}Si , monatomic H, and O. Trace counts of species such as CH, S, and F were detected throughout the layer. The sharp increase in species counts near a sputter time of 3500 s indicates a transition from sputtering the nc-Si:H intrinsic layer to sputtering the substrate layers. It is important to keep in mind that the scattering cross section for each atomic species is different, so the SIMS technique is not strictly quantitative. Relative concentrations of atomic species can be found by taking ratios of species to a suitable background level, such as ^{30}Si in these films. Figure 3.8 clearly shows how the SIMS method can show the compositional effects of H dilution.

Figure 3.8 compares two films, one of which (sample 18349) was grown with constant H dilution and the other (sample 19183) was grown using a functionally reduced H dilution throughout the deposition. Correspondingly, the H content of the constant dilution film is very flat throughout the nc-Si:H intrinsic layer. However the H content of the graded film shows a sharp *increase* near the top surface, that is, it shows an increase in hydrogen content as the hydrogen dilution was *decreased*. This is because decreased hydrogen dilutions encourage the growth of the amorphous phase (see Figure 3.1). The amorphous phase, in turn, typically supports concentrations of hydrogen atoms in the 10-15at.% range whereas crystalline silicon contains roughly 5at.% hydrogen, or less. [54,55]

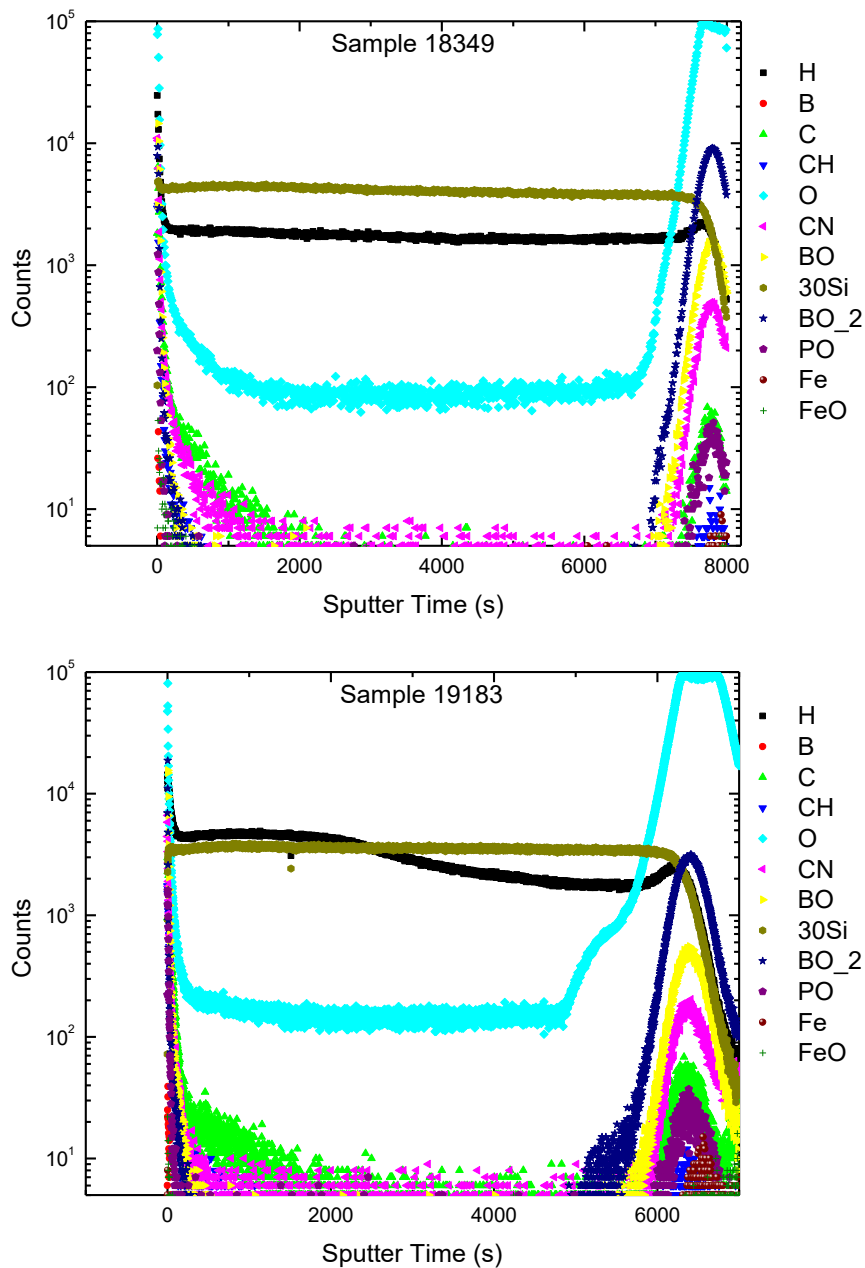


Figure 3.8. Hydrogen profiling effects are clearly seen using SIMS profiling. (top) a film grown using constant H dilution (bottom) a film grown as the H dilution was ramped down throughout the deposition.

This conclusion is supported by correlations between the type of hydrogen dilution profiling used and the open circuit voltage for the films studied. Since the electron affinity

of hydrogenated amorphous silicon (a-Si:H) is smaller than crystalline silicon, larger open circuit voltages should be observed for films with greater a-Si:H content near the top surface. This was indeed the result seen for an ensemble of films deposited using hydrogen dilutions that were functionally altered in time throughout the growth process (see Figure 3.9).

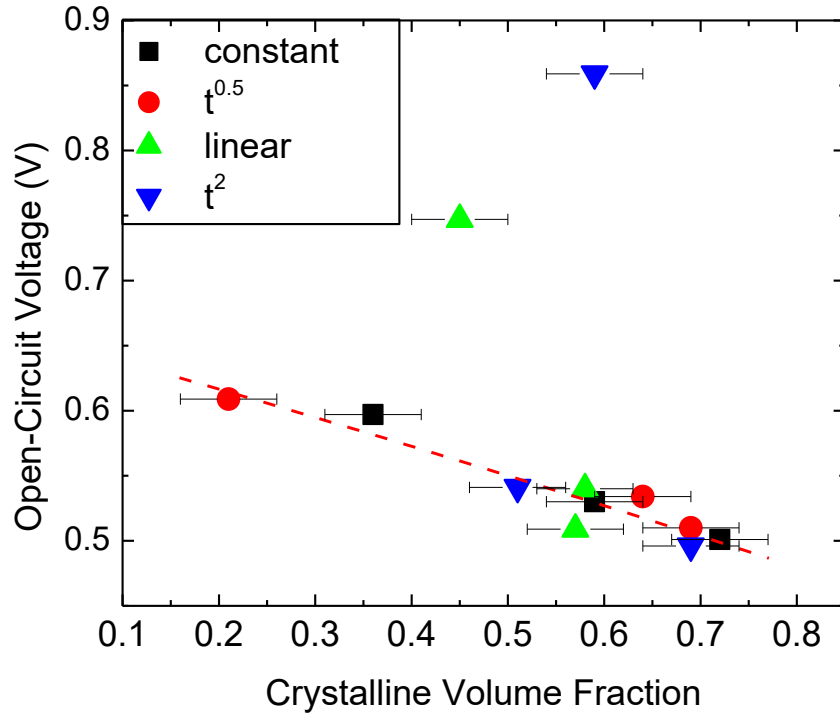


Figure 3.9. Hydrogen dilution profiling effects on the open circuit voltage (V_{OC}). As expected, the average crystallinity yielded by Raman spectroscopy correlated well with V_{OC} , but those films with more amorphous content near the junction contact showed very high open circuit voltages.

Hydrogen dilutions were either held constant, ramped as \sqrt{t} , t , or t^2 , where t was the deposition time. In each case, the total hydrogen content of the films was held constant, with only the spatial distribution of hydrogen in the completed films changing. Indeed,

more amorphous films exhibited larger values for V_{OC} , with the largest V_{OC} values given by those films with the most rapidly varied H dilutions (dilutions ramped as functions of t and t^2), indicating a high concentration of amorphous content near the top surface of these films.

However, simply having larger open-circuit voltages does not particularly make better solar cells, as can be seen from Table 3.2. Nor does the distribution of crystallinity alone determine all of a nc-Si:H cell's electronic properties. Impurity dopants may also play a large part in determining a film's electronic properties. In the next section, we will consider the presence of atomic dopants on the properties of these materials, in particular, the presence of oxygen.

Run	H ₂ Profiling	Cell	J _{sc}	V _{oc}	FF	Xc
15125	constant	94	11.86	0.597	0.496	0.36
15125	constant	75	15.57	0.53	0.522	0.59
15125	constant	74	14.89	0.501	0.529	0.72
15123	$t^{1/2}$	94	15.67	0.609	0.499	0.21
15123	$t^{1/2}$	75	16.12	0.534	0.575	0.64
15123	$t^{1/2}$	74	16.62	0.51	0.589	0.69
15117	linear	94	14.46	0.747	0.406	0.45
15117	linear	75	16	0.54	0.572	0.58
15117	linear	74	16.53	0.509	0.59	0.57
15121	t^2	94	11.57	0.859	0.399	0.59
15121	t^2	75	15.38	0.541	0.444	0.51
15121	t^2	74	15.68	0.496	0.521	0.69

Table 3.2. Crystallinity and cell performance parameters for the devices featured in Figure 3.8. Crystalline fractions, $X_c \pm 0.05$, were estimated using Raman spectroscopy.

The Presence of Oxygen

Aside from trace amounts of atomic species such as C, N, and B, only one accidental dopant was found in these materials in significant quantities – oxygen, shown in Figure 3.10. Oxygen has been known to affect the electronic properties of silicon thin films for some time [56-60] but its particular role in nanocrystalline silicon is yet to be solidly determined.

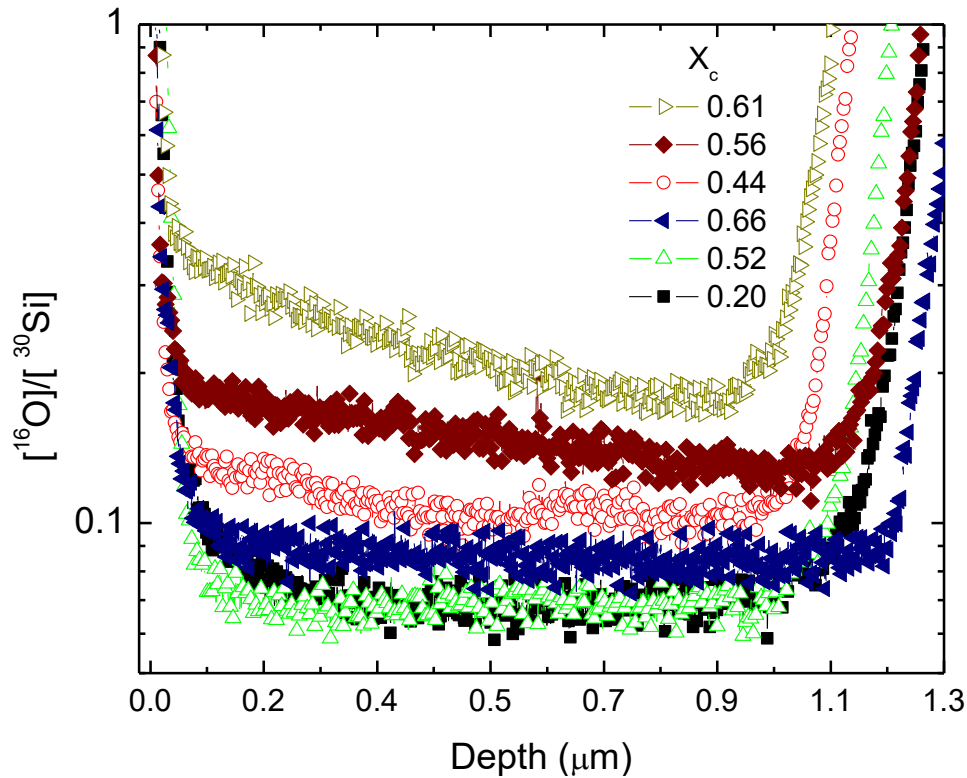


Figure 3.10. Many nc-Si:H measured in this study showed significant concentrations of oxygen. A rough correlation of oxygen content to crystallinity was observed.

Oxygen is often present in significant amounts in nc-Si:H and can be incorporated into the films one of two ways: either by thermal oxidation during film deposition, or by post deposition gaseous uptake. Both scenarios would result in oxygen distributions that are

maximum at the sample surface and decrease exponentially as a function of depth through the film. The oxygen distributions in these films were estimated by taking SIMS count ratios of ^{16}O to ^{30}Si . Using this method, a rough correlation with oxygen content and crystallinity was observed as is shown in Figure 3.10. Note that the concentrations from Figure 3.10 are uncalibrated and are not absolute.

Figure 3.11 illustrates an effort to correlate the presence of oxygen with the presence of grain boundary structures.

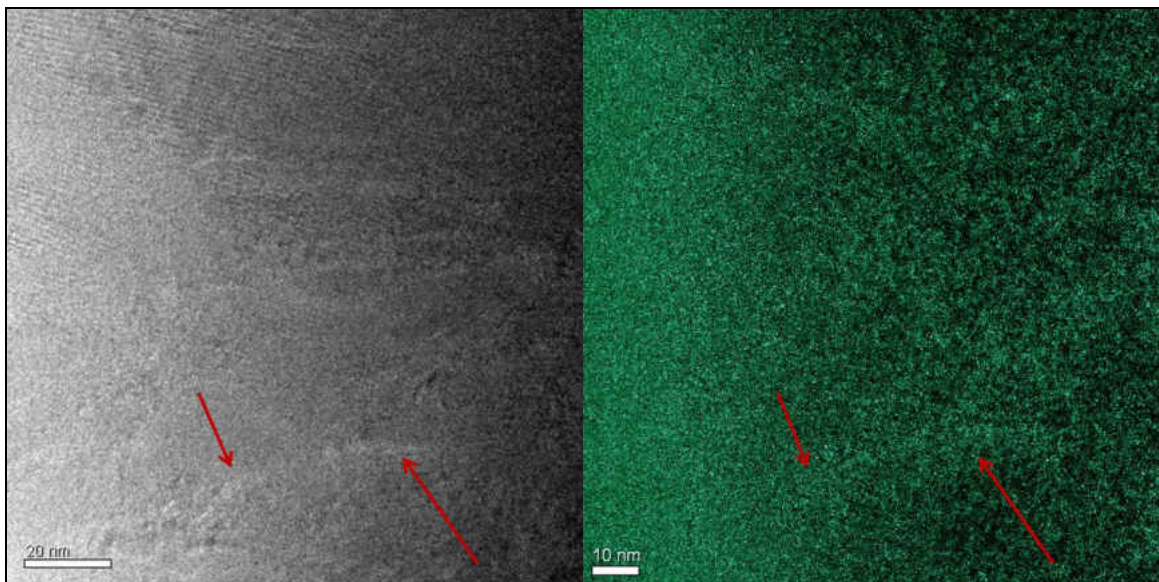


Figure 3.11. Zero loss EELS (left) and oxygen map EELS (right). Slightly higher concentrations of oxygen (right) seem to occur at the same location of the grain boundary type structures (left).

For mixed phase materials, it is often the case that contaminants such as oxygen are naturally rejected into grain boundary regions, or otherwise substantial regions of amorphous tissue. [61-63] As will be discussed further in Section 4.2, oxygen levels in these materials is substantial, but relatively low – within a factor of 2 from the 1at% level

(roughly 10^{19} atoms/cm³). Such low concentrations are difficult to image directly, but we did make one attempt at imaging these oxygen levels using electron energy loss spectroscopy (EELS). The data, which are somewhat inconclusive, are shown in Figure 3.11. On the left of the figure is the zero loss EELS image, where the signal indicates the presence of all atomic species in the material. The top of the sample is on the left. In this image a large amount of signal is seen in the largely amorphous region directly beside the sample surface and a moderate amount of grain boundary structure is seen deeper into the sample (see arrow). When this image is compared to an EELS image of oxygen content (shown right) similarities can be spotted between the crystallite structure and densities of oxygen. This is perhaps weak direct evidence of oxygen accumulating at grain boundaries. However, the sample from which these EELS data were taken was 100 nm thick, meaning that many layers of crystallites of dimension 20 nm contributed to the signals in Figure 3.11, most likely increasing background signal levels. The effects of this layering are discussed in Figure 3.12. It is possible that the same measurement repeated for a thinner sample could yield clearer results.

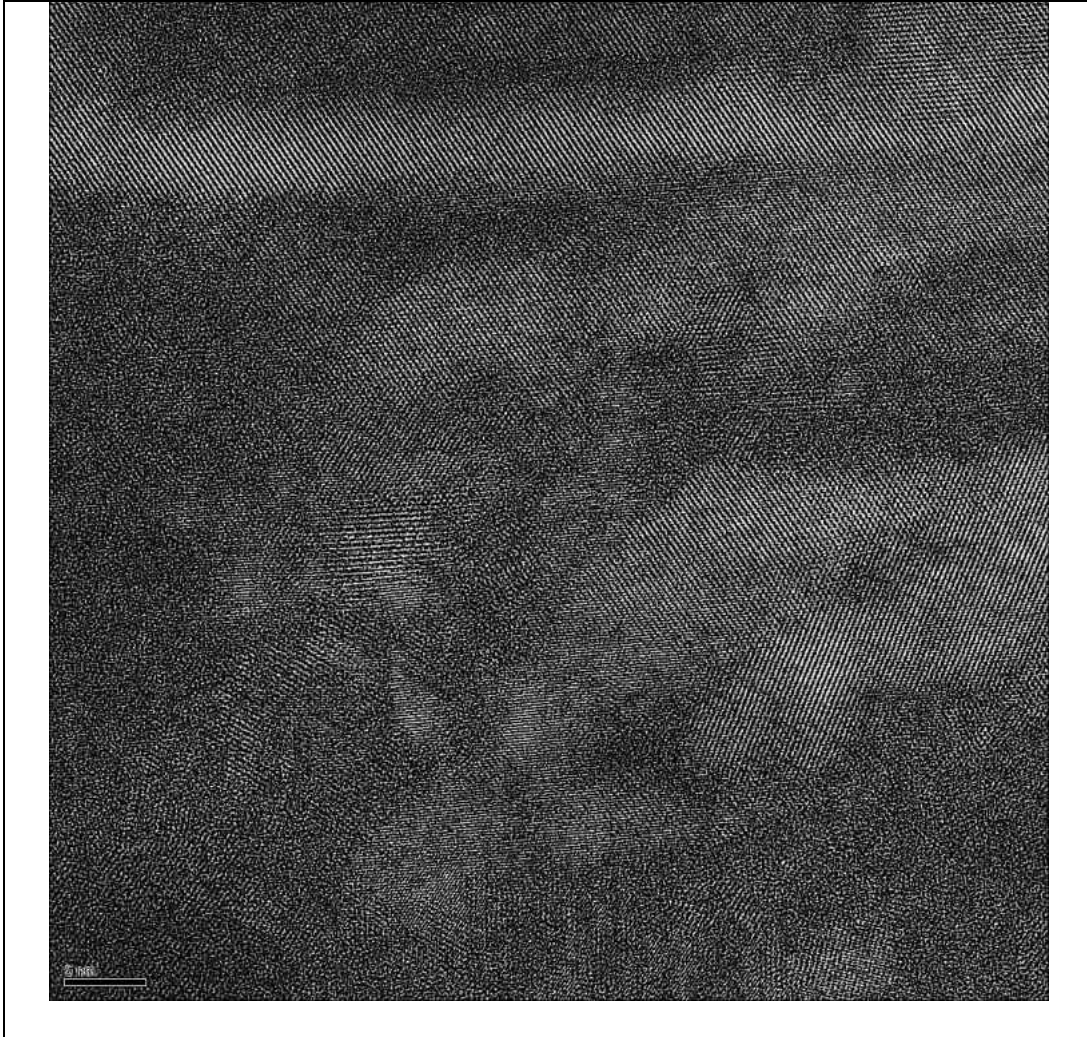


Figure 3.12. This high-resolution TEM image clearly indicates the presence of crystallites and grain boundaries in nc-Si:H. This particular sample, 14036, had a crystallite volume fraction of $X_c=0.61$. Growth direction in this image was from right to left. The region of disordered material on the left hand side of the image is most likely an effect of the ion-milling beam used for sample preparation. Note that in addition to clear regions of crystallite intersection, also visible are column-like crystal structures and overlaid crystal structures. The latter is an indicator that the sample thickness ($\sim 100\text{nm}$) was larger than the crystallite sizes ($\sim 20\text{nm}$).

One other attempt to determine the location of oxygen in these materials was to compare SIMS data with Raman data. Recall that the deconvolved Raman peaks, at

520 cm^{-1} , $\sim 480 \text{ cm}^{-1}$, and $\sim 515 \text{ cm}^{-1}$ indicate the presence of well-ordered, disordered, and quasi-ordered silicon phases, respectively. The latter peak has been taken by several authors to indicate the presence of grain boundaries. Figure 3.13 shows the integrated intensity fraction of each component peak plotted against the [O]/[H] concentration for these materials. The reasons for choosing this particular concentration ratio is discussed in Section 4.2.

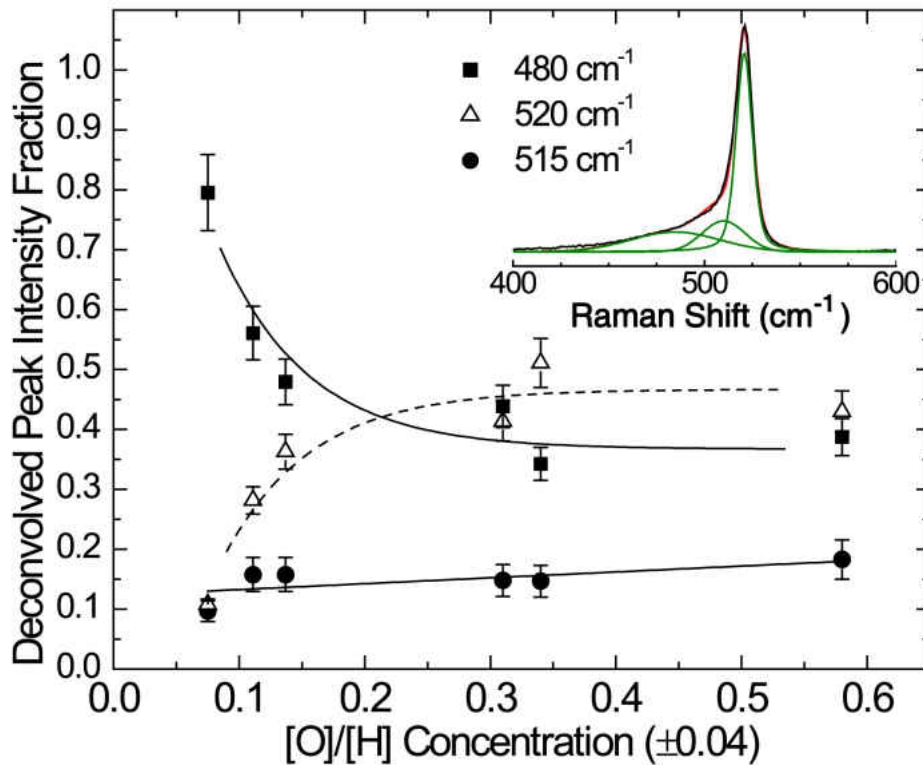


Figure 3.13. Oxygen per Hydrogen concentrations plotted against deconvolved Raman peak intensities. The linear increase ($R^2=0.3$) of [O]/[H] with the 515cm^{-1} could suggest that oxygen accumulates in grain boundary regions.

In Figure 3.13, the [O]/[H] concentration exhibits an exponential or power law relation to the presence of both the crystalline and amorphous phases. In contrast, the

intensity of the 515 cm^{-1} Raman peak shows a weak but statistically significant ($R^2 = 0.3$) linear increase with $[\text{O}]/[\text{H}]$ content. This might suggest oxygen resides along grain boundaries, voids, or other regions of quasi-ordered phase. While this idea is appealing, the data supporting this remain somewhat inconclusive.

Given these results, we conclude that many of our samples do contain significant ($\sim 1\text{at}\%$) of atomic oxygen. Results from the literature, our physical intuition, and relatively inconclusive EELS and Raman data suggest to us that many of these oxygen reside in grain boundaries or within the amorphous tissue in these materials. But what is the effect of the presence of this oxygen on the electronic properties of nc-Si:H? Discussion of this topic, and the topic of the general effect of crystallinity on electronic properties, is a subject for the next chapter.

CHAPTER IV

DEEP STATE DISTRIBUTIONS IN NC-SI:H

4.1. Crystallinity and Deep Defect Densities

Amorphous silicon solar cells are greatly influenced by the Staebler-Wronski Effect (SWE) [64] which is the metastable decrease in the dark- and photo-conductivities of that material upon prolonged exposure to relatively intense ($\geq 200 \text{mW/cm}^2$) above-bandgap illumination. Many years of research and debate have suggested that this affect is attributable to the creation of silicon dangling bond defects during carrier recombination events. In light of this, it might be a reasonable to predict that nc-Si:H, which contains significant amounts of amorphous material, might exhibit the same type of metastable behavior. In fact, our research and the research of others show that this is not the case. Figure 4.1 shows an early trend we witnessed in metastable deep defect densities that we measured using drive level capacitance profiling (DLCP; see Chapter II). For three samples of different crystallinities (Raman insets), the figure shows profiles at two temperatures in the fully annealed state (State A) and several temperatures in the metastable degraded state (State B) that resulted after 100h of exposure to 610nm long pass filtered white light from an ELH halogen light source. Only two curves are provided in State A since for this sample set the behavior of all samples in the annealed state was the same: no temperature dependence was seen in the drive-level profiles, indicating, via Equation 2.30, that deep defect densities are small compared to the free carrier density. The free carrier density is

given by the DLCP minimum, generally around $5 \cdot 10^{14} \text{ cm}^{-3}$. The upturns at the sides of the drive level profiles are an effect of the n^+ and p^+ doped layers in these devices.

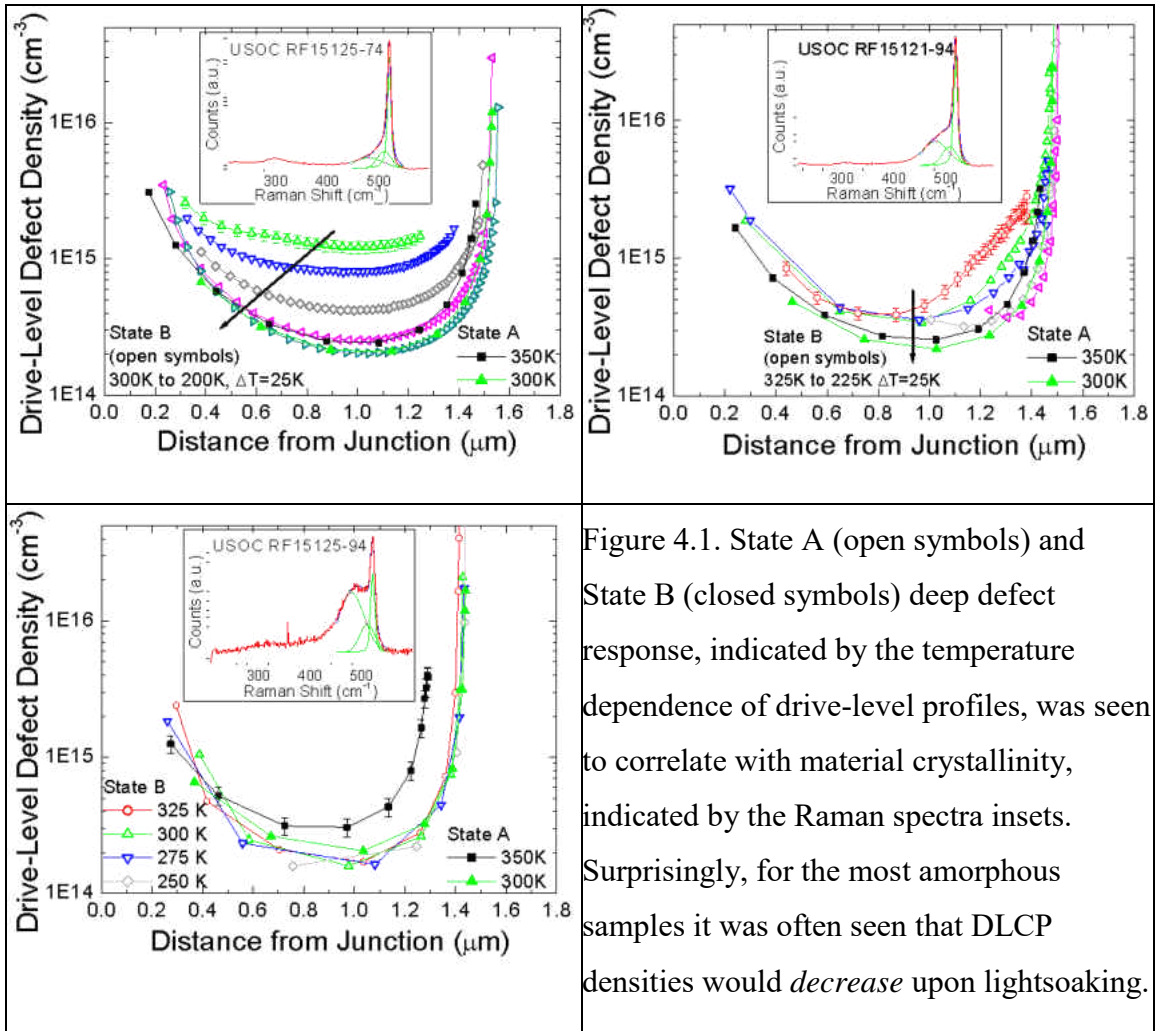


Figure 4.1. State A (open symbols) and State B (closed symbols) deep defect response, indicated by the temperature dependence of drive-level profiles, was seen to correlate with material crystallinity, indicated by the Raman spectra insets. Surprisingly, for the most amorphous samples it was often seen that DLCP densities would *decrease* upon lightsoaking.

In the degraded state, State B, the profiles showed a much different behavior.

Depending on the crystallinity of the sample State B could show a large increase in deep defect density (sample RF15125-74, upper left), a smaller increase (sample RF15121-94, upper right), or even a *decrease* in drive-level density (sample RF15125-94, lower left; see also Figure 4.2). This range of behavior is particularly intriguing since the samples showing the largest densities of deep defects in the degraded state were the most *crystalline* of the

samples measured. Indeed, this is the exact opposite behavior of what one familiar with the Staebler-Wronski Effect might predict.

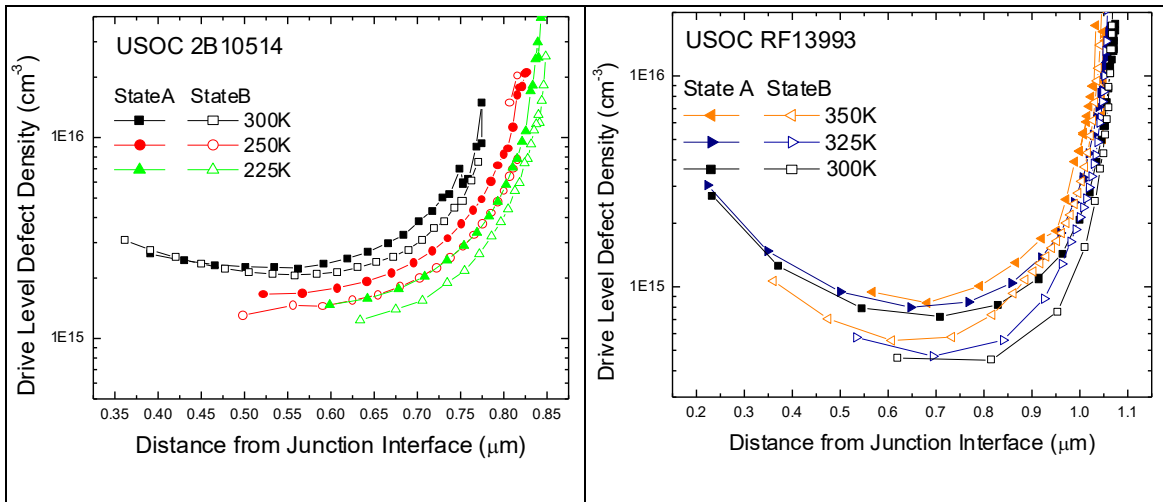


Figure 4.2. Some samples showed a metastable *decrease* in DLCP densities after lightsoaking, as shown here. This behavior, which seems at odds with the tenets of the Staebler-Wronski Effect, is discussed further in Chapter VI.

Early attempts to determine the energy of the deep defects that responded during these DLCP measurements involved analysis of C-T admittance data, as shown in Figure 4.3. Low temperature dark activation of conductivity in these samples consistently yielded values between 0.1eV and 0.35eV in State A and State B, indicating the energy difference between the Fermi level and the conduction band mobility edge. No clear trend in these values as a function of metastable state was observed. Determination of the deep defect energy level using this method was not consistently successful, however. Practically speaking, this was because activation “steps” or “peaks” in the admittance data were not clearly present for these samples, often with any steps or peaks that did appear the result of an unknown activated process. In such cases (an example of which is shown in Figure 4.3) the thermal prefactor for activation was often near 10^8 s^{-1} , which is much smaller than the

prefactor typically associated with deep defects – a fact that reiterates the unknown nature of the activated process. In a few samples, however, admittance data did yield reasonable values of the prefactor and activation energy. In such cases the prefactor had values $10^{13} \pm 5 \cdot 10^{12} \text{ s}^{-1}$ and activation energies between 0.8 and 0.4 eV.

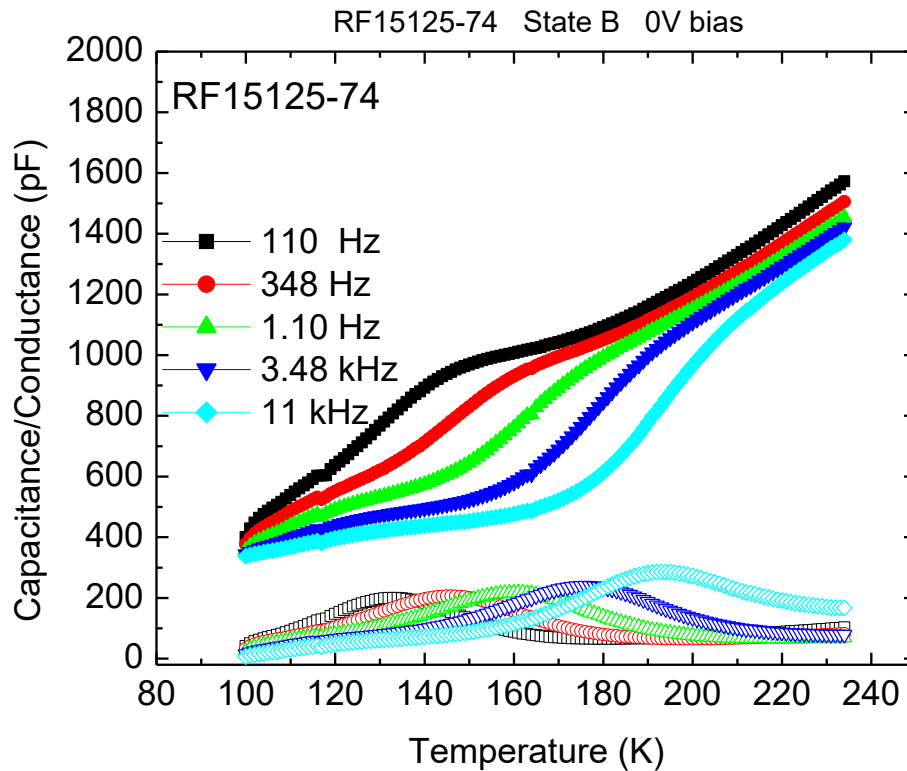


Figure 4.3. An example of State B admittance data for the most crystalline material shown in Figure 4.1. The activation “step” in capacitance does not correspond to the temperature-dependent behavior of the DLCP density, indicating that some other process is causing this effect.

One primary task therefore became to explain this correlation of defect density and crystallinity amidst the obfuscating conduction processes seen in admittance spectroscopy. Optical measurements have offered some significant clues (Chapter V) as have correlations of these defect densities with oxygen and hydrogen, as well as the results from two sets of

samples that were prepared much thicker and showed defect profiles that yielded themselves to particularly detailed modeling analysis. These results are the topic of the rest of this chapter.

4.2. Correlations with Oxygen and Hydrogen Content

In Chapter III a correlation between oxygen content and crystallinity was discussed. Reasons for the presence of oxygen were asserted to be thermal oxidation during film growth and post-deposition oxygen uptake. Given the correlation of deep defect density with crystallinity in the results discussed so far, we investigated whether measurements of the oxygen content of these films would correlate with the defect density determined using the DLCP method.

For the nc-Si:H samples in this study we indeed found this to be true. Defect densities determined using DLCP correlate well with two oxygen level indicators found using TOF-SIMS: the ratio of oxygen counts to hydrogen counts $[O]/[H]$ and, less saliently, the $[O]/[^{30}\text{Si}]$ ratio. The first of these relationships is displayed in Figure 4.4 (right). The independent correlations of the deep defect density and oxygen content with crystallinity are also shown (bottom and top left, respectively). By comparing DLCP data at different temperatures and frequencies (see Section 4.3) we determined the activation energies of these defects to be $E_C - 0.65 \pm 0.05 \text{ eV}$ in the annealed state with a thermal prefactor of $8 \cdot 10^{11} \text{ s}^{-1}$. In addition, within 0.1 to 0.3 μm of the top p/i barrier we detected a separate band of defects responding with energies near $E_C - 0.4 \text{ eV}$, agreeing with gap state defect energies

suggested by some other studies. [65,66] Unfortunately we had insufficient data to correlate this shallower defect to compositional/structural features.

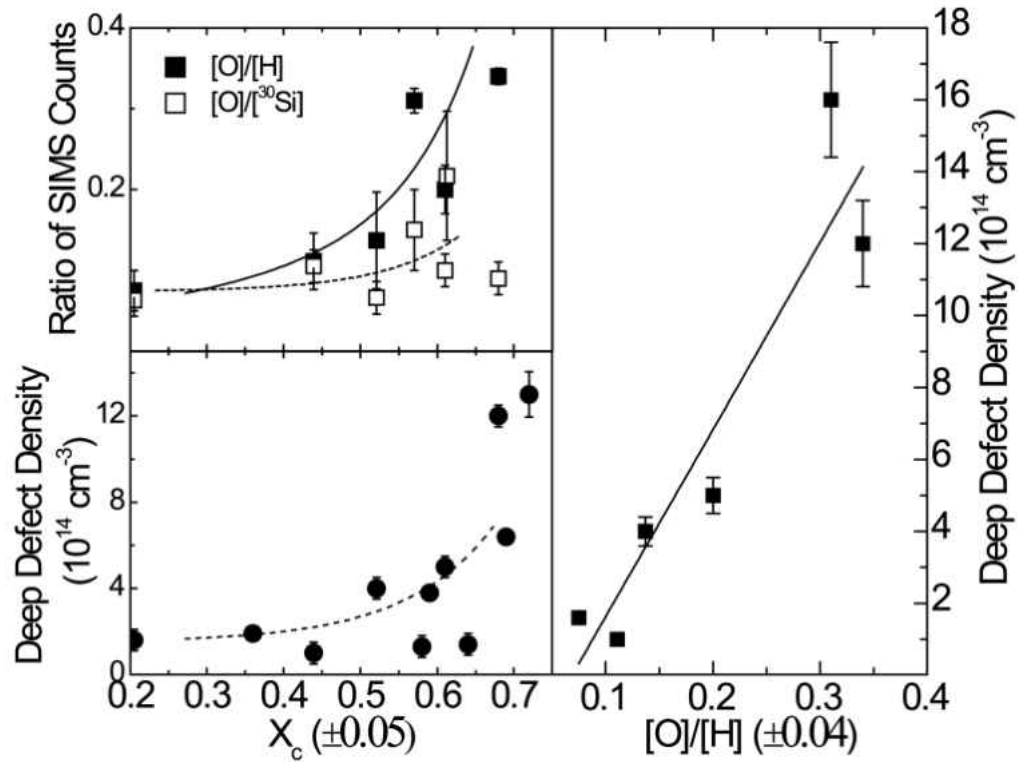


Figure 4.4. Oxygen content, measured by $[O]/[H]$ and $[O]/[^{30}Si]$ SIMS count ratios (above left), and DLCP densities (lower left) both correlated with device crystallinity. In particular, a very good correlation was seen between the $[O]/[H]$ concentration and deep defect density (right). This could suggest that deep defects are the result of an H-mitigated oxygen-based center.

Inferring a direct causal connection from these correlations is difficult. Several authors have proposed that in a-Si:H, silicon dangling bonds in the neighborhood of oxygen impurities do indeed introduce states into the bandgap. [67-70] Tight-binding calculations, supported by experiment, have suggested that these oxygen-influenced dangling bond states occur at energies $E_C - 0.68\text{eV}$. [68,70] These previous results may suggest a direct link between the $E_C - 0.65\text{eV}$ defect density and the oxygen content seen in

this study, where in this case grain boundaries may play a role in defect formation (discussed further below). It is also possible that oxygen, entering the films during growth or by gaseous or aqueous post deposition uptake, is merely an indicator of the crystalline phase volume fraction. Indeed, if hydrogen preferentially resides in the amorphous phase of the material, then one could simply conclude from Figure 4.4 that the degree of crystallinity itself is primarily responsible for the increase in deep defects revealed by DLCP.⁵

To distinguish among these possibilities we examined the oxygen and defect distribution within individual films. Figure 4.5 shows oxygen densities (left axis) deduced from $[O]/[^{30}\text{Si}]$ SIMS count data and deep defect distributions deduced from DLCP data⁸ (right axis) for two devices of similar average crystallinity. For these two devices, a good spatial correlation between the presence of oxygen and bulk defects of energy $E_C - 0.65 \pm 0.05 \text{ eV}$ is seen. These deep defect density increases occur at oxygen contents at or above the observed $\sim 10^{19} \text{ atoms/cm}^{-3}$ threshold for oxygen related electronic changes in a-Si:H. [71,72] From these data we estimate that there are roughly 10^5 oxygen atoms for each deep defect measured using DLCP. The magnitude of this ratio could have several interpretations. Firstly, hydrogen may indeed compensate the majority of any oxygen related defect states; note that this ratio is significantly larger for Sample 2 (triangles in Figure 4.5) in which the hydrogen content is twice as high. Secondly, oxygen like hydrogen, may congregate in grain boundary regions thereby only forming defect complexes in spatially constrained portions of the films, an interpretation supported by H-assisted oxygen diffusion in crystalline and polycrystalline silicon. [59,73] In this case,

⁸ Section 4.3 describes the DLCP curve modeling process and how these deep state distributions are derived.

only a small fraction of oxygen could be available to create states at the energies we have measured. A consequence of this interpretation could be that oxygen is very inefficient at forming defects in well hydrogenated, well mixed nc-Si:H. [74]

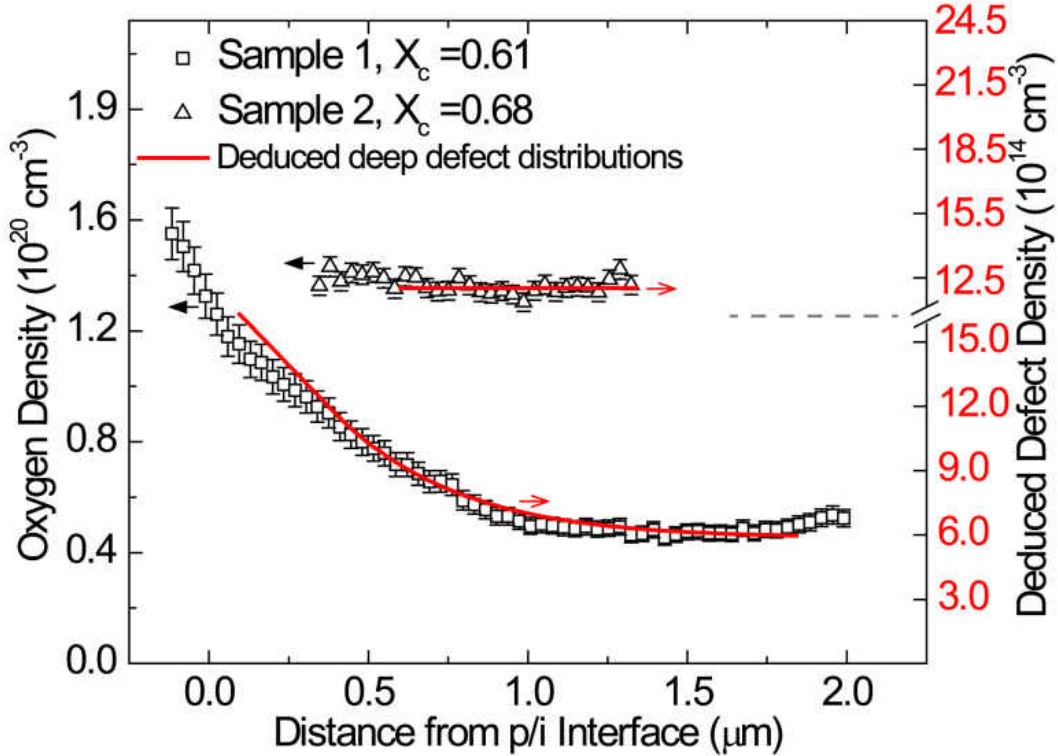


Figure 4.5. Spatial correlations between oxygen concentrations and $E_C-0.7\text{eV}$ deep defect densities were also observed within individual films. The deep defect distributions were derived via modeling of DLCP data. The energy depth of such defects appear to become shallower upon lightsoaking.

4.3. Modeling Deep Defect Densities

Our early DLCP based experiments on nc-Si:H yielded the results that were discussed in Section 4.1 – namely, that deep defect response in DLCP correlated closely with crystallinity. Later experiments focused on the behavior of samples that were purposefully prepared with much thicker intrinsic layers (between 2-3μm) than the early

batch of samples (typically $\leq 1\mu\text{m}$). The result was that we could deduce electronic structure which was less influenced by the highly doped n^+ and p^+ layers. Thicker devices also contained larger densities of free carriers in the annealed state, typically around $5 \cdot 10^{14} \text{ cm}^{-3}$. In short, these devices exhibited behavior whose properties allowed detailed modeling of the DLCP response which helped in our understanding of nc-Si:H's electrical properties considerably.

Figure 4.6 shows the kind of behavior typical of thicker samples. The State A data (Figure 4.6, left) indicates a clear shallow state density in the bulk near $7 \cdot 10^{14} \text{ cm}^{-1}$ and a temperature dependence that suggests a significant number of defects near the p-n junction.

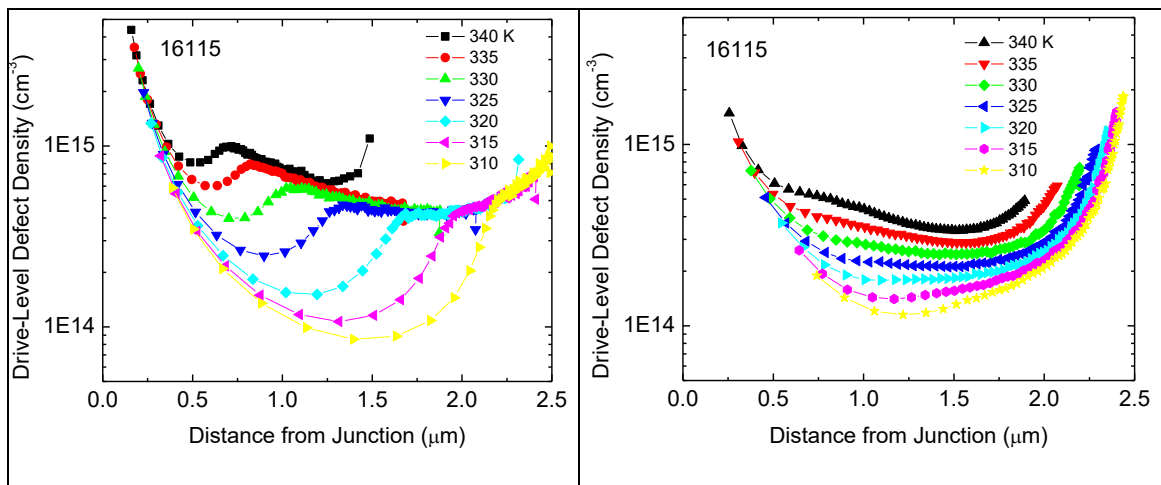


Figure 4.6. A few samples prepared with thicker intrinsic layers showed curious State A (left) and State B (right) drive level profiles. The exact shapes of these profiles could be reproduced via modeling efforts.

Most notably, the State A data contains a large ‘dip’ that always occurs over a particular reverse bias range. The shape of these drive level profiles is quite strange, and at first glance, this dip seemed to suggest a sudden decrease of the density of states in the bandgap; an unexpected result. Furthermore, the metastable transition from the State A

DLCP data to the State B curves from the same sample (Figure 4.6, right) was also initially very puzzling.

The first step to understanding this data was to verify that the DLCP response in State A was indeed an activated process. That is, if the DLCP experiment was repeated for a range of frequencies but at constant temperature (instead of vice versa) would the experiment reproduce the same results? The answer to this was affirmative (see Figure 4.7) and we began to think seriously about what these DLCP were telling us about the energetic and spatial distributions of defects.

To unlock the secrets these DLCP were hiding from us we modeled them using a custom modeling program developed for this purpose by Dr. J. D. Cohen. [75,76] Luckily, throughout this modeling process many parameters were already approximately known, such as the Fermi level depth and the free carrier densities; and some parameters that we didn't know could be constrained. The details of this curve fitting process are tedious (See Appendix A for further discussion and example fits), but the method used in this study is described generally as follows:

- 1.) Mathematically treat the intrinsic layer as consisting of three distinct regions where the distribution of gap states can be unique in each individual region; mix the properties of adjacent regions on a user-defined length scale.
- 2.) Choose a drive-level curve to model with a known measurement temperature, frequency, and thermal prefactor for responding states (i.e. – a known E_c) and known dc reverse bias values. Input the bulk free carrier densities known from DLCP data and adjust deep defect densities,

energetic distributions, and spatial distributions until modeled data roughly match the real data in magnitude and reverse bias behavior.

- 3.) Insure the modeled density of deep defects is correct by simultaneously modeling CV profiles as well as DLCP data.
- 4.) Improve the fit by correctly modeling the DLCP dependence on E_c .
- 5.) Improve the fit by applying any additional constraints to fit parameters, if possible.

Results of these fitting procedures in State A are shown overlaid with both the temperature and frequency domain DLCP data in Figure 4.7. The density of states distribution that reproduced this data is reproduced schematically in Figure 4.8 and is explained as follows.

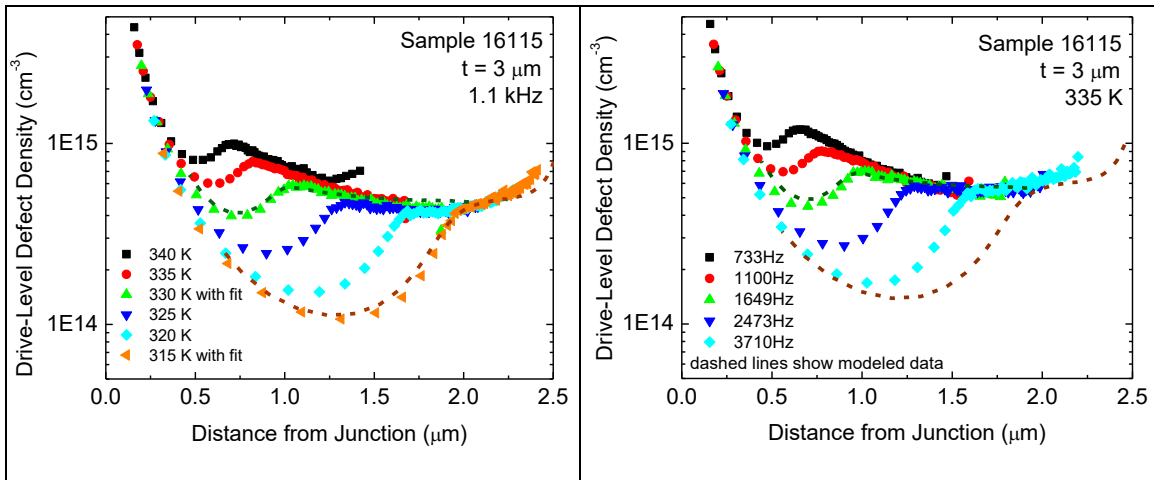


Figure 4.7. The quantitative agreement between temperature (left) and frequency (right) domain data underscore the thermally-activated nature of these drive level profiles. Also shown are modeled fits to the data (dashed lines).

The dip in this data did not indicate a drop in density of states near the p-n junction, rather the dip is the result of the quasi-Fermi level crossing a relatively shallow mid-gap

state at a particular value of reverse bias. Figure 4.8 (left) shows a bandgap diagram describing the situation for DLCP data lying *outside* the dip (e.g. – the signal at 1.5 μ m and 330K in Figure 4.7, left). In this situation, the contribution to the DLCP signal is a mixture of shallow states (free carriers) and gap states located at energy $E_C - 0.65 \pm 0.05$ eV. The response from the shallow defect is not seen since at this particular value of reverse bias, all such states lie above E_F^* . At a particular value of reverse bias, however, the shallower states will begin to cross E_F^* and they will start contributing to the DLCP signal. When this happens, the dipole moment of charge response, $\langle x \rangle$, will rapidly shift toward the interface. Since the DLCP defect density is inversely proportional to dC/dV , this shift suppresses the drive level profile in this region and produces the “dip”. This highly structured DLCP response was serendipitous for a couple of reasons. First, it allows one to accurately model the energetic depth and spatial distribution of the deep defect far from the interface with a high degree of certainty, since the shape of the drive-level profile is extremely sensitive to these parameters. Secondly, it provided a striking example of a characteristic behavior that we later determined to be generally true even for samples that did not show noticeably strange behavior in their drive level profiles.

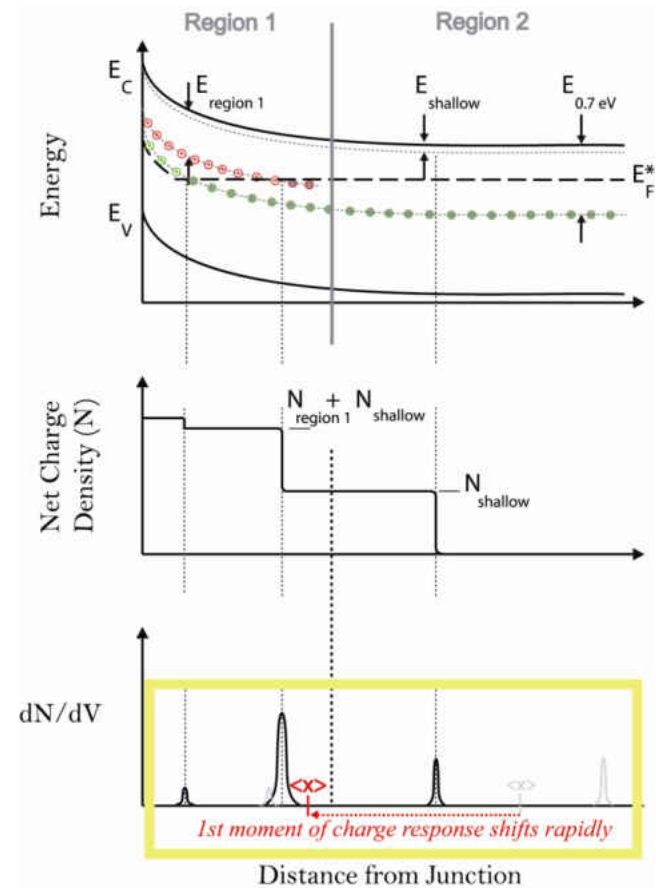
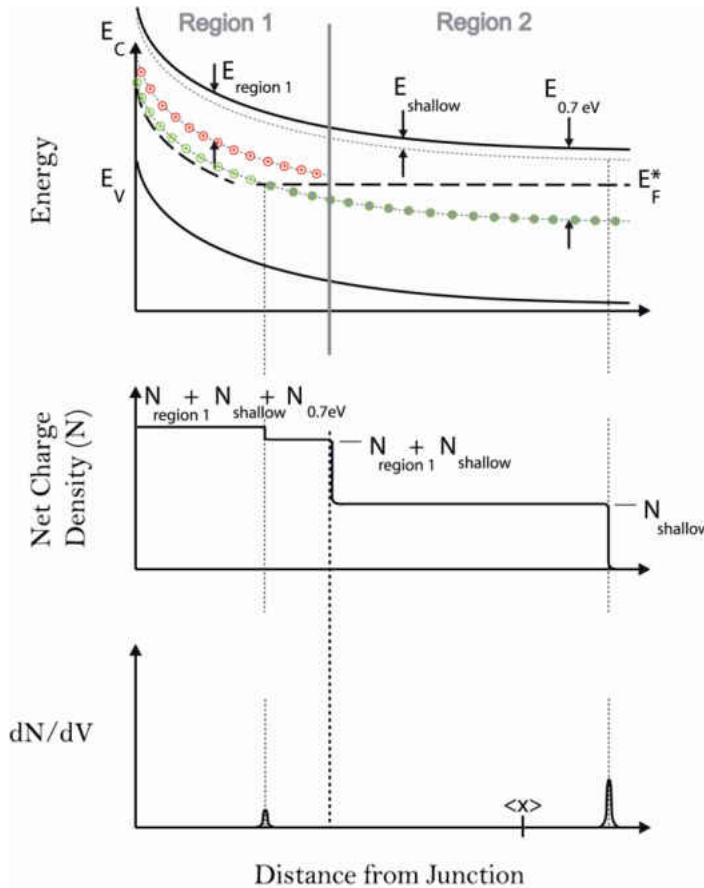


Figure 4.8. A schematic describing the only density of states configuration found to adequately describe the State A drive level profiles of thick nc-Si:H samples. The dip was found to occur as the Fermi level crossed a relatively shallow ($\sim 0.4\text{eV}$) defect located near the p-n junction (right) while at large values of reverse bias it did not (left).

Modeling the Temperature Dependence

When modeling the temperature dependence of the profiles from Figure 4.7, we discovered that the densities of deep and shallow states actually varied. However, we also saw that the additional constraint could be made that the sum of deep states and shallow states (free carriers) remain constant for each metastable state. This constraint, which asserts total charge neutrality, is illustrated in Figure 4.9.

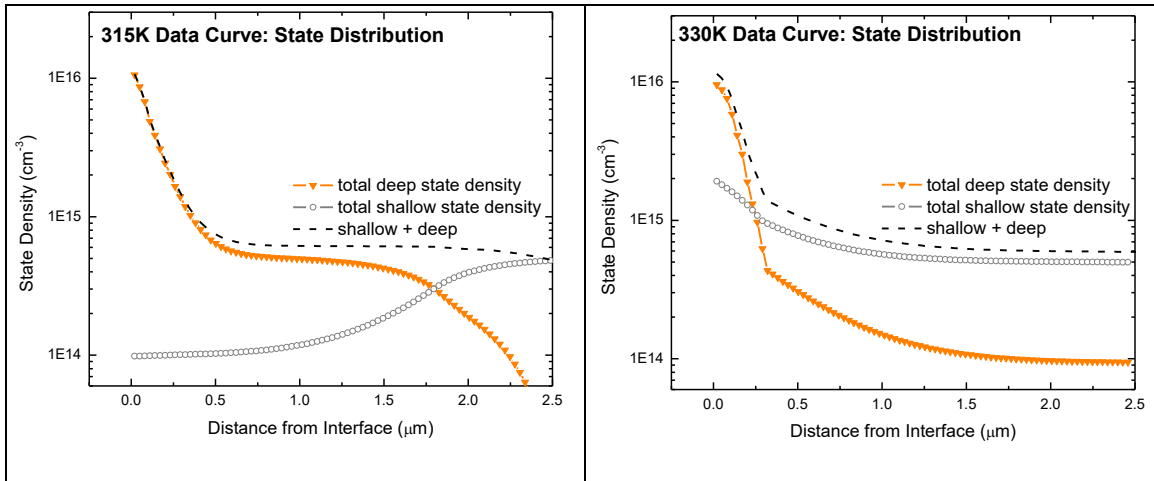


Figure 4.9. Spatial distributions of the sum of *all* deep states and shallow states (free carriers) were constrained to obey a sum rule across temperature changes for each metastable state that was modeled. The temperature dependence of the drive-level profiles was reproduced by changing the spatial extent of the region in which free carrier density was low.

Figure 4.9 details the state distributions that produce the DLCP curves from Figure 4.7. The large increase of deep state density within 0.4 μm of the interface is primarily indicates the 0.4eV defect while the remainder of the deep state distribution primarily indicates the 0.7eV defect. Note that these density curves do not distinguish between the

energy depth of the two defect states.

The striking feature of these modeled data is the *spatial dependence* of the conserved exchange between deep and shallow state densities as the temperature is changed. We modeled the temperature dependence of each metastable state by starting with a certain deep/shallow state distribution and then altering the physical distance from the junction at which the shallow states lose density to the deep states. One interpretation of this phenomenon is the “freezing out” of conduction in certain regions of the sample via a temperature-dependent transport process like is described in Section 1.4. A schematic illustrating this effect is given in Figure 4.10. In such an interpretation, as carriers are excluded from moving across certain spatial regions via conduction band states, they begin to respond to the DLCP measurement as if they were occupying deep gap states; thus they maintain charge neutrality throughout the material.

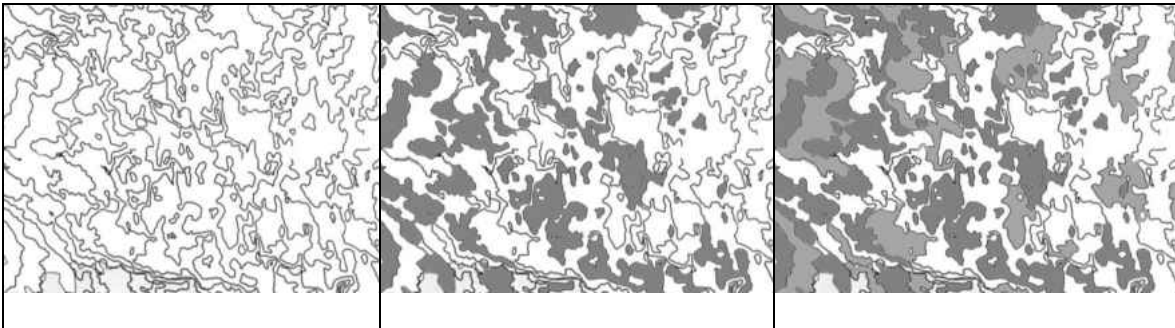


Figure 4.10. A schematic representation of a randomized potential landscape, as described in Section 1.4. Grey areas represent regions where carrier conduction (percolation) is not possible. Our modeling results are consistent with a spatially dependent freezeout of conduction through conduction band states as the temperature is lowered, as shown in the progression in the figure.

This interpretation is consistent with considering a nc-Si:H whose randomized potential landscape coincides with randomly arranged nanocrystallite/grain

boundary/amorphous regions. Given a flat Fermi level describing densities of carriers within this potential landscape, regions of high potential energy will contain fewer carriers than regions of low potential energy. The interpretation given here is synonymous with claiming that carrier excluded from regions of high potential energy are preferentially placed in deep defects – the assumed lowest energy states for majority carriers within nc-Si:H.

Regardless of the interpretation, it was this constrained exchange which ultimately made attempts to reconcile deep state distributions with the temperature dependence of DLCP successful.

Modeling the Metastable State Change

In the annealed state, State A, the primary benefit of our modeling attempts was to reveal the energies and spatial distributions of mid-gap defects in the samples studied. But these distributions and even *energies* appear to change upon lightsoaking. Figure 4.11 (left) outlines the curious degradation sequence seen for the sample in question. As is visible in the figure, upon lightsoaking (200mW/cm² 610nm LP filtered white light) the drive level profiles first begin to *decrease* in magnitude up until lightsoak times of roughly 500m, then begin to *increase* and saturate at lightsoak times approaching 8000m. After successfully describing the DLCP response and temperature dependence in the annealed state, we worked to model this entire metastable state change and were met with some success as is shown in Figure 4.11 (right).

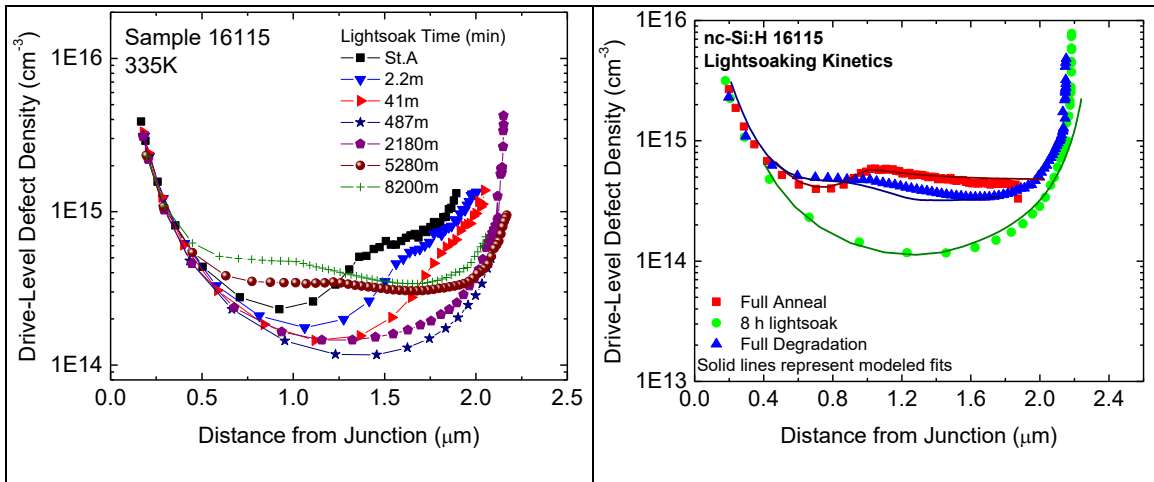


Figure 4.11. DLCP densities (left) were seen to first decrease, then later increase as a function of lightsoaking. These data were modeled (solid curves, right) by considering monotonic decreases in free carrier density and a monotonic density increase and simultaneous energy shift of deep defects from $E_C-0.7\text{eV}$ to $E_C-0.55\text{eV}$.

This sequence at first appears troubling, since it appears to suggest non-monotonic changes in material properties upon lightsoaking. However our modeling attempts showed that, in fact, this strange lightsoaking behavior was completely describable by considering monotonic changes in the free carrier density and the density of deep defects (see Appendix A).

Interpretation of the Degradation Sequence

At early lightsoak times, up to about 500m, DLCP densities were seen to decrease. This effect was reproduced via modeling by decreasing the free carrier density from $5 \cdot 10^{14} \text{cm}^{-3}$ to a minimum value of $1 \cdot 10^{14} \text{cm}^{-3}$ in the far-interface region and by raising the 0.7eV deep defect density by a commensurate amount. It was also necessary to lower the Fermi level from $E_C-0.21\text{eV}$ to $E_C-0.24\text{eV}$. Changes in the density of the 0.4eV near-interface defect were not required in order to obtain a good fit to the data.

At lightsoak times between 500m and 8000m the drive-level density is seen to increase. This was achieved in modeling by lowering the Fermi level from $E_C-0.24\text{eV}$ to $E_C-0.28\text{eV}$ and by increasing the density of deep defects. Surprisingly, we could not reproduce the State B DLCP and CV profiles without *lowering the energy depth of the 0.7eV defect* from 0.7eV below the conduction band to 0.55eV below the conduction band. Since the drive level measurement measures all defect response between the Fermi level and E_c , and does not give direct spatial information about deep defects, we can only claim that at the latest stages of lightsoaking a shallower state is created *somewhere* throughout the intrinsic layer. This level may indeed be a charge state of the 0.7eV defect, or it could be a different level altogether. We discuss these possibilities in Chapter VI.

For reasons discussed in the next section, we assume that this 0.7eV defect is located in bands of amorphous tissue. If we also assume that occupied 0.7eV defects are negatively charged, which we denote by D^- (see discussion, Chapter VI) then the entire lightsoaking sequence is described by Figure 4.12.

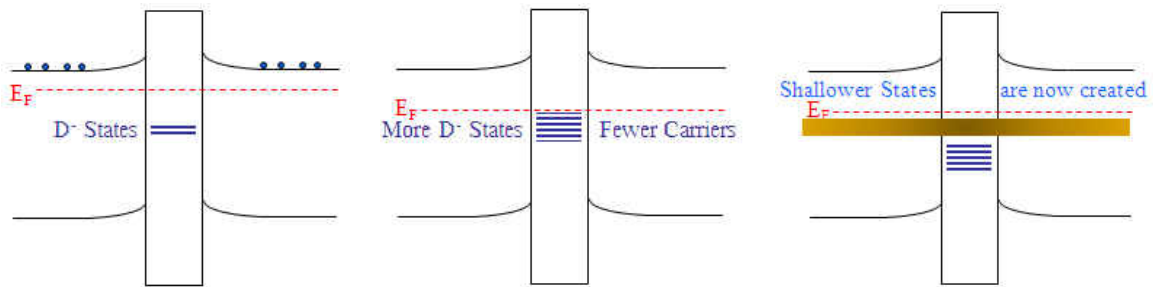


Figure 4.12. Bandgap schematics showing grain boundary material surrounded by crystallite material illustrate the process producing the lightsoak sequence from Figure 4.11. State A (left) carrier densities reduce and charged deep defect densities increase at early stages of lightsoaking (center). At later stages of lightsoaking free carrier densities are low and shallower, neutral defects are created.

4.4. Host Phase of Deep Defects

That it is unphysical to measure a 0.7eV defect in the nanocrystalline phase (since such a defect would lie below half the bandgap) is a strong argument for this defect to be located in the amorphous phase of the samples studied here. However, we did also perform one degradation study, reproducing the work of others on these same materials [77], that also suggests that these defects reside in the amorphous phase.

If the 0.7eV defect resides in the amorphous tissue, then one would expect a wavelength dependence to light-induced degradation. Since the amorphous phase has a wider bandgap than the crystalline phase (1.7eV and 1.1eV, respectively) and some authors estimate its band offsets for the conduction and valence band edges are 0.05eV and 0.58eV respectively, one would not expect carriers generated in the nanocrystallite phase to recombine and form defects in the amorphous phase. Thus for such material, light degradation at optical energies less than the amorphous phase bandgap energy are not expected.

Taking great care to insure that carrier generation rates were kept constant for the degradation wavelengths used (850nm long-pass and 610nm long-pass) we performed this experiment for sample similar to that which we subjected extensive modeling. Since the degradation sequence for this type of sample was verified to follow that shown Figure 4.11 (left) it was expected that for short lightsoak times, the DLCP density would show a slight *decrease* (indicating a loss in free carrier density) if the incident optical energy was greater than 1.7eV. Likewise, no change should be seen for lower optical energies. These were indeed the results we obtained, and they are shown in Figure 4.13.

Therefore, our evidence for the defect which has energy $E_C-0.7\text{eV}$ to reside in the amorphous, or grain boundary tissue is threefold. First, such an energy depth suggests a large ($>1.4\text{eV}$) bandgap energy. Secondly, the association of this defect with the presence of oxygen suggests that such states reside in the grain boundary material (see Figure 3.12 and discussion). Finally, a lightsoak study performed by us was found to repeat the work of others who have observed no light induced degradation for these materials at optical energies less than the a-Si:H bandgap energy.

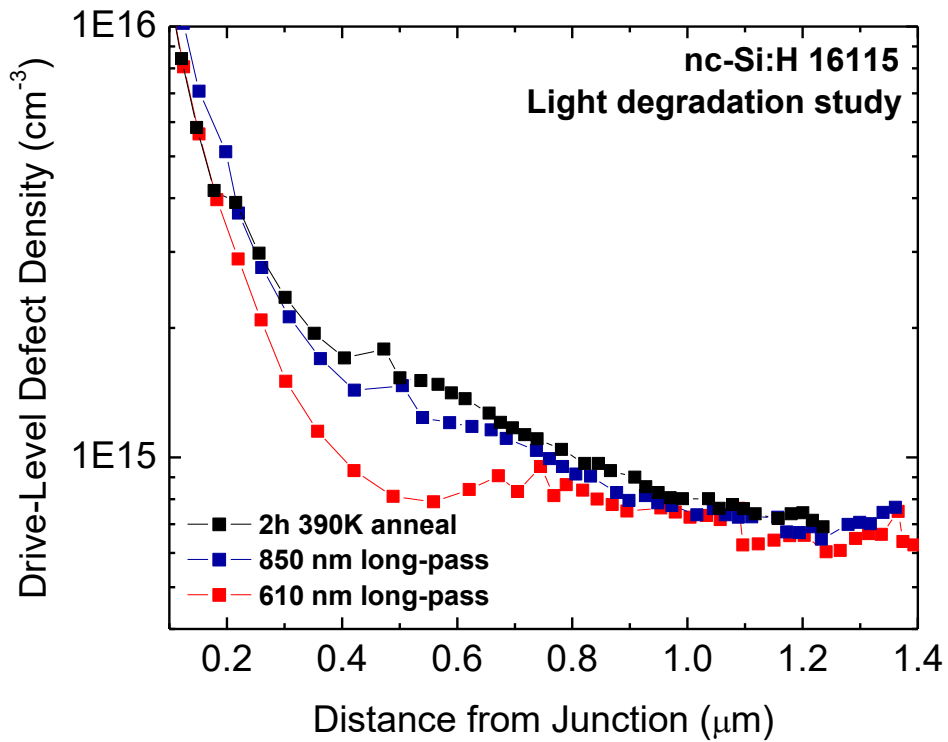


Figure 4.13. For thick samples exhibiting the degradation response shown in Figure 4.11, light-induced degradation does not occur at incident photon energies of 1.5eV , but does occur for 2eV light. This strongly suggests that recombination events in the amorphous/grain boundary phase are the cause of metastability.

4.5. Presence of the Near Interface Defect of Transition Energy 0.4eV

Earlier in this chapter we noted that we identified two separate deep defects in these materials. The defect that appears at a transition energy of 0.7eV in the annealed state has been discussed in detail; we believe this defect is related to oxygen content and is located in the amorphous/GB tissue of these materials. The second, shallower defect was only first identified during modeling of DLCP data and was only observed in the near interface region, with the bulk of the defect density usually constrained within 0.3 μm of the p/i interface. To illustrate the spatial distributions of this shallower defect, Figure 4.14 displays the state distributions of the 0.7eV defect (orange triangles), shallow states (open symbols) and the near interface 0.4eV defect (solid blue line). The 0.4eV defect was not considered when calculating the sum “shallow+deep” in these plots, nor is it included in “total deep state density”. Therefore, Figure 4.14 illustrates the deduced spatial distributions of the 0.7eV and 0.4eV defects independently.

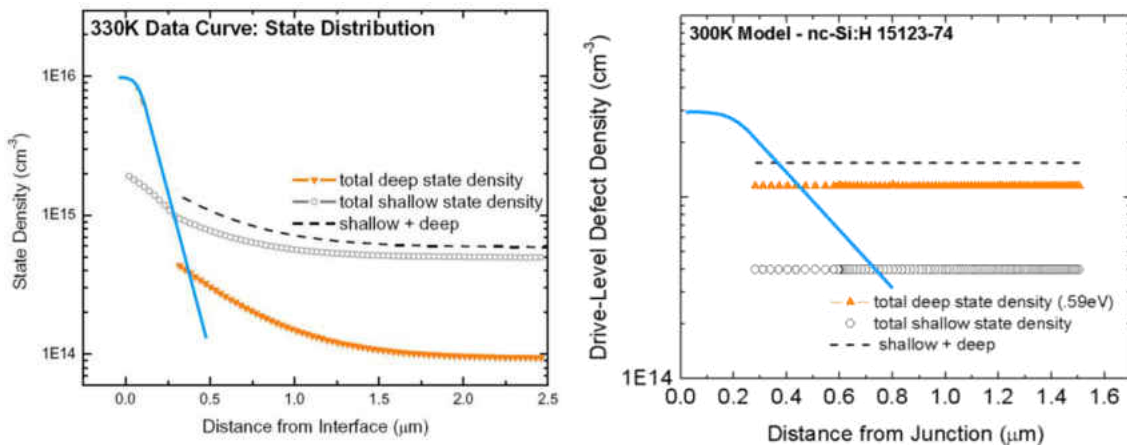


Figure 4.14. Spatial distributions of shallow states (free carriers) and both deep defect states. The solid light blue line indicates the spatial distribution of the 0.4eV deep defects, and the orange triangles indicate the spatial distribution of the 0.7eV defects.

It was after considering the data from Figure 4.14 that we began to realize the presence of the 0.4eV defect was more universal than we had initially supposed. Figure 4.14 (left) shows the deduced deep state distributions for sample 16115, the sample from Figure 4.6 which showed a highly pronounced “dip” in the State A DLCP data. We quickly realized that this “dip” indicated the presence of the 0.4eV state. However, the data from Figure 4.14 (right) is from a sample that showed *no* pronounced DLCP dip, or any other immediately obvious indicator of a near-interface state – yet the 0.4eV state was required to reproduce the DLCP results for this sample via modeling. The State A and State B DLCP data for this sample is given in Figure 4.15.

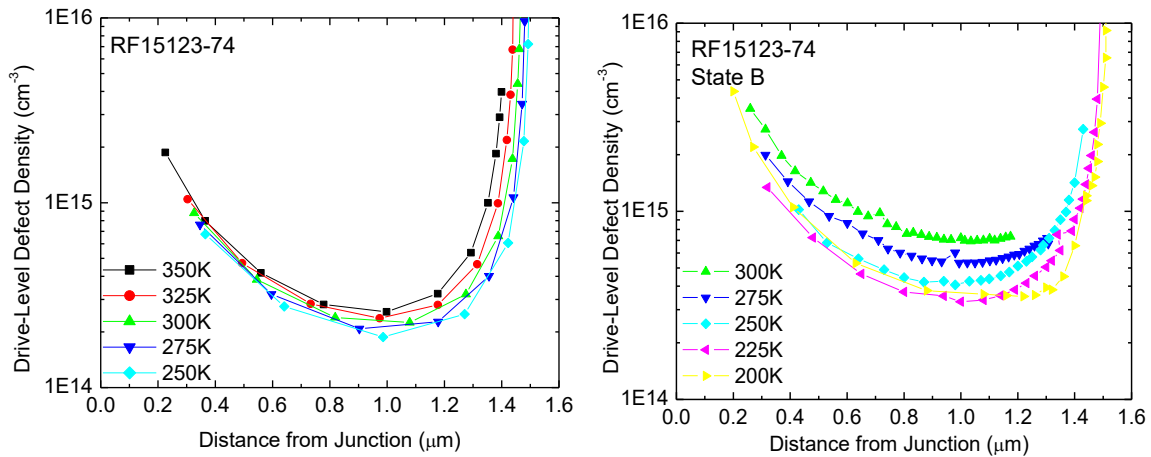


Figure 4.15. The original DLCP data from which the deep and shallow state distributions in Figure 4.13 (right) were derived (sample 15123-74; $X_c=0.69$). A specific near-interface distribution of deep states with transition energy 0.4eV was required to reproduce these DLCP results, despite the fact that no obvious “dip” betrayed the presence of this defect state. In retrospect, the broad spatial dependence of the DLCP signal out to 0.8mm from the junction interface indicates the presence of the 0.4eV state in this data.

After this realization, we began to look for evidence of this shallower defect in the drive level profiles of other samples and we were not surprised to find that this shallower defect was indicated in *many* of our DLCP data sets for samples with crystalline fractions near or above $X_c=0.6$. Some examples of profiles that illustrate this are given in Figure 4.16.

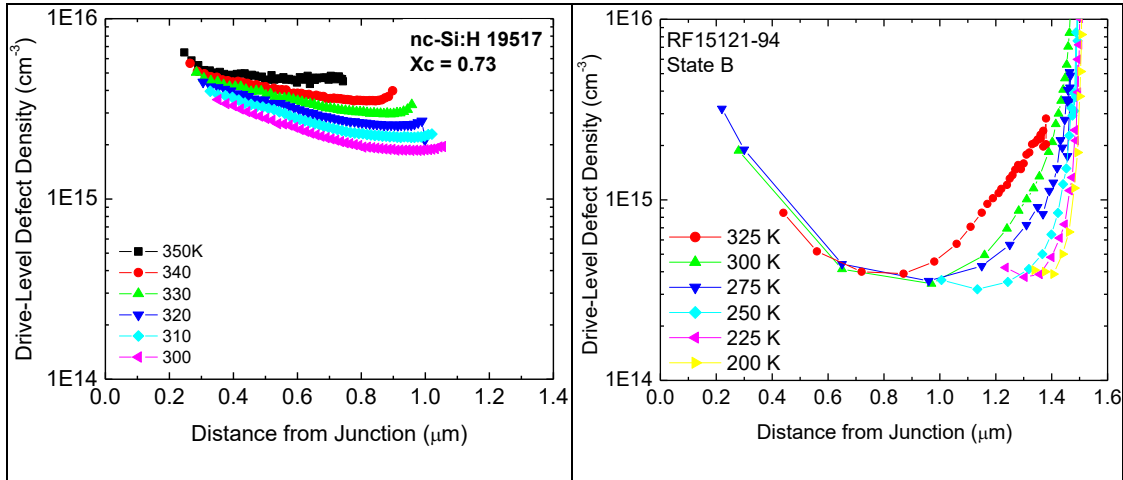


Figure 4.16. These State B data both indicate the presence of a shallow, near-interface defect. (left) the lowest temperature profile indicates the spatial dependence of the 0.4eV defect while the 350K profile indicates the spatial dependence of the 0.7eV state. (right) This State B data is reminiscent of the annealed state data for sample 16115, but exhibits a much more subtle “dip” which we once again attribute to the 0.4eV near interface state. For this sample $X_c=0.59$.

But what is the physical origin of this near-interface defect? One idea was that the defect is the result of a dopant or atmospheric contaminant that has diffused into the intrinsic layer through the junction interface. For example, carbon is a known donor in crystalline silicon that creates a gap state of energy 0.35eV below the conduction band. [21] Initial comparisons with secondary ion mass spectrometry (SIMS) data, however, indicate that carbon is not a likely cause of this interface state. Another idea is that very small

densities of boron which have diffused from the p layer are responsible for the defect. Indeed, for a limited set of samples the presence of boron was probed using SIMS measurements. These data are shown in Figure 4.17. These results indicated that there appears to be some variation of boron content between samples, but no correlation of these boron densities have yet been made with deep defect densities of energy 0.4eV.

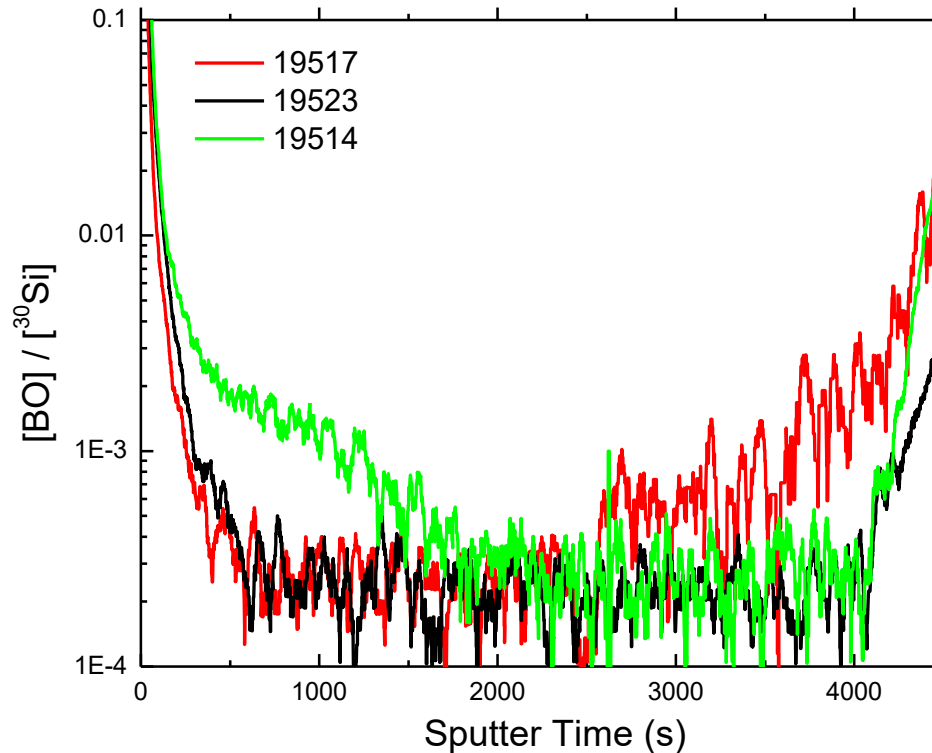


Figure 4.17. For a limited set of samples the presence of boron, in the form of the diatomic molecule BO, was investigated using secondary ion mass spectrometry. Densities of boron were very low in these samples, as seen in the figure, but spatial variation in the near-interface region is present in these samples. No correlation with the presence of 0.4eV defects has yet been determined.

In conclusion, in addition to the 0.7eV defect that we believe is present throughout the nc-Si:H absorber layer we have also identified a shallower defect of energy 0.4eV that

appears only near the p-i interface. The bulk of the defect density of this shallower defect is unusually contained within $0.3\mu\text{m}$ of the p/i interface, although the full distribution of this defect can produce features in the drive level profiles out to distances of $0.8\mu\text{m}$ from the p/i interface. The physical origins of this defect are most likely a molecular contaminant that has diffused into the absorber from the p layer. However, it is also a possibility that the 0.4eV is a charge state of the 0.7eV defect. Our data are inconclusive on these points.

CHAPTER V

OPTICAL DETERMINATION OF ELECTRONIC PROPERTIES

5.1. Optically Measured Deep State Distributions

To form a more complete picture of the distributions of gap states in these materials, TPC and TPI (see Section 2.6) optical spectra were also taken on many of the materials we investigated. The nominal shape of the spectra were similar to the data presented in Figure 5.1. Plotted in this figure are three curves, a TPC curve taken at 200K, a TPI curve (which extends only down to energies near 0.9eV) and a best fit curve to the TPI spectrum. In general, the shape of this spectrum is similar to that crystalline silicon, exhibiting a bandgap energy just over 1eV. However, unlike crystalline silicon which has no exponential bandtails at the edges of the conduction or valence bands, these spectra show significant exponential behavior between optical energies of 1.0eV and 1.6eV. Urbach energies for bandtails in these materials were found to consistently lie in the range of 50meV to 60meV. For the spectrum shown, the Urbach energy is 55meV. Also apparent in these data is a mid-gap distribution of defects that are centered at an optical excitation energy of 0.654eV. The presence of such defects was correlated to a significant deep defect response seen in DLCP, such as that shown in Figure 4.1 (top left). We note that optical transitions of energy 0.74eV are very close to what one would expect for transitions into and out of mid-gap defect states located at the amorphous silicon mid-gap energy.

The data of Figure 5.1 were indeed nominal, but the true behavior seen over a wide range of nc-Si:H samples was incredibly varied. As was expected, most of these changes occurred as a function of material crystallinity.

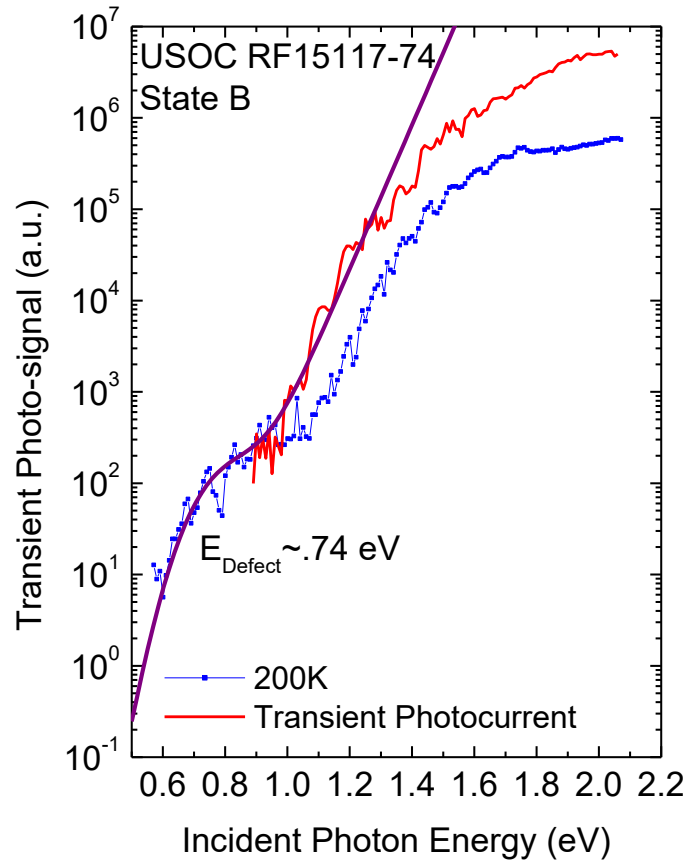


Figure 5.1. A typical nc-Si:H TPC/TPI dataset with best fit curve for a sample that exhibited significant deep state response in DLCP measurements performed in the degraded state. The presence of a significant defect band near 0.75eV seems correlated with the defect response in DLCP. The pseudo-regular fluctuations in this data is the result of thin film interference.

Our results from applying the TPC and TPI measurement methods to nc-Si:H were twofold. First, we found that the relative degree of hole vs. electron collection depended strongly on the amorphous content of the film. Secondly, we found that this relative hole collection was also very sensitive to the material's metastable state – i.e. the degree of lightsoaking. Figure 5.2 compares sets of TPC spectra that were obtained for two nc-Si:H sample devices with very different amorphous volume fractions.

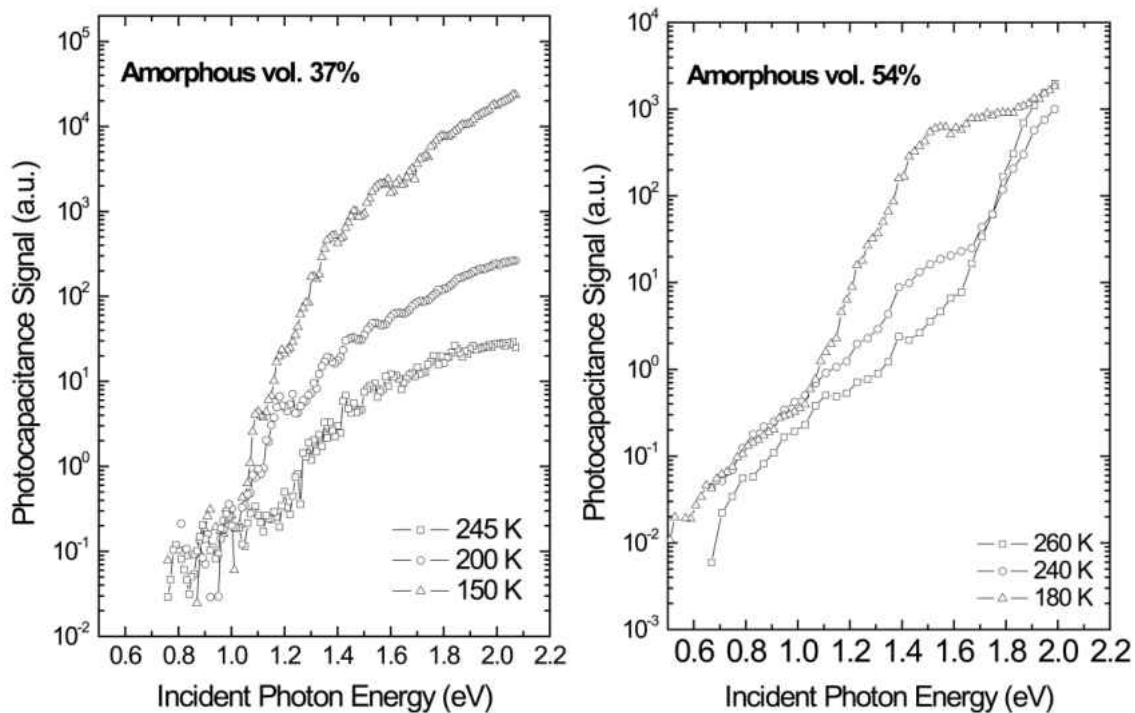


Figure 5.2. Data in the annealed state for two nc-Si:H samples of different crystalline volume fractions. For both samples, the degree of minority carrier collection decreases with temperature. (left) The overall change in this collection fraction is quite large for the more crystalline material (sample 14036). (right) the more amorphous material (sample 14657) shows a lower magnitude change, but at higher measurement temperatures a decidedly amorphous-like residual TPC spectrum is revealed, showing a bandgap energy of $\sim 1.7\text{eV}$. [78]

Figure 5.2 (left) displays the temperature dependence of a relatively low amorphous fraction sample, whose behavior was similar to other such samples, like that of Figure 5.1. At measurement temperatures typically below 275K these spectra resemble those obtained by others using the PDS measurement technique on microcrystalline Si. [46,79] As the measurement temperature is raised, the signal intensity above the crystalline Si bandgap (1.1eV) decreases monotonically. This is a result of the nature of the photocapacitance signal, discussed in Section 2.6, which is sensitive to the *difference* in carrier type collected. This is to say, while photons with energies exceeding 1.1eV excite equal numbers of electrons and holes, these carriers are not collected with equal efficiency. As a result, during the timescale of the measurement, which is on the order of 1s, a residual charge is left behind in the depletion region. The positive sign of these data indicates that holes are being collected less efficiently than the electrons, but that this asymmetry decreases with increasing temperature. Thus, the TPC signal above 1.1eV becomes smaller as the temperature is increased. From auxiliary TPI measurements on the particular sample shown in Figure 5.1 (left), we estimate that at optical energy 1.5eV the relative hole collection (compared to that of the electrons) over the 1s measurement window increases from less than 70% at 150K to over 99% at 245K.

Figure 5.2 (right) shows a set of corresponding spectra taken for a sample with a higher amorphous Si fraction that was published a few years ago. [78] Again, at lower measurement temperatures, these data appear qualitatively identical to the lowest temperature spectra of the more crystalline sample and to CPM and PDS spectra for similar materials. We again see a comparable increase in hole collection efficiency with increasing temperature above 1.1eV, indicated by the decrease in the TPC signal in this energy

regime. However, in this case the TPC signal does not decrease for all optical energies above 1.1eV. Instead, the TPC decrease appears more structured and gradually reveals a residual spectrum at measurement temperatures near 260K. This “residual spectrum” closely resembles those obtained for hydrogenated *amorphous* silicon. [80,81]

As was argued in [78], this behavior is a result of the presence of a well-defined amorphous silicon phase in this sample that actually maintains its microscopic identity with respect to its optical excitation spectrum. We believe that because total hole collection in this sample is dominated by the thermal trapping of holes in the amorphous phase, and that the “nanocrystalline TPC component” is effectively suppressed with respect to this amorphous-like TPC contribution, the amorphous silicon phase dominates the appearance of the overall TPC spectrum.

But these interesting minority-carrier dominated processes were not only observed as a function of measurement temperature, but also as a function of metastable state. Figure 5.3 compares the TPC and TPI spectra near room temperature for two additional nc-Si:H samples, again with higher and lower nanocrystallite fractions. In this case, however, we display spectra in the annealed state and also after light soaking. First of all, we note that in both cases, the TPI (photocurrent) spectra closely resemble the familiar absorption curve for micro-crystalline silicon – that is to say, spectra that show bandgap energies of roughly 1.1eV--and are essentially the same as the lower temperature TPC spectra for the samples shown in Figures 5.1 and 5.2.

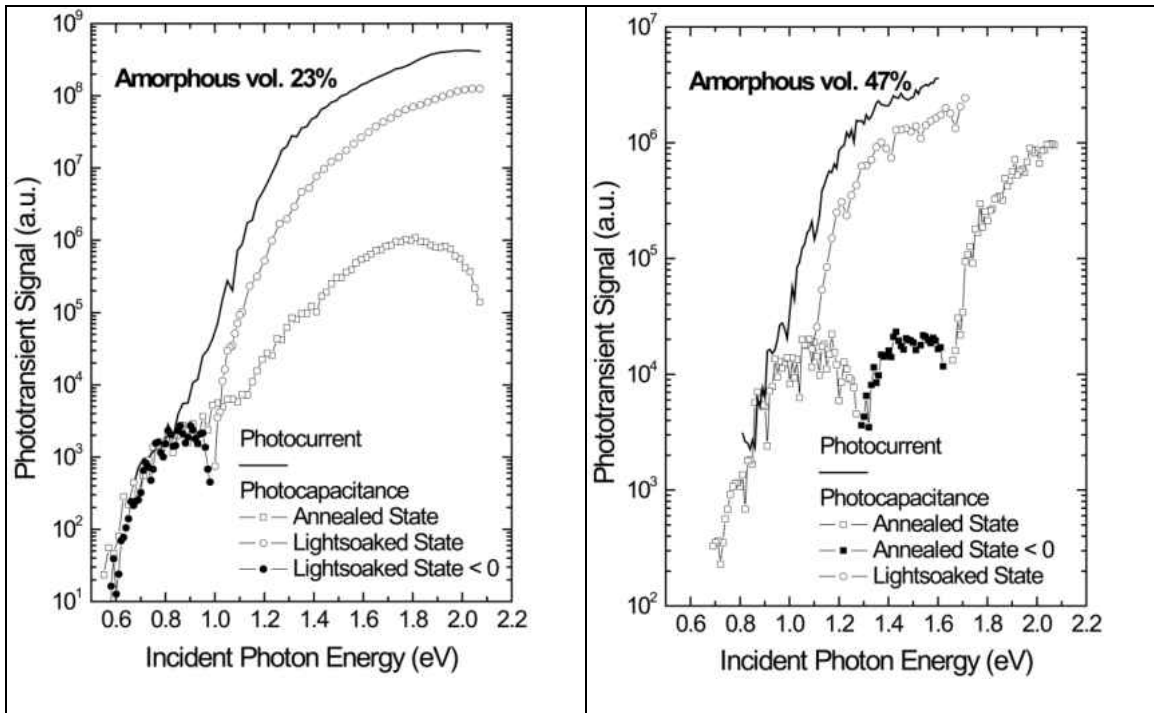


Figure 5.3. Photocapacitance (TPC) and photocurrent (TPI) data are shown in both the annealed and lightsoaked states for samples of very different crystalline volume fraction. (left) the highly crystalline film (sample 16115) shows no evidence of an a-Si:H – like bandgap. In its lightsoaked state, the negative TPC signal below optical energies of 0.9eV indicates optical transitions into deep defect states above the Fermi level. Data were taken at 325K. (right) A more amorphous film (sample 13993) shows an a-Si:H – like band edge near 1.7eV. A negative feature appears near 1.2eV in the annealed state. Data were taken at 295K.

The factor of ~ 200 suppression of TPC relative to TPI in the annealed state and above 1.4eV for both samples indicates that at least 99% of the minority carriers generated for every majority carrier are being collected during over the measurement's 1s timescale. It is important to point out that these hole collection fractions do occur over different temperature ranges for these two samples of different crystallite content, at 295K for the more crystalline sample and at 325K for the more amorphous one. This behavior changes significantly with lightsoaking, however, and the TPC signal above 1.1eV increases significantly in both cases, implying that the relative hole collection has dramatically

decreased to below 90% . This behavior after light soaking has been universally observed for all the United Solar nc-Si:H we have examined by these methods. These results are summarized and correlated to certain cell performance parameters in Figure 5.4 and Table5.1.

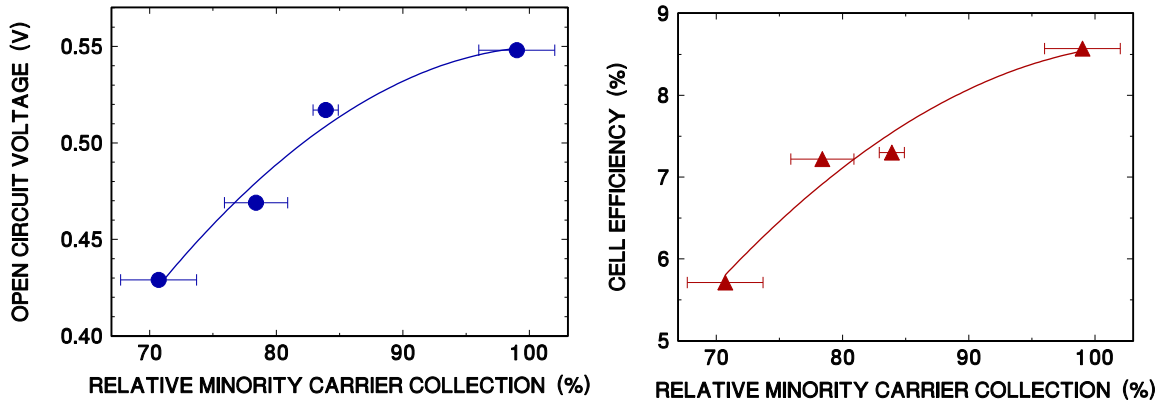


Figure 5.4. Among the earliest results of this study was a correlation between minority carrier collection and cell performance in the annealed state.

Sample	X_a	V_{oc}	Eff. (%)	f_p^A	f_p^B
16114	0.71	0.568	5.4	0.97	0.42
14657	0.54	N/A	N/A	1.0	0.95
13993	0.47	0.548	8.57	>1.0	0.75
16115	0.23	0.448	4.42	0.98	0.80

Table 5.1. Hole collection fractions, f_p , at 300K determined by the TPC and TPI signal ratios at a photon energies of 1.5 eV for a set of nc-Si:H sample devices of various amorphous volume fractions, X_a . State A and State B collection fractions are indicated by the superscripts. In all cases, the hole collection fractions, f_p , decrease after light soaking.

As with the comparison shown in Figure 5.2, the nc-Si:H film with the higher amorphous Si fraction shows a distinct amorphous phase in its TPC spectrum. For this sample the “amorphous-like” to “crystalline-like” crossover occurred at temperatures near 285 K. Any indication of an amorphous phase is absent for the sample with the higher nanocrystalline fraction. Thus, qualitatively, the results for these two samples are similar for the two cases displayed in Figure 5.2. However they also exhibit behavior not present in the spectra from Figure 5.2; namely, there are regions in which the TPC signal actually becomes negative (indicated by filled symbols). A negative signal in TPC is the unambiguous signature for an optical transition between a valence band state and a deep empty gap state where the excited electron can remain trapped during the timescale of the measurement. (see [82] for a more detailed discussion) In such a case, if the residual valence band hole escapes the depletion region and the electron remains trapped in the gap state, the result is a net negative residual charge in the depletion region and therefore a negative TPC signal is seen.

For these two samples of different nanocrystallite content, the negative features in the TPC spectra occur over different optical energy regimes. At the same time, no negative features appear at all for the samples discussed in Figure 5.2, regardless of the measurement temperature. The breadth of these results presents quite a significant challenge in the study of nc-Si:H materials; namely, how to account in a reasonably straightforward way for the great variety of behaviors seen in the optical spectra of these materials. Indeed, it is the same challenge we face in interpreting the DLCP and admittance data. How can a single class of material be so *diverse* in its behavior?

Before we attempt to answer this question (see Chapter VI), one may ask why

negative features appear in some TPC spectra but not in others. This is because observing a net negative TPC response requires three conditions that must be met simultaneously:

(a) There must be a large unoccupied defect band in the depletion region that is still deep enough so that electrons inserted into it are not thermally re-emitted into the conduction band too rapidly. (b) One must be able to collect the residual hole in the valence band with a reasonable efficiency and (c) Transitions from filled gap states into the conduction band that can occur over the same photon energy regime (which result in a positive TPC signal) must not be so strong that they overwhelm the transitions responsible for the negative signals.

Thus, the lack of a negative TPC regime for the more crystalline samples in Figures 5.1 and 5.2 is probably a result of item (a) listed above; that is, the lack of a sufficiently large empty defect band. Indeed, the more crystalline sample in Figure 5.3 did not exhibit a negative feature until after it was light-soaked. Likewise, the lack of a net negative signal for the more amorphous sample in Figure 5.2 is likely due to (c): the presence of a strong transition from filled gap states into the conduction band. It might also be due to a lower hole collection fraction in that sample since our data indicate a sensitivity to hole conduction through the amorphous phase. Indeed, the negative region for the more amorphous sample in Figure 5.2 also disappears at a 20K lower temperature due to decreases in hole collection.

To summarize these last few points, the observation of a negative TPC signal provides an unambiguous signature for a valence band transition into an empty defect level. However, the lack of that signature does not mean the transition is absent, only that other factors make it difficult to observe. Therefore, we believe that the two spectra shown in

Figure 5.3 provide clear evidence for a distinct crossover in the electronic properties of nc-Si:H with greater or lesser degrees of crystallinity. Can these data be brought together, however, to form a working model that we can use to understand the electronic behavior of nc-Si:H? If so, what kind of picture can account for the extraordinarily varied behavior that we see in these optical measurements? Indeed, we believe that we can posit such a model. Our model, we believe, offers an excellent starting point for understanding the details of conduction and degradation in these materials and serves to explain not only the optical data presented here, but also the DLCP data presented in Chapter IV.

5.2. Light Trapping Effects

One short study that we performed for nc-Si:H materials deposited by United Solar was to determine the effects of substrate texturing on our optical measurements. It is not uncommon that PV makers will incorporate a textured substrate or roughened junction interfaces in order to promote optical absorption. [83-86] The so-called degree of “light trapping” is a measure of the effective optical path length through the absorber layer of the device. Good light trapping properties are absolutely critical in order to produce a PV device of good optical conversion efficiency.

Researchers at United Solar often promote light trapping by incorporating a thin (~50nm) Ag/ZnO texturing layer in their devices. Such devices have the structure: TCO/p⁺/i- nc-Si:H/n⁺/Ag/ZnO/Stainless Steel. In order to test the effects of this texturing on optical absorption, United Solar asked us to perform some TPI measurements on a pair of these devices that were grown simultaneously. One of the devices was deposited on a n⁺/Ag/ZnO/SS substrate and the other on n⁺/SS. The resulting TPI spectra for these

devices is given in Figure 5.5. The device incorporating the Ag/ZnO texturing layer is denoted as “Textured” and the device lacking this layer is denoted as “Specular”.

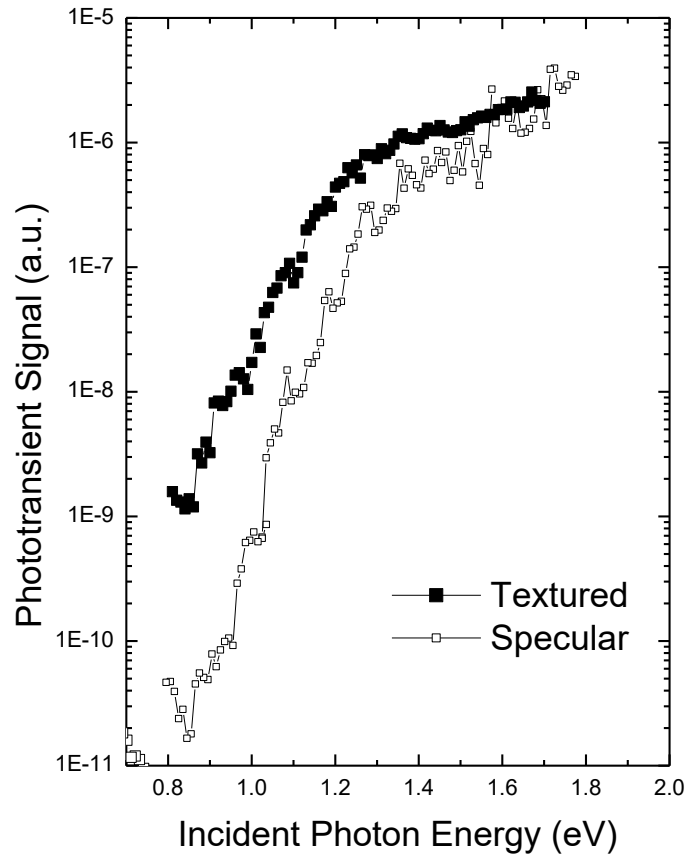


Figure 5.5. The effects of light trapping were investigated in sample 14036 by using transient photocurrent (TPI) measurements. The effect of adding a textured back reflector was to broaden the effective TPI absorption curve.

These spectra, which were aligned at 1.7eV for clarity of presentation, show very different absorptive properties. Namely, the absorption (Urbach) edge of the textured device is much broader than that of the specular device. This result is most likely a convolution of two effects. The first is the geometric light trapping effect caused by the

textured substrate. The second is the nature of the nc-Si:H absorber, which is almost certainly been influenced by the textured substrate. This latter result was a central feature of our DLCP measurements and was discussed in Section 4.1. Therefore, in a way, the result shown in Figure 5.5 reinforces conclusions drawn from DLCP measurements. This data is important in another way, however. For the first time, these spectra show that light trapping effects on IR absorption are detectable using the TPI measurement method.

The ability to image such an effect using standard measurement techniques such as a transmission/reflection (T/R) experiment are dubious at best. Figure 5.6 shows a comparison between a TPI absorption curve which was performed on a standard p-i-n device, and a T/R experiment performed on a device deposited on a transparent glass substrate. The T/R spectrum was taken with the expert aid of J. Russell and J. Tate at Oregon State University. [87] The TPI data have been scaled such that the spectrum provides a measure of the attenuation coefficient, α . These data show 1) the correspondence between TPI and the T/R experiment, and 2) the ability of TPI to image absorption in the IR range where the T/R signal becomes obscured by thin film interference.

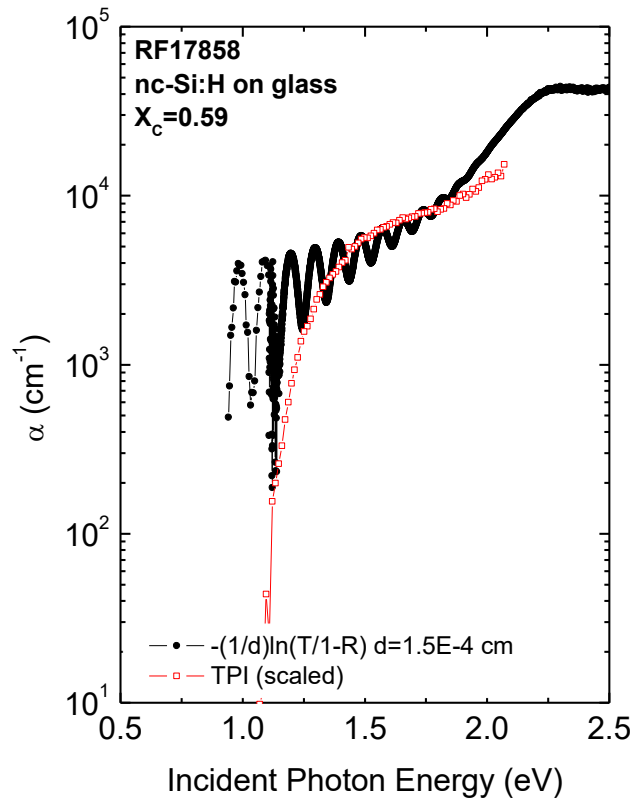


Figure 5.6. The TPI method is well suited to imaging optical absorption over IR wavelengths. These data compare a TPI spectrum with a corresponding transmission/reflection spectrum, which becomes obscured at optical energies below $\sim 1.2\text{eV}$. [87]

One may note that the TPI spectrum tends toward a slope not equal to that of the T/R measurement at optical energies equal to and above 1.75eV . The failure of the spectra shapes to conform to one another in this energy range was most likely caused by small physical differences between the two matched samples used in this study. At such high optical energies, optical penetration depths into the material would be very small, meaning that even a thin layer of detritus on the material surface could have produced the effect.

Also, we have already shown that substrate type can affect the material properties of nc-Si:H. Since these two “matched” samples were indeed deposited on different substrates for practical reasons, the structural properties induced in these materials by substrate choice could also have produced this minor spectral shape difference.

CHAPTER VI

INTERPRETATION AND DISCUSSION

6.1. Interpretation of the Optical Spectra

In Section 5.1 several results of TPC and TPI measurements were discussed for nc-Si:H. Specifically, we recognized the challenge of proposing a set of criteria explaining the wide variety of behaviors seen in these spectra. Here we outline more completely the most likely physical causes of those behaviors.

In Chapter V we discussed a set of criteria necessary for observing a negative TPC signal. But why, in nc-Si:H, do these negative signals appear *both* at optical energies near 0.6eV *and* 1.2eV? In addition, why should this behavior be dependent on the crystalline volume fraction of the devices? We believe that the explanation lies in considering the spatial extent of the grain boundary (GB) regions. Indeed the idea that the thickness of GBs, or regions of otherwise larger bandgap such as amorphous inclusions, crucially influence the electrical properties of nc-Si:H is becoming more prevalent in the literature. [57,88-90] We believe this thickness dependence appears in our TPC spectra as follows.

Figure 6.1 shows optical transitions that might occur between the valence band and empty states of a defect band that resides in the amorphous/GB phase. Both transitions are of the type that may result in a negative TPC signal. Figure 6.1 (left) illustrates a material that contains a lower volume fraction of amorphous component, or otherwise a material wherein the distribution of nanocrystallites is such that the thickness of amorphous

inclusions/GBs⁹ is small. Specifically, the thickness of such regions is comparable to the wavelength of majority carriers. In this case, the energy levels in the amorphous and crystalline phases are likely to be well mixed quantum mechanically (represented by the stippling in the figure). In such a scenario, the energy threshold for the optical transition illustrated in the figure reflects the energy difference between the top of the valence band in the crystallite and the defect energy. Conversely, Figure 6.1(right) shows a situation in which the amorphous region is much thicker, denoted by some authors as a “large grain boundary” or LGB. [57]

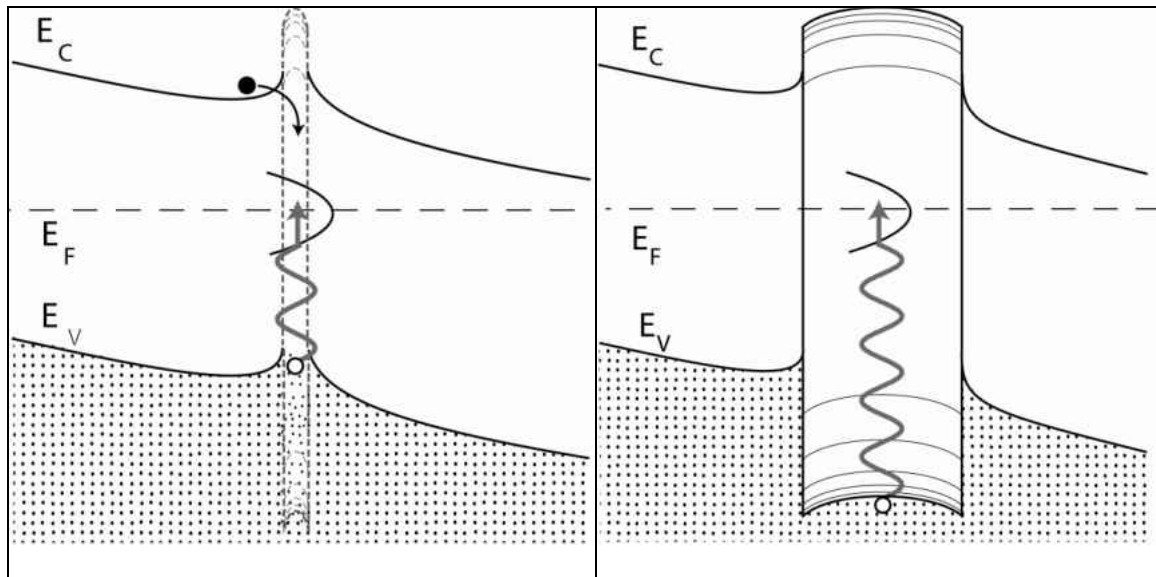


Figure 6.1. We believe tunneling effects involving grain boundaries explain the optical transition energies for more crystalline (left) and more amorphous (right) materials.

In this case, the amorphous region/GB is wider so that the spatial overlap (and corresponding matrix element) between the wavefunction of a carrier in the crystallite valence band and amorphous region valence band states is small. In such a case, the

⁹ The terms “grain boundaries” and “amorphous inclusions” are being used interchangeably because the precise nature of these regions is unknown. All that is important is that such regions have a larger bandgap than the nanocrystallite phase.

transfer into and out of this amorphous region is difficult for holes and electrons alike and the energy threshold for an optical transition would reflect the energy difference between the valence band states in the amorphous phase and the defect level. In comparison to the optical transition from Figure 6.1(left), this second transition energy will be larger by roughly the valence band offset energy between the two phases. Indeed, from the negative TPC signal regimes in Figure 5.3, the difference in thresholds is 0.5 to 0.6eV, a value very close to the valence band offset between crystalline and amorphous silicon as determined by several studies. [91-93] In addition, the individual optical transition energies for the lower and higher crystalline fraction materials (0.6 and 1.2eV, respectively) also agree with the theoretical transition energies illustrated in Figure 6.1. To be clear, Figure 6.1 illustrates optical transitions into a defect situated near the amorphous silicon mid-gap energy. Note that these transition energies agree well with the proposed energetic distribution of defects found using the DLCP method. Note also that the thickness of these GB regions are very likely to play an important role in affecting minority carrier transport. These two features of the data are discussed next.

6.2. Interpretation of Drive Level Capacitance Profiling (DLCP) Results

The optical spectra suggested two primary conclusions: first, that defects responsible for a negative TPC response reside in the amorphous/grain boundary (GB) tissue, a result supported by wavelength dependent light-induced degradation experiments; and second, that the thickness of amorphous/GB inclusions, and therefore the device crystallinity, crucially affect the appearance of the optical spectra. What, if anything, do the results from the DLCP experiments add to this picture?

Results from the DLCP data can be summarized as follows: a large defect response was characteristic of the more *crystalline* materials as shown in Figure 4.1 – in contrast to what might be expected from the Staebler-Wronski Effect. Furthermore, in more amorphous materials, a *decrease* in defect response was witnessed, as shown in Figure 4.3. We believe these results can be modeled using the same picture as shown in Figure 6.1 and that our results lend themselves to two primary interpretations. For each interpretation it is our belief that these effects are describable by considering a set of defects situated near the amorphous component mid-gap with the added stipulation that the transition energy into and out of these defects is a function of their electronic occupation. The two interpretations are as follows.

The first interpretation of the data [94] is illustrated in Figure 6.2. This model shows an amorphous/GB inclusion in the annealed state (Figure 6.2, left) and in the degraded state (Figure 6.2, right). In this interpretation the amorphous/GB inclusion is of such a thickness that carriers can easily conduct into and out of the region, thereby making the mid-gap states “visible” on the timescale of our DLCP measurements (~ 0.1 ms). We make the assumption that defects in this scenario are *negatively charged*, a reasonable assumption given that several electron-spin resonance experiments on similar mixed phase silicon material suggest that such defects indeed are singly-occupied, and negatively charged.

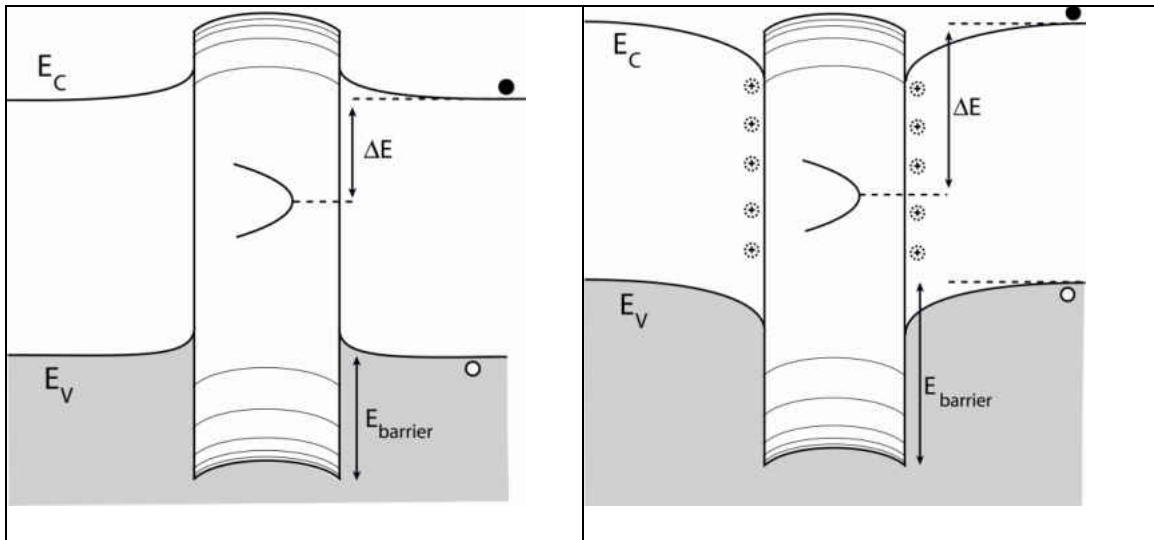


Figure 6.2. Compared to the State A case (left) lightsoaking may produce more negatively charged defects which must be compensated by positive charge which can gather at the grain boundary edges (right), affecting both the band bending and the potential energy difference between the deep defects and the conduction band mobility edge. This effect can explain both the decreases of DLCP density upon lightsoaking and the decreases in minority carrier collection in the degraded state.

To compensate this negative charge, positive charge gathers in the neighborhood of the defects, affecting the band bending in this region. As more D^- states are produced upon lightsoaking, the density of defects increase, the Fermi level becomes pinned to the defect level, and additional positive charge surrounds the GB effectively shifting the potential of the amorphous/GB inclusion with respect to the neutral bulk potential. This shift would occur in a fashion theoretically predicted by Equation 1.9. This energy shift *increases* the transition energy of bulk majority carriers into and out of the defect thereby increasing the timescale for the transition and therefore producing a drive level profile of suppressed magnitude.

This picture accounts for a *decrease* of DLCP density upon lightsoaking by

suggesting that the transition energy into and out of these defects is affected by the metastable band bending conditions in the neighborhood of the amorphous/GB regions. At the same time, this picture suggests that more defects are visible in materials of higher crystalline volume fraction because materials possessing large grain boundaries (LGBs) do not allow sufficient conduction of carriers into and out of these regions. Finally, this picture accounts for metastable decreases in minority carrier collection upon lightsoaking since the formation of a positive “screening charge” in the neighborhood of the GBs induces a large potential barrier for hole transport in the conduction band, as illustrated.

Altogether, we find this model for conduction and degradation in nc-Si:H very appealing. Indeed, this picture may be true for a large variety of nc-Si:H material, save for two experimental facts. First, even though we can experimentally increase the maximum energy depth, E_e , for the DLCP experiment, no large defect response (i.e. that of Figure 4.2 top left) was *ever* observed in materials of large amorphous fraction. This means that either measurement of the full defect density under the conditions illustrated in Figure 6.2 (right) was experimentally impossible, suggesting that the model of Figure 6.2 is valid, or that this large DLCP response, which is so typical for materials of large crystalline fraction, is caused by something *other than* defects situated in amorphous/GB regions. Indeed, the extensive modeling which was performed on a subset of nc-Si:H materials suggests that just such a picture is possible.

During the modeling attempts for materials of crystalline fraction near 0.65 (see Appendix) we found that the large defect response in the light-degraded state could only be reproduced by allowing the mid-gap amorphous/GB defect, originally occurring at an energy of $E_C-0.7\text{eV}$ in the annealed state, to *decrease* to a transition energy depth of E_C-

0.56eV in a metastable fashion upon lightsoaking. In other words, the large increase in DLCP density in State B was attributed to a defect that *appeared* to have a decreased transition energy. This seems completely at odds with the model of Figure 6.2 which depends on the idea that the State B defects become *deeper* with respect to the neutral bulk conduction band, nonetheless, we believe a solution to this apparent conflict exists.

Consider, for example, Figure 6.3.

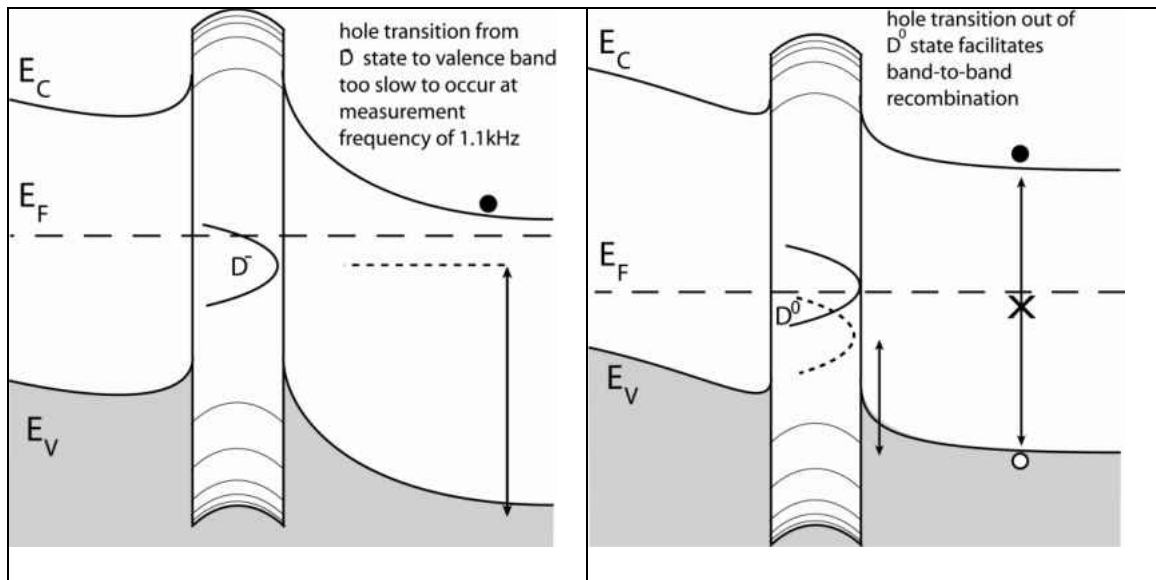


Figure 6.3. Under this model, the large DLCP signal in State B indicates band-to-band recombination (right) that occurs with an activation energy of half the crystallite bandgap, roughly 0.55eV. This could appear as a defect of energy 0.55eV in the DLCP measurement. In State A (left) holes occupying D- defects are too deep to emit to the valence band at the measurement frequency of 1100Hz.

In Figure 6.3 are shown the annealed state (Figure 6.3, left) and the degraded state (Figure 6.3, right). Just as before, upon lightsoaking the Fermi level becomes pinned to the defect, the density of defects increase, and the potential energy of defect located in the amorphous/GB region becomes deeper with respect to the bulk conduction band edge – once again providing a large barrier to hole transport in the degraded state. However, in this

picture an additional kind of defect is produced in State B – a neutral D^0 defect.

In State A, we believe that a hole captured into a D^- defect – thus becoming a neutrally charged D^0 state - may be too tightly bound to emit to the valence band at the 1100Hz timescale of the DLCP measurement. However in State B, the capture of a hole into a D^0 defect – thus forming a positively charge D^+ state - is energetically closer to the valence band edge and so allows a more rapid reemission of the hole to the valence band (Figure 6.3, right). In such a scenario, the density of holes in the crystallites could then follow the 1100Hz oscillation. However, if this hole density was rate limited not by the 1100Hz driving oscillatory voltage, but by band-to-band carrier recombination, then this entire process would be dominated by a transition energy of exactly half the nanocrystallite bandgap. Therefore if the nanocrystallite bandgap is 1.12eV, then this transition energy would be 0.56eV – a value nearly identical to the 0.57eV that emerged from our modeling attempts.

In summary, our data suggest two physical interpretations of the electronic behavior of nc-Si:H. These interpretations are distinct, but not mutually exclusive. Both pictures suggest defects present in amorphous/GB regions of nc-Si:H which lie at an energy about 0.7eV below the amorphous/GB region conduction band edge, or about 0.7eV below the nanocrystallite band edge. Both pictures also suggest a metastable potential shift upon lightsoaking in the energy of these defects in reference to the bulk conduction band mobility edge and in both cases this potential shift creates a barrier to hole transport. The difference between the interpretations lies in how they account for the enhanced lightsoaked state (State B) DLCP response in materials of crystallite fraction at or above

60vol%. Specifically, one model suggests that this DLCP response is merely suppressed in high amorphous fraction materials because carrier mobilities in the amorphous phase are low and therefore transitions into and out of these defects in the more highly amorphous materials responds too slowly to be visible in our measurements. The other model suggests that the presence of crystallites themselves drive this enhanced DLCP response and that the physical effect causing this particular DLCP behavior is actually the recombination and emission of carriers rate-limited by an energy half of the crystalline silicon bandgap, $\sim 0.56\text{eV}$.

These interpretations, which have been proposed here for the first time, are certainly open to debate. Scientifically, however, one must ask if there is any possible way to experimentally distinguish which interpretation may be correct (if either!). Some further discussion of this topic, along with a general summary of the entirety of this work, is offered in the next, and final chapter.

CHAPTER VII

SUMMARY AND CONCLUSIONS

Hydrogenated nanocrystalline silicon is an important semiconductor material because it has shown great promise as a thin film photovoltaic. However, since nc-Si:H is a mixture of both crystalline and amorphous silicon phases, its electrical properties, and the structure/function relationships governing these properties are complex and very hard to understand. In this study we investigated the structural properties of this material using methods such as Raman spectroscopy and transmission electron microscopy, we examined the compositional properties using TOF-SIMS measurements, and characterized the electrical properties using a set of junction-capacitance based measurements.

Our work is unique because very few laboratories are able to perform the junction-capacitance measurements we employ. These measurements include the drive level capacitance profiling (DLCP) technique, transient photocapacitance (TPC) and transient photocurrent (TPI) measurements. These measurements are very useful because they can provide direct measurements of the density of states distribution in the band-gap and can also provide information on majority and minority carrier transport properties.

Our primary results in this study can be summarized as follows. Crystallinity in these devices was shown to be highly sensitive to growth conditions including the substrate type and texture. We also saw that the presence of oxygen was highly dependent on the device crystallinity, with more crystalline devices containing higher densities of oxygen. Moreover, we saw that both the crystallinity and the oxygen content correlated well with the presence of deep gap states located at 0.7eV below the conduction band. Our

measurements indicate that this defect is located in amorphous-like grain boundary regions in these materials. In addition, we identified a second deep defect of energy 0.4eV below the conduction band that appeared to exist only near the p/i junction interface. This defect resulted in a “dip” in the drive level profiles. The spatial extent of this 0.4eV defect was found to be constrained to within 0.3 μ m of the p/i interface for the samples investigated.

Metastable changes in nc-Si:H upon lightsoaking seemed complex, but our measurements and careful modeling of some measurement results yielded information that have produced a couple of reasonable models that account for the primary features of light-induced degradation in nc-Si:H. These primary features include: a universal decrease in minority carrier collection efficiency in the light-degraded state, deep defects that appear at optical transition energies of both 0.6eV and 1.2eV for more crystalline and more amorphous devices, respectively; the occasional *decrease* in DLCP density for more amorphous devices, and a large apparent defect density in highly crystalline devices in the light-degraded state which exhibit electronic transition energies near 0.55eV. Our models, which are discussed in the previous sections of this chapter, can be succinctly summarized as interpretations that rely on the potential shift of grain-boundary regions with respect to the bulk potential as the charge state of the identified 0.7eV defect alters upon lightsoaking or temperature changes. We believe these potential shifts explain well the salient features of our data. Furthermore, we believe that these models can be further tested by sets of experiments that we describe next.

7.1. Ideas for Future Experiments

A physical model isn't much good if it can't be tested. In Sections 6.1 and 6.2 we proposed a couple of models that we believe help explain the electrical properties of nc-Si:H. In this section we consider a set of measurements that might test the validity of these models.

First of all, these measurements should be repeated on additional sets of samples. Particularly, the negative TPC optical transitions discussed in Section 5.1 should be verified on additional sets of material.

Secondly, the models we propose assume band bending in the neighborhood of grain boundaries that results from compensating positive charge gathering around regions of negatively charged defects. The charge states of mid-gap defects in purely amorphous materials has been studied thoroughly using techniques such as electron spin resonance (ESR) in which the occupancy (net electronic spin) of electronic gap states can be directly measured.. Such measurements could be performed on these materials to verify that the occupancy of gap states reflects the charge states we propose.

Thirdly, techniques do exist that can measure the potential distributions in conductors directly. Kelvin probe force microscopy (KPFM) is a technique that can spatially resolve the work function of a material surface on an atomic-length scale. Such a method might be able to detect potential fluctuations within nc-Si:H directly.

In addition to these measurements, there are many other tests and verifications that could be performed. These include additional EELS and TEM measurements to verify the presence of oxygen at grain boundaries, time-of-flight measurements to investigate metastable changes to minority carrier conduction and the spatially-dependent conduction

mechanisms discussed in Section 4.3, and even the special preparation of a-Si:H/c-Si superlattice structures to verify the tunneling mechanisms we have discussed. The latter experiment would allow the investigation of band bending at specially prepared a-Si:H/c-Si interfaces.

APPENDIX A

DETAILS ON THE MODELING OF DLCP DATA

This appendix offers additional details on the portion of this project concerned with modeling drive level profiles. At a certain point during this research project, our collaborators began to supply us with nc-Si:H samples that were much thicker than the original sample sets. This allowed us to see additional structure in the drive level profiles that were much more complex than more nominal DLCP data. We set about modeling these profiles and more details about this modeling process are given here.

Modeling was performed using a program that was developed Dr. J. D. Cohen to treat the dynamic response of an arbitrary spatial variation of electronic properties to an oscillatory voltage (see Chapter VI of [95]) The basic functionality of this program is described as follows. The numerical simulation solves the Poisson equation for a small oscillatory voltage, δV at a nominal dc bias. The value of δV is then incremented and Poisson's equation is re-solved. This analysis, which involves an integration over the entire depletion region, results in a simulated measurement of C_0 and C_1 as described in Chapter II of this dissertation. The behavior of this response with changes in temperature and frequency is incorporated by defining a time limit for the release of charge from gap states. The dc bias value is then changed and the process is repeated. Therefore, the numeric simulation relies on: Poisson's equation, the legitimacy of $\delta Q/\delta V$ as a measurement of capacitance, and the application of an emission time limit to deduce the deep state response of a simulated distribution of gap states. In its current form, the program divides the

semiconductor absorber layer into three spatial regions takes the input parameters: 1) temperature and measurement frequency; 2) bandgap and Urbach energy of the majority carrier band edge; 3) thermal emission cutoff energy, E_e ; 4) the positions of the two boundaries separating the three spatial regions; 5) the characteristic mixing width of the boundaries in 4); 6) the simulated sample area; and, 7) the simulated dc bias range and bias increment value. For each individual spatial region the input parameters are: 1) the shallow donor density; and, 2) the energy depth, width, and integrated density of a gaussian deep defect band.

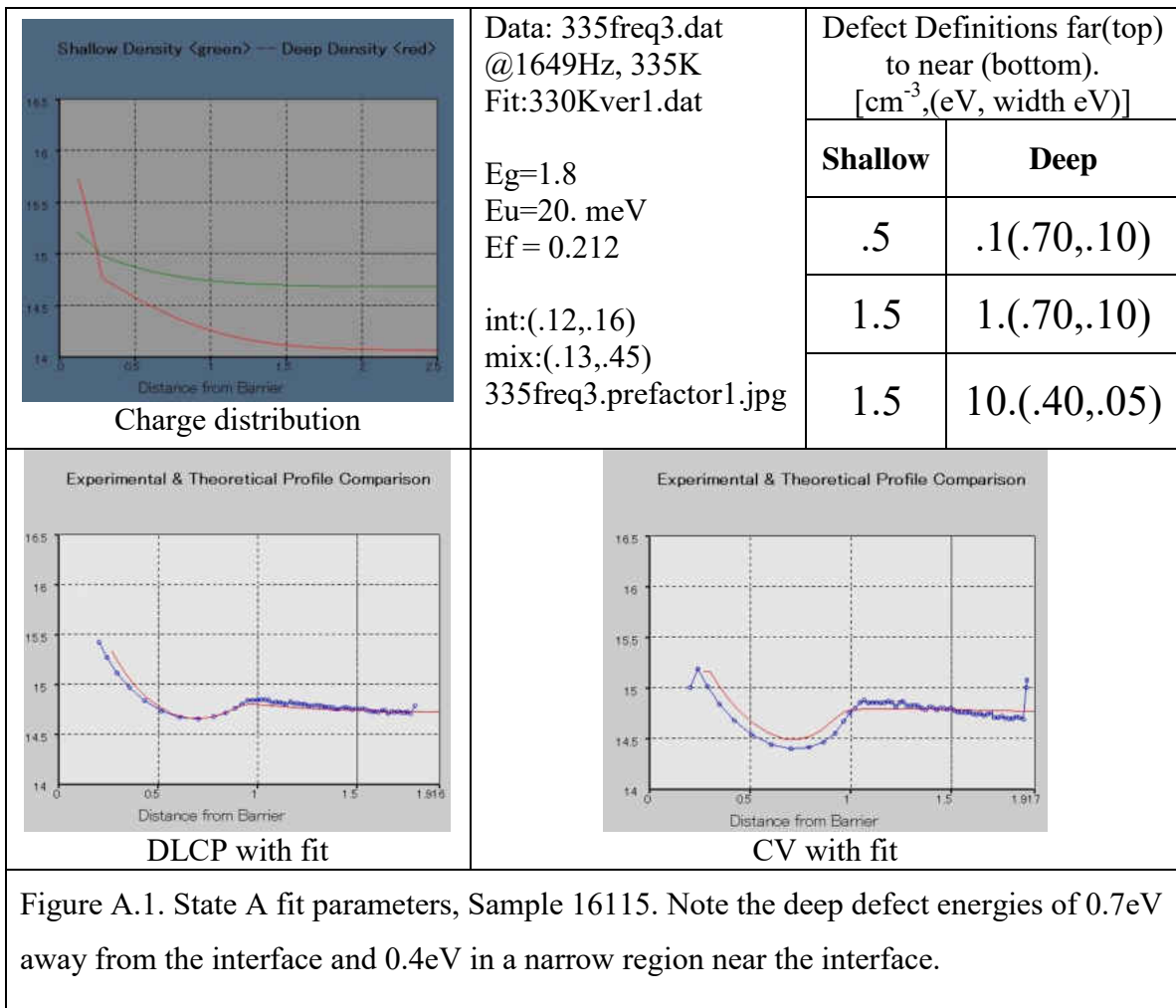
Insofar as the above parameters define an arbitrary set of electronic properties, and to within the numeric capabilities of the simulation, the program is able to output a simulated DLCP and CV experiment. This technique is extremely helpful for “backing out” the actual electronic properties described by a DLCP experiment which in itself may be non-intuitive. An example of just such a case is given next.

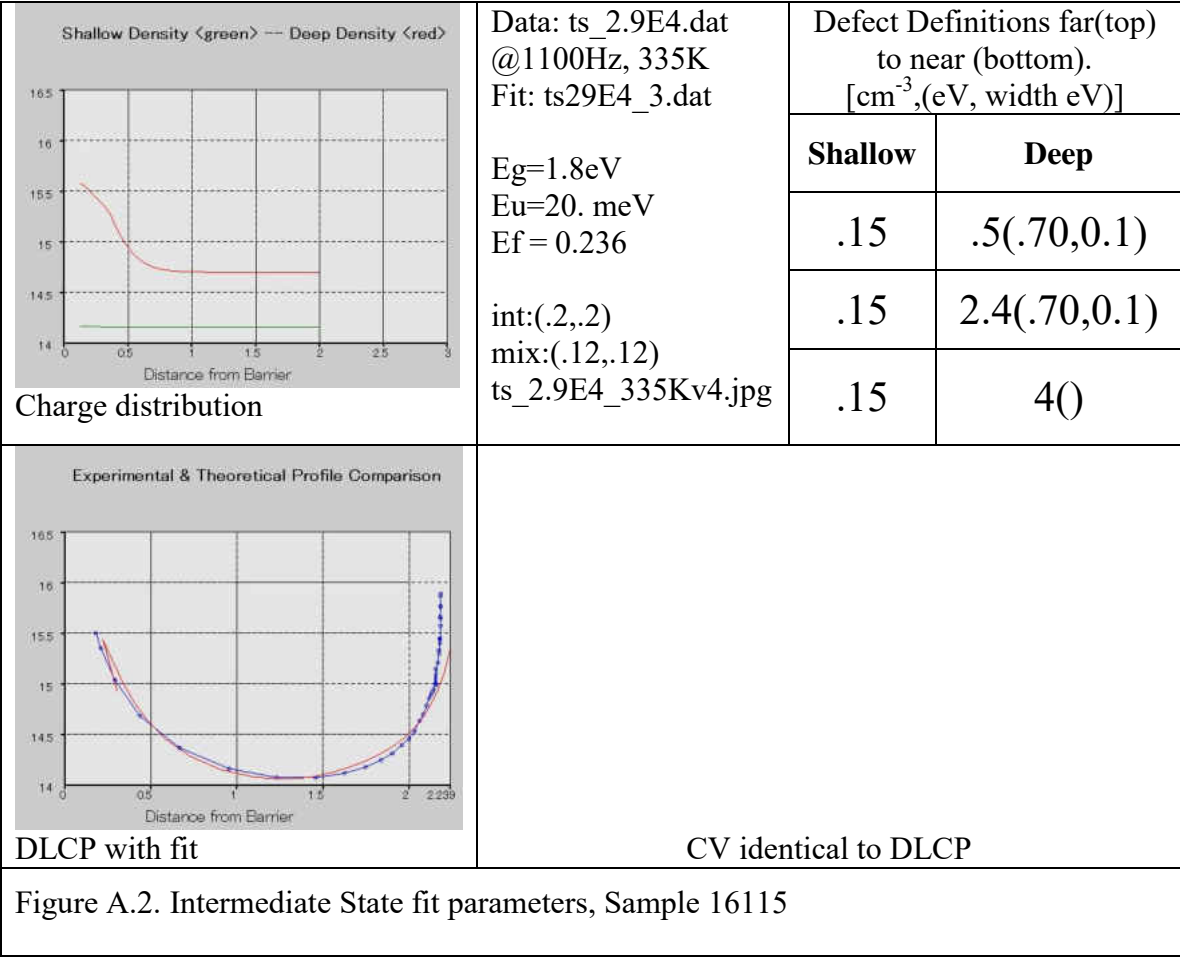
A.1. Modeling Results for Sample 16115

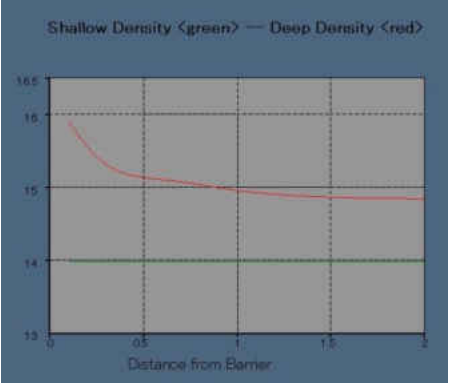
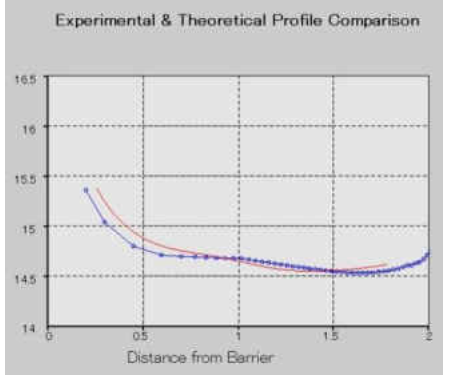
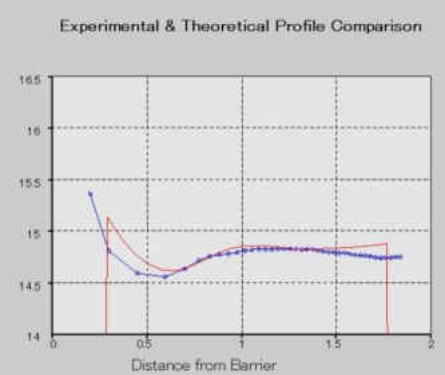
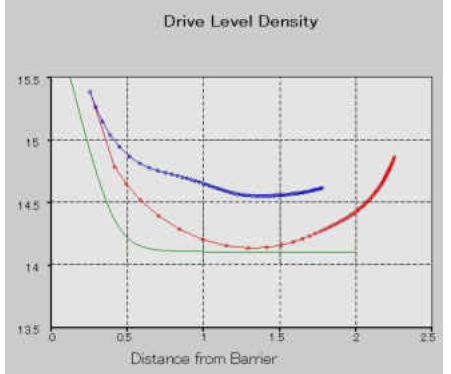
The following spreadsheets give detailed fitting parameter information for three fits to DLCP data for sample 16115. Shown in each case are shallow/deep charge distributions as output by the fitting program (top left), detailed fitting parameters and relevant filenames (top right), best fit to DLCP data (lower left; data shown in blue, modeled fit shown in red), and best fit to corresponding CV data (lower right; data shown in blue, modeled fit shown in red). NOTE: for the table entitled “Defect Definitions”, user defined defect densities are listed for the three spatial regions defined by the program. The top row gives defect information for the spatial region *far* from the interface, the middle row is the *middle*

spatial region, and the bottom row is the *near* spatial region. “Shallow” density definitions are density only, and “Deep” density definitions are of the form: *density (energy depth, distribution width)*. Where all densities are in units of 10^{15} cm^{-3} , and energy depths and widths are in eV. “Int” refers to the positions of the interfaces between the three spatial regions, given in microns. “Mix” refers to the mix widths between the spatial regions. The given .jpg filename refers to the DLCP best fit image shown in the bottom left of the table.

In the State B data, an additional graphic is shown showing the temperature dependence of the modeled data.





 <p>Charge distribution</p>	<p>Data: xvsNdStB @1100Hz, 335K Fit:SB335iT9.dat (.53 Ee) Fit:SB335iT7.dat (.48eV) Eg=1.15 Eu=23. meV Ef = 0.284</p> <p>int:(.14,.7) mix:(.1,.45) SbiT7 Nd.jpg</p>	<table border="1"> <thead> <tr> <th colspan="2">Defect Definitions far(top) to near (bottom). [cm⁻³,(eV, width eV)]</th> </tr> <tr> <th>Shallow</th> <th>Deep</th> </tr> </thead> <tbody> <tr> <td>.1</td> <td>1.8(.59,.05)</td> </tr> <tr> <td>.1</td> <td>2.5(.57,.04)</td> </tr> <tr> <td>.1</td> <td>10.(.48,.01)</td> </tr> </tbody> </table>	Defect Definitions far(top) to near (bottom). [cm ⁻³ ,(eV, width eV)]		Shallow	Deep	.1	1.8(.59,.05)	.1	2.5(.57,.04)	.1	10.(.48,.01)
Defect Definitions far(top) to near (bottom). [cm ⁻³ ,(eV, width eV)]												
Shallow	Deep											
.1	1.8(.59,.05)											
.1	2.5(.57,.04)											
.1	10.(.48,.01)											
 <p>DLCP with fit</p>	 <p>CV with fit</p>											
 <p>Temperature Dependence: StBiT7b_.525_.48eV.jpeg</p>		<p>Figure A.3. State B fit parameters, Sample 16115. Note the energy shifts of the deep defects. The 0.7eV defect has become ~0.58eV and the near-interface defect has become 0.48eV. The deeper defect has an uncertainty of 0.05eV and the shallower defect has an uncertainty of 0.1eV.</p>										

APPENDIX B

DEVICE PREPARATION AND APPLICATIONS

This study concerns the electronic and optical properties of hydrogenated nanocrystalline silicon (nc-Si:H). United Solar Ovonic, LLC in Troy, Michigan, deposited all of these films.

B.1. Growth Methods and Sample Geometry

Unless otherwise specified, all samples were deposited in a StainlessSteel/n+/i/p+/ITO geometry using a modified very high frequency (modified VHF) plasma enhanced chemical vapor deposition (PECVD) process. In general, PECVD depositions involve the plasma decomposition of a source gas as it flows between two parallel plate electrodes which carry an alternating voltage of several hundred volts at a frequency of 13.56 MHz, in the case of VHF depositions. The positively charged plasma is then attracted to a negatively charged substrate onto which the film becomes deposited.

For the deposition of these particular nc-Si:H films, the source gas was a mixture of silane (SiH_4) and disilane (Si_2H_6), where Si_2H_6 was used as a hydrogen diluting agent. By carefully controlling the Si_2H_6 flow during deposition the hydrogen content throughout the film could be controlled. The top contact, indium tin oxide (ITO), was a semi-transparent conducting contact usually of area 0.05cm^2 . In cases in which nc-Si:H films were tested in a near-optimal geometry, an additional scattering layer was included near the stainless steel (SS) substrate to facilitate light trapping. In these cases the device structures were:

SS/Ag/ZnO/n+/i/p+/ITO, as shown in Figure B.1. The astute reader will also notice that the VHF process used in the preparation of these films is “modified”. The details of this modification are considered proprietary¹⁰, but do not constitute a substantial departure from the process outlined above.

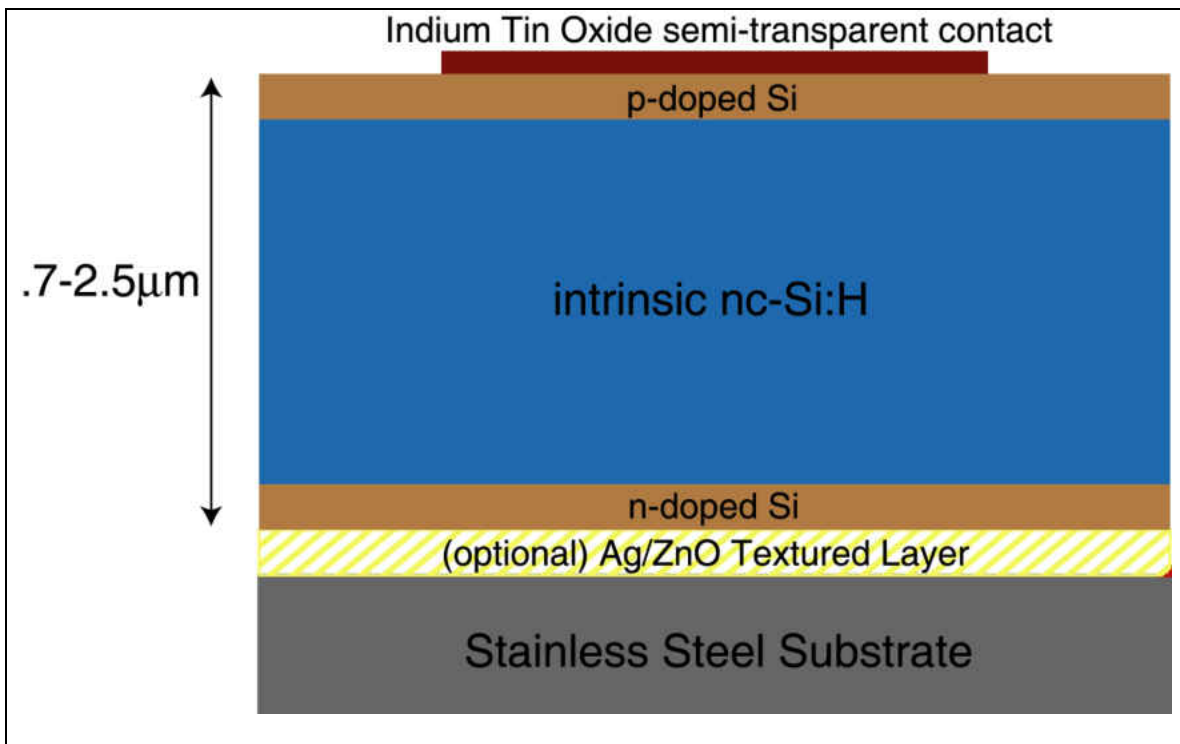


Figure B.1. Sample structures were a very straightforward p-i-n configuration set atop a stainless steel specular back-reflector. Sometimes an Ag/ZnO textured back reflector was added to the device in order to facilitate light-trapping. Measurements on devices using such a back reflector are cited in the text. One result of this study was that such textured layers do indeed influence crystallite growth in these materials, which in turn influenced deep defect densities. Of course, light would be incident onto this device from the semi-transparent contact side.

Indeed, although the PECVD process is simple in principle, in practice it is a highly detailed procedure where many factors must be controlled to produce high quality films.

¹⁰ Clarification comes from one United Solar staff scientist who says: the MVHF process results when “we take the regular VHF process and change it a little bit”

Important deposition parameters include gas flow rate, gas pressure (which specifies mean collision times between gas molecules), VHF power, substrate temperature, and gas composition, naturally. Any deposition process may also include more radical modifications or embellishments to include UV-assisted plasma decomposition, post deposition annealing or post deposition laser-induced crystallization, detailed substrate temperature control, and any of a host of other possibilities.

B.2. Purpose of the Devices

These nc-Si:H films were part of a study directed at studying fundamental material properties of nc-Si:H in order to increase deposition rates and material quality for incorporation of nc-Si:H as a narrow-gap component of a-Si:H based tandem cells at United Solar. The tandem cells utilizing nc-Si:H have the overall structure a-Si:H/a-SiGe:H/nc-Si:H and are true optically thin films with conversion efficiencies approaching 15%. [96] Because of their thin, amorphous structure these devices are rather flexible. This flexibility means that these multi-junction cells are currently incorporated in some very interesting applications including solar laminates. These laminates are essentially large rolls of “solar cell carpet” that can be unrolled and secured to a sunlit surface, greatly easing the cost and labor of installation. Another application United Solar has found for these multi-junction structures are solar shingles, an architecturally understated approach to incorporating photovoltaics into building structures. Other manufacturers of flexible thin film photovoltaics have suggested applications such as portable PV mats that can be unrolled and utilized “in the field”, and even clothing that incorporates PV arrays. Most agree that the fashion potential of the latter is shocking, at best. It is this author’s opinion,

however, that the primary benefit flexible thin film PV technology is the decreased transport and installation cost of solar modules that are non-fragile and easily deployable.

REFERENCES CITED

- [1] N. W. Ashcroft and N. D. Mermin, "Solid State Physics." (Thompson Learning, 1976).
- [2] W. H. Zachariasen, J. of the Am. Chem. Soc. **54**, 3841 (1932).
- [3] N. F. Mott, Philo. Mag. **19**, 835 (1969).
- [4] D. Weaire and M. F. Thorpe, Phys. Rev. B. **4**, 2508 (1971).
- [5] J. D. Joannopoulos and M. L. Cohen, Physical Review B **7**, 2644 (1973).
- [6] J. M. Ziman, "Models of disorder." (Cambridge University Press, Oxford, 1979).
- [7] L. D. Landau and E. M. Lifshitz, "Electrodynamics of continuous media." (Pergamon, Oxford, 1960).
- [8] A. Y. Shik, "Electronic properties of inhomogenous semiconductors." *Electrocomponent science monographs*. (Gordon and Breach, Luxembourg, 1995).
- [9] J. Volger, Phys. Rev. **79**, 1023 (1950).
- [10] G. H. Blount, R. H. Bube and A. L. Robinson, J. Appl. Phys. (1970).
- [11] W. E. Taylor, Physical Review **88**, 867 (1952).
- [12] R. Zallen and S. Harvey, Phys. Rev. B. **4**, 4471 (1971).
- [13] S. Kirkpatrick, Reviews of Modern Physics **45**, 574 (1973).
- [14] S. Guha, X. Xu, J. Yang and A. Banerjee, Applied Physics Letters **66**, 595 (1995).
- [15] H. Keppner, J. Meier, P. Torres, D. Fischer and A. Shah, Applied Physics A **69**, 169 (1999).
- [16] B. Yan, G. Yue, J. Yang, A. Banerjee and S. Guha, Mat. Res. Soc. Symp. Proc. **762**, A4.1.1 (2003).
- [17] R. E. I. Schropp, H. Li, R. H. Franken, J. K. Rath, C. H. M. van der Werf, M. A. Schuttauf and R. L. Stolk, Thin Solid Films **516**, 6818 (2008).

- [18] B. Yan, G. Yue, J. M. Owens, J. Yang and S. Guha, in *IEEE 4th World Conf. on Photovoltaic Energy Conversion* (Hawaii, USA, 2006), pp. 1477.
- [19] A. M. Goodman, *Journal of Applied Physics* **34**, 329 (1963).
- [20] D. L. Losee, *Jour. App. Phys.* **46**, 2204 (1975).
- [21] S. M. Sze, "Semiconductor Devices." (John Wiley and Sons, New York, 1985).
- [22] D. V. Lang, *Physical Review B* **25**, 5285 (1982).
- [23] J. D. Cohen and D. V. Lang, *Phys. Rev. B* **25**, 5321 (1982).
- [24] R. A. Street, "Hydrogenated amorphous silicon." *Cambridge solid state science series.* (Cambridge University Press, Cambridge, 1991).
- [25] A. Yelon, *Physical Review Letters* **65**, 618 (1990).
- [26] J. C. Dyre, *Journal of Physics C: Solid State Physics* **19**, 5655 (1986).
- [27] J. T. Heath, J. D. Cohen and W. N. Shafarman, *Journal of Applied Physics* **95**, 1000 (2004).
- [28] C. E. Michelson, A. V. Gelatos and J. D. Cohen, *Applied Physics Letters* **47**, 412 (1985).
- [29] W. B. Jackson, N. M. Amer, A. C. Boccara and D. Fournier, *Applied Optics* **20**, 1333 (1981).
- [30] M. Vanecek, J. Kocka, A. Poruba and A. Fejfar, *Journal of Applied Physics* **78**, 6203 (1995).
- [31] D. V. Lang, *J. Appl. Phys.* **45**, 3023 (1974).
- [32] D. V. Lang, in *Topics in applied physics*, edited by P. Bräunlich (Springer, Berlin, 1979), Vol. 37, pp. 93.
- [33] W. B. Jackson, *Physical Review B* **31**, 5187 (1985).
- [34] J. T. Heath, Ph.D. Thesis (2002).
- [35] J. D. Cohen, J. T. Heath and W. N. Shafarman, in *Wide-Gap Chalcopyrites*, edited by Susanne Siebentritt and Uwe Rau (Springer, Berlin, 2006), pp. 69.

- [36] P. Hugger, J. D. Cohen, B. Yan, J. Yang and S. Guha, *Philosophical Magazine* **89**, 2541 (2009).
- [37] N. B. Colthup, L. H. Daly and S. E. Wiberley, "Introduction to Infrared and Raman Spectroscopy." Third ed. (Academic Press, 1990).
- [38] G. Viera, S. Huet and L. Boufendi, *Journal of Applied Physics* **90**, 4175 (2001).
- [39] E. Bustarret, M. A. Hachicha and M. Brunel, *Applied Physics Letters* **52**, 1675 (1988).
- [40] D. Han, J. D. Lorentzen, J. Weinberg-Wolf, L. E. McNeil and Q. Wang, *Journal of Applied Physics* **94**, 2930 (2003).
- [41] A. Matsuda, *Thin Solid Films* **337**, 1 (1999).
- [42] C. W. Teplin, C. S. Jiang, P. Stradins and H. M. Branz, *Applied Physics Letters* **92**, 093114 (2008).
- [43] L. Houben, M. Luysberg, P. Hapke, R. Carius, F. Finger and H. Wagner, *Philosophical Magazine A* **77**, 1447 (1998).
- [44] Y. Baojie, Y. Guozhen, Y. Jeffrey, G. Subhendu, D. L. Williamson, H. Daxing and J. Chun-Sheng, *Applied Physics Letters* **85**, 1955 (2004).
- [45] H. Keppner, J. Meier, P. Torres, D. Fischer and A. Shah, *Applied Physics a-Materials Science & Processing* **69**, 169 (1999).
- [46] U. Kroll, J. Meier, P. Torres, J. Pohl and A. Shah, *Journal of Non-Crystalline Solids* **227-230**, 68 (1998).
- [47] C. C. Tsai, G. B. Anderson, R. Thompson and B. Wacker, *Journal of Non-Crystalline Solids* **114**, 151 (1989).
- [48] R. W. Collins, **364**, 129 (2000).
- [49] S. Guha and J. Yang, *Amorphous and Nanocrystalline Semiconductors - Science and Technology* **352**, 1917 (2006).
- [50] S. Guha, J. Yang, A. Banerjee, Y. Baojie and K. Lord, *Critical review of amorphous and microcrystalline silicon materials and solar cells* **78**, 329 (2003).
- [51] O. Vetterl, F. Finger, R. Carius, P. Hapke, L. Houben, O. Kluth, A. Lambertz, A. Mück, B. Rech, and H. Wagner, *Solar Energy Materials and Solar Cells* **62**, 97 (2000).

- [52] M. Kondo, *Solar Energy Materials and Solar Cells* **78**, 543 (2003).
- [53] Y. Nasuno, M. Kondo and A. Matsuda, in *Proc. of 28th IEEE PVSC* (IEEE, Anchorage, Alaska, 2000), pp. 142.
- [54] S. Guha, J. Yang, D. L. Williamson, Y. Lubianiker, J. D. Cohen and A. H. Mahan, *Appl. Phys. Lett.* **74**, 1860 (1999).
- [55] A. A. Langford, M. L. Fleet, B. P. Nelson, W. A. Lanford and N. Maley, *Physical Review B* **45**, 13367 (1992).
- [56] C. E. Michelson and J. D. Cohen, *Physical Review B* **41**, 1529 (1989).
- [57] J. Kocka, H. Stuchlikova, M. Ledinsky, J. Stuchlik, T. Mates and A. Fejfar, *Solar Energy Materials and Solar Cells* **93**, 1444 (2009).
- [58] L. C. Kimerling and J. L. Benton, *Applied Physics Letters* **39**, 410 (1981).
- [59] R. Murray, *Physica B: Condensed Matter* **170**, 115 (1991).
- [60] R. S. Crandall, *Physical Review B* **24**, 7457 (1981).
- [61] H. Curtis and S. Veprek, *Solid State Communications* **57**, 215 (1986).
- [62] F. Finger, J. Muller, C. Malten, R. Carius and H. Wagner, *Journal of Non-Crystalline Solids* **266-269**, 511 (2000).
- [63] T. Kamei, T. Wada and A. Matsuda, in *MRS Symp. Proc.* (2001).
- [64] D. L. Staebler and C. R. Wronski, *Applied Physics Letters* **31**, 292 (1977).
- [65] V. Dalal and P. Sharma, *Appl. Phys. Lett.* **86**, 103510 (2005).
- [66] J. D. Fields, C. Taylor, D. Bobela, B. Yan and G. Yue, *Mat. Res. Soc. Symp. Proc.* **1245**, A13.01 (2010).
- [67] K. Winer and L. Ley, *Physical Review B* **37**, 8363 (1988).
- [68] G. Lucovsky and S. Y. Lin, *AIP Conf. Proc.* **120**, 55 (1984).
- [69] I. Balberg, R. Naidis, L. F. Fonseca, S. Z. Weisz, J. P. Conde, P. Alpuim and V. Chu, *Phys. Rev. B.* **63**, 113201 (2001).
- [70] C. E. Michelson, *Physical Review B* **41**, 1529 (1990).

- [71] M. Stutzmann, *Physical Review B* **32**, 23 (1984).
- [72] J. Woerdenweber, T. Merdzhanova, R. Schmitz, A. Muck, U. Zastrow, L. Niessen, A. Gordijn, R. Carius, W. Beyer, H. Stiebig, and U. Rau, *Journal of Applied Physics* **104**, 094507 (2008).
- [73] R. E. I. Schropp, P. F. A. Alkemade and J. K. Rath, *Solar Energy Materials and Solar Cells* **65**, 541 (2001).
- [74] R. E. I. Schropp, *Thin Solid Films* **451-452**, 455 (2004).
- [75] J. D. Cohen, C. E. Michelson and J. P. Harbison, in *Disordered Semiconductors*, edited by M.A. Kastner, G.A. Thomas, and S. R. Ovshinsky (Plenum Publishing Corp., 1987).
- [76] P. T. Erslev, J. Lee, W. N. Shafarman and J. D. Cohen, *Thin Solid Films* **517**, 2277 (2009).
- [77] B. Yan, G. Yue, J. M. Owens, J. Yang and S. Guha, *Appl. Phys. Lett.* **85**, 1925 (2004).
- [78] A. F. Halverson, J. J. Gutierrez, J. D. Cohen, B. Yan, J. Yang and S. Guha, *Applied Physics Letters* **88**, 071920 (2006).
- [79] M. Vanecek, A. Poruba, Z. Remes, N. Beck and M. Nesladek, *Journal of Non-Crystalline Solids* **227-230**, 967 (1998).
- [80] T. Unold, J. Hautala and J. D. Cohen, *Physical Review B* **50**, 16985 (1994).
- [81] A. V. Gelatos, K. K. Mahavadi, J. D. Cohen and J. P. Harbison, *Applied Physics Letters* **53**, 403 (1988).
- [82] J. D. Cohen, T. Unold, A. Gelatos and C. M. Fortmann, *Journal of Non-Crystalline Solids* **141**, 142 (1992).
- [83] J. Mueller, B. Rech, J. Springer and M. Vanecek, *Thin Film PV* **77**, 917 (2004).
- [84] R. Biswas and D. Zhou, *Physica Status Solidi* **207**, 667 (2010).
- [85] R. Biswas, J. Bhattacharya, B. Lewis, N. Chakravarty and V. Dalal, *Solar Energy Materials and Solar Cells* **94**, 2337 (2010).
- [86] S. Pillai, K. R. Catchpole, T. Trupke and M. A. Green, *Jour. App. Phys.* **101**, 093105 (2007).

- [87] J. Russell and J. Tate, Private communication (2009).
- [88] J. Koc(ka, A. Fejfar, P. Fojtik, K. Luterova, I. Pelant, B. Rezek, H. Stuchlikova, J. Stuchlik, and V. Svrcek, *Solar Energy Materials and Solar Cells* **66**, 61 (2000).
- [89] J. Koc(ka, T. Mates, H. Stuchlikova, J. Stuchlik and A. Fejfar, *Thin Solid Films* **501**, 107 (2005).
- [90] Y. L. He, G. Y. Hu, M. B. Yu, M. Liu, J. L. Wang and G. Y. Xu, *Physical Review B* **59**, 15352 (1997).
- [91] J. M. Essick and J. D. Cohen, *Applied Physics Letters* **55**, 1232 (1989).
- [92] S. Gall, R. Hirschauer, M. Kolter and D. Braunig, *Solar Energy Materials and Solar Cells* **49**, 157 (1997).
- [93] J. P. Kleider, A. S. Gudovskikh and P. R. i. Cabarrocas, *Applied Physics Letters* **92**, 162101 (2008).
- [94] P. G. Hugger, S. Datta, P. T. Erslev, G. Yue, G. Ganguly, B. Yan, J. Yang, S. Guha, and J. D. Cohen, *Mater. Res. Soc. Symp. Proc.* **910**, A01.05 (2006).
- [95] J. D. Cohen, in *Subcontract Report, NREL/SR-520-43909* (U.S. Department of Energy, Office of Scientific and Technical Information, 2008).
- [96] J. Yang, B. Yan and S. Guha, *Thin Solid Films* **487**, 162 (2005).